Flow Through Porous Media: From Mixing of Fluids to Triggering of Earthquakes

by

Birendra Jha

B.Tech. Petroleum Engineering, Indian School of Mines (2001)
M.S. Petroleum Engineering, Stanford University (2005)

Submitted to the Department of Civil and Environmental Engineering
in partial fulfillment of the requirements for the degree of

Doctor of Philosophy in the Field of Civil and Environmental Engineering

at the

MASSACHUSETTS INSTITUTE OF TECHNOLOGY

February 2014

Author .....
Department of Civil and Environmental Engineering
December 31, 2013

Certified by .....
Ruben Juanes
Associate Professor of Civil and Environmental Engineering
Thesis Supervisor

Accepted by .....
Heidi M. Nepf
Chair, Departmental Committee for Graduate Students

Flow Through Porous Media: From Mixing of Fluids to Triggering of Earthquakes

by

Birendra Jha

Submitted to the Department of Civil and Environmental Engineering
on December 31, 2013, in partial fulfillment of the
requirements for the degree of
Doctor of Philosophy in the Field of Civil and Environmental Engineering

Abstract

Enhanced oil recovery by displacing oil with solvents such as carbon dioxide requires development of miscibility between the two fluids to maximize the displacement efficiency. Prevention of inadvertent triggering of earthquakes due to injection or production of fluids in the underground requires understanding of coupling between flow and deformation processes. In this Dissertation, we study flow through porous media in two different contexts: effect of viscosity on mixing of fluids, and triggering of earthquakes due to coupling between flow and deformation.

We show that miscible viscous fingering—the hydrodynamic instability that arises when a less viscous fluid displaces the more viscous one—can be employed as an agent for enhanced mixing in porous media flows. Based on results from high-resolution numerical simulations, we derive a macroscopic model of mixing that captures the delicate interplay between channeling of less viscous fluid and creation of interfacial area as a result of viscous fingering.

The coupling between subsurface flow and geomechanical deformation is critical in the assessment of the environmental impacts of groundwater use, underground liquid waste disposal, geologic carbon dioxide storage, and exploitation of shale gas reserves. We present a new computational approach to model coupled multiphase flow and geomechanics of faulted reservoirs. We represent faults as surfaces embedded in a three-dimensional medium by using zero-thickness interface elements to accurately model fault slip under dynamically evolving fluid pressure and fault strength. We incorporate the effect of fluid pressures from multiphase flow in the mechanical stability of faults, and employ a rigorous formulation of nonlinear multiphase geomechanics that is capable of handling strong capillary effects. We develop a numerical simulation tool by coupling a multiphase flow simulator with a mechanics simulator, using the unconditionally stable fixed-stress operator split for the sequential solution of two-way coupling between flow and geomechanics. We validate our modeling approach using test cases that illustrate the onset and evolution of earthquakes from fluid injection and production.

Thesis Supervisor: Ruben Juanes
Title: Associate Professor of Civil and Environmental Engineering

Acknowledgments

I am deeply grateful to my family, friends, and mentors who have all contributed, in one way or another, to this work. I offer my sincere thanks to my advisor, Ruben Juanes, for his guidance and support. I thank my thesis committee, Bradford Hager, Dennis McLaughlin, and Charles Harvey, for their time and suggestions. I am very thankful to Luis Cueto-Felgueroso for our insightful discussions both inside and outside the Parsons Lab. I thank the members of the Juanes Research Group for their invaluable friendship. I am thankful to my wife, Ashwini Rao, for her unconditional love, and for walking with me on this journey. I thank my mother and brother for letting me pursue my dreams, and for believing in me.

Contents

List of Figures

List of Tables

Chapter 1

Introduction

Flow through porous media is ubiquitous in natural and man-made systems. Groundwater flow, recovery of oil and gas from underground reservoirs, geologic sequestration of greenhouse gases, drug delivery through microfluidics, flow through porous fuel cells, and food processing are a few examples that highlight importance of understanding the influence of the porous structure of the medium on fluid flow. The porous matrix plays a critical role in determining the flow behavior, such as pressure drop across the medium, dispersion of particles carried by the fluid, and rate of mixing and reaction between multiple fluids flowing through the medium. Conversely, the flow of fluids through a porous medium alters the mechanical behavior of the medium in response to externally applied loads, because the mechanical load is transmitted through both the pore fluid and the solid skeleton. The interplay between porous-media flow and deformation can have severe consequences, including large-scale ground subsidence and failure of geologic faults leading to earthquakes. In this Thesis, we explore two phenomena in the general field of fluid flow through porous materials: mixing of fluids of different viscosities and triggering of earthquakes.

Fluid mixing from viscous fingering. Mixing of fluids is an important and complex phenomenon. Several chemical [171], pharmaceutical [73, 16] and food processing [59] operations require controlled mixing of fluids at low Reynolds numbers, a notoriously difficult problem [198, 244, 241]. Mixing also plays a fundamental role

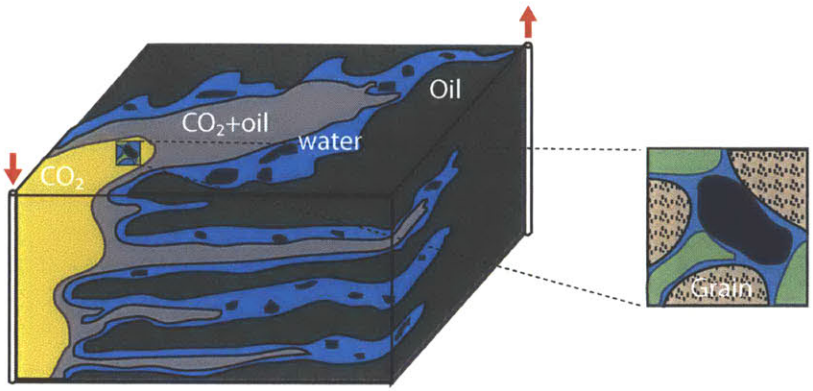

Figure 1-1: Schematic of miscible CO_2 flooding after, or with, waterflooding in an oilfield. CO_2 mobilizes the residual oil bypassed during the waterflood and increases the ultimate recovery. Displacement efficiency is a function of pore scale sweep efficiency and field scale sweep efficiency. Field scale efficiency depends on reservoir heterogeneity and viscous fingering. Alternating injection of CO_2 and water usually leads to better displacement efficiency because of comparable viscosities of oil and water, which inhibits viscous fingering at the displacement front. Solubility of CO_2 in oil and water at high pressures helps in pore scale efficiency.

in natural processes, including groundwater flows in heterogeneous media [69], mantle convection [195, 263], debris gravity currents [237], population genetics [120, 152], mammalian digestion [23], and bacterial locomotion [123, 225, 238, 239, 161, 154, 131].

When the physical properties of the fluids, such as density or viscosity, are sufficiently different, mixing may become heavily influenced by the formation of hydrodynamic instabilities. It has been shown, under controlled conditions, that such instabilities can speed up the mixing process enormously [240, 31]. Viscous fingering [125] is one such instability that ensues when a less viscous fluid displaces a more viscous one. When the two fluids are miscible with each other, the instability is called miscible viscous fingering. Miscible viscous fingering is important in enhanced oil recovery by CO_2 injection [242, 243, 81], where it can lead to a decrease in recovery efficiency [153, 113] (Fig. 1-1). It is also important in other applications such as chromatographic separation, where it leads to an undesirable peak-broadening effect [87]. In the first part of this Thesis, we study the effect of viscosity contrast on fluid mixing, and we develop a method to utilize viscous fingering for enhanced mixing in porous media flows.

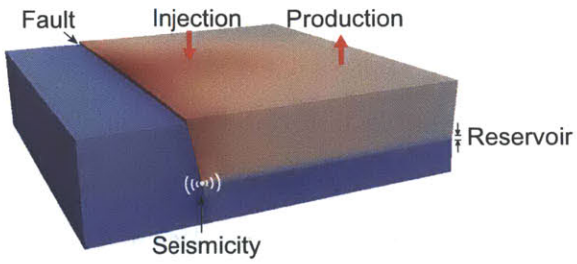

Figure 1-2: Triggering of earthquake due to underground injection and production. A fault can get destabilized by drop in fault friction, increase in pore pressure, or increase in shear traction due to differential depletion of pressure across the fault.

Fault slip and earthquake triggering. Triggering of earthquakes from anthropogenic sources is a topic of public concern [231]. Earthquakes can be triggered by reservoir impoundment behind large dams [169, 115], mine cavity collapse [205, 204], controlled explosions [72], wastewater disposal [74, 261, 145], fluid injection and production in oilfields [96], salt mining [94], geothermal energy extraction [176, 35], underground gas storage [260], and hydraulic fracturing [191, 222]. Recently, it has been reported that the number of earthquakes with magnitude $M \geq 3$ has increased sharply since year 2001, a trend that can be attributed to human activities, such as underground injection and production of fluids related to energy-development activities (e.g. carbon sequestration and shale gas recovery) [74] (Fig. 1-2). Better understanding of the physics of earthquakes may benefit society by guiding subsurface activities to prevent inadvertent triggering of earthquakes that can cause damage at the surface. In the second part of this Thesis, we focus on the role of coupling between flow and deformation that can trigger earthquakes by destabilizing critically-stressed faults in underground reservoirs.

The Thesis is organized as follows: Chapter 2 describes our approach for high-resolution numerical simulation of viscous fingering and the mechanisms that control mixing. We present a numerical scheme that is stable for arbitrarily high viscosity contrasts, for which the traditional schemes become unstable. Chapter 3 describes the macroscopic model of fluid mixing due to viscous fingering. Chapter 4 describes

mixing due to viscous fingering in an alternating injection flow, which is relevant for miscible CO_2 floods as well as microfluidic applications and lab-on-a-chip systems. Chapter 5 describes our approach for simulation of coupled multiphase flow and poromechanics of faulting in underground reservoirs. It also presents implementation details of our coupled simulator. In Chapter 6, we describe an application of the coupled simulator for estimating rock properties in a real underground gas storage field. In Chapter 7, we use the simulator to investigate the role of pore pressure in triggering a real earthquake. The results in Chapters 2, 3 and 4 have been published previously [136, 135, 137], while Chapters 5, 6 and 7 will each be the subject of a separate future publication.

Chapter 2

Numerical simulation of fluid mixing from viscous fingering

2.1 Introduction

Miscible viscous fingering has been studied extensively in the past through laboratory experiments [151, 14, 206] and numerical simulations [50, 249, 49, 279, 280]. Linear stability analyses have explained the onset and growth of instabilities as a function of the viscosity contrast and the flow rate for rectilinear [248] and radial [214] geometries. A number of experimental, theoretical and numerical studies have been carried out to understand the effects of anisotropic dispersion [275, 279, 281], medium heterogeneity [250, 252, 65, 66], gravity [251, 178, 157, 219, 89, 213], chemical reaction [88, 67, 63, 189], adsorption [183], and flow configuration [203, 276, 45, 46, 211, 44] on the viscous fingering instability.

It has long been recognized that viscous fingering leads to enhanced *spreading* of the displacing fluid [28, 117]. A large body of literature, going back to the works of Koval [153] and Todd and Longstaff [257], has focused on the development of fractional flow formulations to predict averaged concentrations and breakthrough curves [82, 83, 84, 29, 30, 272, 158, 273, 139, 140, 184].

Despite the considerable work done, the effect of viscous fingering on fluid *mixing* remains unexplored. It is not known how the degree of mixing evolves under vis-

Figure 2-1: Snapshot of the concentration field during the unstable displacement of a more viscous fluid (dark) by a fully-miscible, less viscous fluid (light). The formation, splitting, and nonlinear interaction of viscous fingers induce disorder in the velocity field that affects the mixing rate between the fluids. The displacement corresponds to a viscosity ratio $M = \exp(3.5) \approx 33$ and Péclet number $\mathrm{Pe} = 10^4$. See also Video 1 in [1].

cous fingering and whether optimum mixing can be achieved by varying the viscosity contrast and the flow rate. In this chapter, we focus on answering these two questions.

2.2 Governing equations

We consider Darcy flow of two fluids of different viscosities μ_1 and μ_2, where $\mu_1 < \mu_2$, in a porous medium. We assume that the porosity ϕ (volume of voids per unit volume of porous medium) and the permeability k (coefficient relating flow velocity and pressure gradient) are uniform and constant. This means that the porous medium is homogeneous and isotropic. The two fluids are assumed to be first-contact miscible, neutrally buoyant and incompressible. This means that the injected and the resident fluids mix instantaneously in all proportions to form a single phase and, therefore, surface tension effects are, by definition, absent. The diffusivity D between the fluids is assumed to be constant, isotropic and independent of concentration. The length and width of the domain are L and W, and the mean velocity is in the x-direction

and of magnitude U. The governing equations in dimensional form are

$$\phi\frac{\partial c}{\partial t} + \nabla \cdot (\boldsymbol{u}c - D\nabla c) = 0, \tag{2.1}$$

$$\boldsymbol{u} = -\frac{k}{\mu(c)}\nabla p, \qquad \nabla \cdot \boldsymbol{u} = 0, \tag{2.2}$$

in $x \in [0, L]$ and $y \in [0, W]$. Eq. (2.1) is a linear advection-diffusion transport equation (ADE) for the concentration of the less viscous fluid $c(\boldsymbol{x}, t)$, that is, the mass of the less viscous fluid per unit volume of the mixture. Eq. (2.2) is Darcy's law defining the velocity of the mixture, which satisfies the incompressibility constraint. The viscosity of the mixture, $\mu(c)$, is assumed to be an exponential function of concentration, $\mu(c) = \mu_1 e^{R(1-c)}$, where $R = \log M$ and $M = \mu_2/\mu_1$ is the viscosity ratio.

We express the equations in nondimensional form using characteristic quantities, W, U and $\mu_2 = \mu_1 e^R$, for length, velocity and viscosity, respectively. The characteristic time and pressure drop are given by $T = \phi W/U$ and $P = \mu_2 UW/k$, respectively. Abusing notation, we write the governing equations in dimensionless form:

$$\frac{\partial c}{\partial t} + \nabla \cdot \left(\boldsymbol{u}c - \frac{1}{\mathrm{Pe}}\nabla c\right) = 0, \tag{2.3}$$

$$\boldsymbol{u} = -\frac{1}{\mu(c)}\nabla p, \qquad \nabla \cdot \boldsymbol{u} = 0, \tag{2.4}$$

in $x \in [0, L/W]$, $y \in [0, 1]$, where $c \in [0, 1]$ is now the volume fraction of the least viscous fluid, and $\mu(c) = e^{-Rc}$ is the dimensionless viscosity. Darcy's law and the divergence-free condition in Eq. (2.4) can be combined to obtain the pressure equation in explicit form,

$$\nabla \cdot \left(-\frac{1}{\mu(c)}\nabla p\right) = 0. \tag{2.5}$$

The system is governed by two nondimensional groups: the Péclet number $\mathrm{Pe} = UW/D$ and the viscosity ratio $M = \mu_2/\mu_1$. A displacement of the high viscosity fluid by the low viscosity fluid for high mobility ratio and high Péclet number leads to aggressive viscous fingering (Fig. 2-1).

2.2.1 Fluid mixing in a periodic field

Since viscous fingering instabilities are caused by viscosity contrasts, and therefore by concentration gradients, the decay of σ^2 as mixing progresses is closely linked to the decay of the flow disorder due to fingering. Indeed, a natural way to characterize the interplay of mixing and viscous instabilities is to understand the decay of a fully developed fingered flow away from the boundaries. We simulate this flow scenario by considering the mixing of two fluids driven by a constant flow rate in a periodic domain. After a short initial transient, the onset of fingering leads to a highly heterogeneous flow and intense mixing. At later times, the system evolves towards a more homogeneous, synchronous decay of concentration gradients and velocity fluctuations.

We use the global variance of the concentration field, $\sigma^2 \equiv \langle c^2 \rangle - \langle c \rangle^2$, to define the degree of mixing,

$$\chi(t) = 1 - \sigma^2(t)/\sigma^2_{\max}, \tag{2.6}$$

where $\langle \cdot \rangle$ denotes spatial averaging over the domain volume V. The maximum variance, $\sigma^2_{\max}$, corresponds to a perfectly segregated state, hence $\sigma^2_{\max} = 0.25$ for a mean concentration $\langle c \rangle = 0.5$. In a perfectly mixed state, $\sigma^2 = 0$ and $\chi = 1$.

We first derive the evolution equation for the global concentration variance σ^2. Multiplying the ADE [Eq. (2.3)] by c results in

$$c\frac{\partial c}{\partial t} + c\nabla \cdot (\boldsymbol{u}c) = \frac{1}{\mathrm{Pe}} c\nabla^2 c, \tag{2.7}$$

where ∇^2 denotes the Laplacian operator. Expanding the right hand side and averaging over the domain,

$$\frac{1}{2}\left\langle \frac{\partial c^2}{\partial t} + \nabla \cdot \left(\boldsymbol{u}c^2\right) \right\rangle = \frac{1}{\mathrm{Pe}} \langle \nabla \cdot (c\nabla c) - |\nabla c|^2 \rangle. \tag{2.8}$$

Applying the Gauss divergence theorem gives

$$\begin{aligned}\langle \nabla \cdot (\boldsymbol{u}c^2) \rangle &= \frac{1}{V} \int_S c^2 \boldsymbol{u} \cdot \boldsymbol{n} dS, \\ \langle \nabla \cdot (c \nabla c) \rangle &= \frac{1}{V} \int_S c \nabla c \cdot \boldsymbol{n} dS,\end{aligned} \tag{2.9}$$

where S is the surface bounding V, dS the element of boundary area, and $\boldsymbol{n}$ the outward-pointing normal to the boundary. Assuming periodicity in x and y, these two boundary surface integrals vanish and Eq. (2.8) becomes

$$\frac{d\langle c^2 \rangle}{dt} = -\frac{2}{\mathrm{Pe}} \langle |\nabla c|^2 \rangle. \tag{2.10}$$

Since the mean concentration $\langle c \rangle$ remains constant in a periodic domain, the evolution of concentration variance under periodic boundary conditions becomes [209, 159],

$$\frac{d\sigma^2}{dt} = -2\epsilon, \tag{2.11}$$

where

$$\epsilon \equiv \langle |\boldsymbol{g}|^2 \rangle / \mathrm{Pe} \tag{2.12}$$

is the dimensionless mean scalar dissipation rate and $\boldsymbol{g} \equiv \nabla c$. In absence of any source terms, Eq. (2.11) indicates that the global concentration variance monotonically decays with time due to the dissipative action of ϵ which is positive as long as there are gradients in the concentration field. Eq. (2.6) and Eq. (2.11) together identify degree of mixing as cumulative dissipation. Physically, ϵ can be interpreted as a mixing rate or, equivalently, as a rate at which scalar fluctuations are destroyed.

In the initial stages of a rectilinear displacement, under a quasi-steady-state approximation (QSSA) of the base state, linear stability analysis predicts the wavenumber and growth factor of the most unstable mode [248]. In the nonlinear regime, the length scale of viscous fingers arises from diffusion and nonlinear interactions, including channeling, tip-splitting, merging, fading, and shielding [125, 279]. The dissipation scale, also referred to as Taylor microscale for the scalar fluctuations [77],

is defined as

$$s \equiv \sqrt{\sigma^2/\epsilon \mathrm{Pe}}. \tag{2.13}$$

Just like the finger width w, the scalar dissipation length s is a transverse length scale in the problem. It is related to the diffusion of scalar gradients across the flow, and can be interpreted as the thickness of the interface on which the scalar gradients are localized. The Taylor microscale for mechanical energy is defined as $\lambda_{\mathrm{Taylor}} = (\nu u^2/\epsilon_u)^{1/2}$, where ν is the kinematic viscosity, and

$$\epsilon_u = 2\langle \nu \nabla^{\mathrm{sym}} \boldsymbol{u} : \nabla^{\mathrm{sym}} \boldsymbol{u} \rangle, \tag{2.14}$$

is the mean mechanical energy dissipation rate [209]. Superscript sym denotes the symmetric part of the tensor.

Eq. (2.11) motivates us to study the evolution of ϵ in time and understand its dependence on the governing physical parameters, R and Pe. We obtain an evolution equation for ϵ by taking the gradient of the ADE, performing a dot product with $\boldsymbol{g}$ and averaging over the domain (similar to the derivation of k-epsilon models in turbulence [209]). Taking the gradient of the ADE in Eq. (2.3) and then dot product with ∇c yields

$$\nabla c \cdot \frac{\partial \nabla c}{\partial t} + \nabla c \cdot \nabla \left(\boldsymbol{u} \cdot \nabla c \right) = \frac{1}{\mathrm{Pe}} \nabla c \cdot \nabla \left(\nabla^2 c \right), \tag{2.15}$$

Using $\boldsymbol{g} = \nabla c$ and $\nabla \cdot \boldsymbol{u} = 0$,

$$\begin{aligned} \frac{1}{2} \frac{\partial \left| \nabla c \right|^2}{\partial t} + \sum_{i,j} \frac{\partial u_i}{\partial x_j} g_i g_j + \frac{1}{2} \sum_i \nabla \cdot \left(\boldsymbol{u} g_i^2 \right) \\ = \frac{1}{\mathrm{Pe}} \nabla c \cdot \nabla \left(\nabla^2 c \right) \end{aligned} \tag{2.16}$$

where u_i, x_j and g_i are components of the velocity, position and concentration gradient vectors, respectively. Integrating over a periodic domain removes the divergence terms

on the left hand side. Expanding the right hand side,

$$\begin{aligned}\nabla c \cdot \nabla \left(\nabla^2 c\right) &= \sum_{i,j} g_i \frac{\partial^2 g_j}{\partial x_i \partial x_j} = \sum_{i,j} g_i \frac{\partial^2 g_i}{\partial x_j^2} \\ &= \sum_i \nabla \cdot \left(g_i \nabla g_i\right) - \sum_{i,j} \left(\frac{\partial g_i}{\partial x_j}\right)^2 .\end{aligned} \tag{2.17}$$

Upon volume integration, the divergence terms in Eqs. (2.16)–(2.17) vanish under periodic boundary conditions. The assumption of periodicity is usually valid in fully-developed fingering flow away from the boundaries. Using the definition of ϵ, Eq. (2.16) becomes

$$\frac{d\epsilon}{dt} + \frac{2}{\mathrm{Pe}} \sum_{i,j} \left\langle \frac{\partial u_i}{\partial x_j} g_i g_j \right\rangle = -\frac{2}{\mathrm{Pe}^2} \sum_i \langle |\nabla g_i|^2 \rangle \tag{2.18}$$

Alternatively, in direct tensorial notation,

$$\frac{d\epsilon}{dt} + \frac{2}{\mathrm{Pe}} \langle \nabla \boldsymbol{u} : \boldsymbol{g} \otimes \boldsymbol{g} \rangle = -\frac{2}{\mathrm{Pe}^2} \langle \nabla \boldsymbol{g} : \nabla \boldsymbol{g} \rangle, \tag{2.19}$$

where $\otimes$ denotes a dyadic product of two vectors resulting in a second-order tensor, : denotes double contraction, and $\nabla \boldsymbol{u}$ is the gradient of the velocity field. The second term in Eq. (2.19) is the rate of stretching of the square norm of concentration gradient $\boldsymbol{g}$ and it is negative due to fingering. For a globally chaotic flow with steady or time-periodic velocity fields, it is proportional to $\langle |\boldsymbol{g}|^2 \rangle$. For viscous fingering displacements, where the velocity field is a function of concentration, the dependency on $\boldsymbol{g}$ is stronger and there is an additional dependency on the viscosity contrast.

Eqs. (2.11) and (2.19) are *exact* evolution equations for the global concentration variance σ^2 and the mean scalar dissipation rate ϵ, respectively. Clearly, closure relations are needed for this system of equations to be solvable, and the objective of this work is precisely to propose a closure model, guided by direct numerical simulation of the underlying partial differential equations. The form of Eq. (2.19), however, already reveals that the heart of the problem lies in the interplay between velocity gradients (flow disorder) and concentration gradients. Since gradients in concentration lead to

contrasts in fluid viscosity, homogenization of the mixture through removal of the concentration gradients also results in destruction of the viscosity contrasts, that is, decay of viscous fingering. Eq. (2.11) reflects that the degree of mixing increases monotonically in time. One could naively expect, in view of the right hand side of Eq. (2.19), that the same be true for the scalar dissipation rate. However, this is not the case: as we shall see, concentration gradients increase during the early stages of viscous fingering before starting to decrease, resulting in a nontrivial behavior for the scalar dissipation rate and the overall mixing process.

2.3 Numerical method

2.3.1 Streamfunction–vorticity method

The pressure equation, Eq. (2.5), is an elliptic PDE with a space- and time-varying coefficient. Solving this equation is computationally expensive for large number of grid cells, which is required to resolve the concentration gradients that ensue as a result of the viscous instability at high Pe. To alleviate this computational burden, the governing equations are usually cast in the so-called streamfunction–vorticity formulation, and the "pressure" equation solved using a spectral method [249, 279, 45].

The streamfunction Ψ is defined for an incompressible two-dimensional velocity field as

$$u_x = \frac{\partial \Psi}{\partial y}, \qquad u_y = -\frac{\partial \Psi}{\partial x}. \tag{2.20}$$

The magnitude of the vorticity vector normal to the plane of flow, $\omega \equiv |\nabla \times \boldsymbol{u}|$, is related to the gradients in concentration field. Using the definition of the Darcy velocity [Eq. (2.4)] and the exponential form of the mixture viscosity,

$$\omega = R\,|\nabla c \times \boldsymbol{u}| = R\left(\frac{\partial c}{\partial x}u_y - \frac{\partial c}{\partial y}u_x\right). \tag{2.21}$$

Using the definitions of the streamfunction and vorticity, we obtain the relation

$$\nabla^2\Psi = -\omega. \tag{2.22}$$

In the streamfunction-vorticity (SV) method, Eqs. (2.3) and (2.22) are solved sequentially under periodic boundary conditions. At a given time step, Eq. (2.21) is used to compute the vorticity field from known concentration and velocity fields. Then Eq. (2.22), which is a single algebraic equation in Fourier space under periodic boundary conditions, is solved to obtain the streamfunction of the flow at the next time step using the vorticity at previous time step. The velocity field is then constructed from the streamfunction using Eq. (2.20).

This computational approach has been used successfully for the nonlinear simulation of the viscous fingering phenomenon [249, 279, 45], with a degree of fidelity and resolution that was not possible in early simulations [50, 49]. However, this formulation is numerically unstable and fails to produce a solution for large values of mobility ratio ($M > 20$ or $R > 3$), when the finger tip velocity is much higher than the mean flow velocity. The underlying reason for the numerical instability is the splitting of the fluid mobility in Eq. (2.22), which computes the streamfunction at the current time step from the vorticity at the previous time step. This split is stable for moderate values of M, but becomes unconditionally unstable for large values of M, irrespective of time step size.

2.3.2 Implicit mobility method

Obtaining a numerical scheme that is stable at high M requires an implicit mobility scheme. To this end, we solve Eq. (2.5) globally for the pressure field. This is computationally more expensive because it entails building and solving a linear system of equations at each time step, instead of one single equation in Fourier space [Eq. (2.22)]. However, since the solution of Eq. (2.5) implies implicitness—the velocity at a time step corresponds to the mobility at the same time step—this scheme is stable for arbitrarily high values of M. We use a finite volume method with two-point

flux approximation (TPFA) to discretize the Darcy flux between the grid cells [162]. We solve the linear system of equations resulting from discretizating Eq. (2.5) using either a direct solver or an iterative multigrid solver. The concentration equation is solved using a sixth-order compact finite differences and a third-order Runge-Kutta time-stepping scheme [219].

We use a finite volume discretization of the divergence-free velocity condition in Eq. (2.3). Integrating over the volume of the ith cell V^i and using the divergence theorem,

$$\int_{V^i} \nabla \cdot \boldsymbol{u} = \int_{S^i} \boldsymbol{u} \cdot \boldsymbol{n} dS = 0, \tag{2.23}$$

where S^i is the total surface area of the cell, comprised of interfaces S^{ij} where j denotes cells adjacent to the ith cell. Thus, fluid mass balance over cell i for an incompressible flow becomes

$$\sum_j U^{ij}(t) = 0, \tag{2.24}$$

where U^{ij} is the integrated flux through interface S^{ij}. The pressure field $p(x, y)$ is approximated as a piecewise constant function, taking discrete values p^i at individual cells. Fluxes across interfaces are estimated from a set of neighboring cell pressures. The TPFA method uses just two neighboring cell pressures, p^i and p^j, to approximate the flux through the interface ij,

$$U^{ij} = t^{ij}\lambda^{ij}\left(p^i - p^j\right), \tag{2.25}$$

where λ^{ij} is the mobility at the ij-interface, estimated by a harmonic average of the respective cell mobilities, $1/\mu^i$ and $1/\mu^j$, and t^{ij} is the interface geometric transmissibility, which for a regular 2D Cartesian grid is proportional to the length of the interface and inversely proportional to the distance between cell centers. Thus, the interface transmissibility $T^{ij} = t^{ij}\lambda^{ij}$, for a simple 2D Cartesian grid, is

$$T_x^{ij} = \frac{h_y}{h_x}\frac{2}{\mu^i + \mu^j}, \quad T_y^{ij} = \frac{h_x}{h_y}\frac{2}{\mu^i + \mu^j}, \tag{2.26}$$

for vertical and horizontal interfaces, respectively. Eqs. (2.24)–(2.25) result in a system of linear equations to be built and solved at every time step,

$$\boldsymbol{TP} = \boldsymbol{B}, \tag{2.27}$$

where $\boldsymbol{P}$ is the vector of unknown cell-center pressures and $\boldsymbol{B}$ is the vector of known boundary fluxes. Generation and assembly of the mobility-dependent transmissibility matrix, $\boldsymbol{T}$, for the simple periodic boundary conditions as considered here, can be completely vectorized.

2.4 Nonlinear simulations

2.4.1 Continuous injection

To illustrate the ability of the implicit high-resolution numerical method to simulate viscous fingering for high viscosity ratios, we solve the governing equations on a square domain with periodic boundary conditions in the y-direction, and uniform flux on the left and right boundaries. Initially, the medium is filled with the more viscous fluid, and the less viscous fluid is injected through the left boundary. For high viscosity ratios ($R = 4$, corresponding to $M \approx 55$), the invading fluid fingers through the defending fluid aggressively (Fig. 2-2a), exhibiting well-known complex nonlinear interactions such as finger merging, shielding, and tip splitting [249, 279]. Simulation of the flow for this viscosity contrast is outside the range of stability of the streamfunction-vorticity method. For an even larger viscosity ratio ($R = 5$, corresponding to $M \approx 150$), a new pattern emerges: *channeling* through the more viscous fluid, with minimal interaction between channels and very low sweep efficiency (Fig. 2-2b).

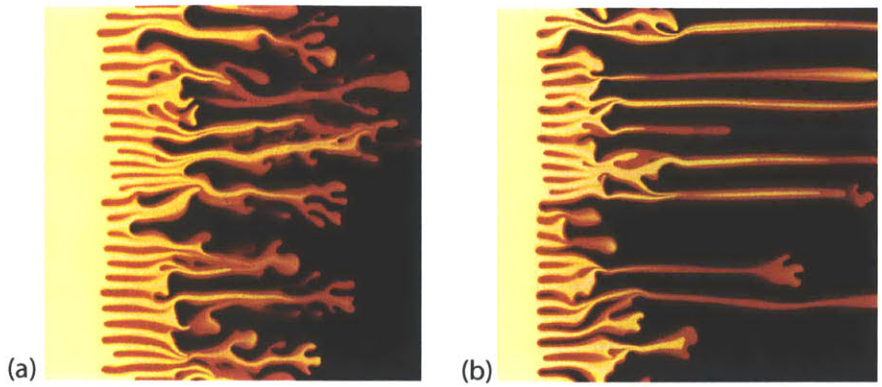

Figure 2-2: Snapshots of the concentration field from viscous fingering simulations using the implicit mobility TPFA method (**a**: $R = 4$, $\mathrm{Pe} = 5000$, **b**: $R = 5$, $\mathrm{Pe} = 5000$). Channeling of the fingers of less viscous fluid at high R renders the explicit mobility streamfunction-vorticity method unstable.

2.4.2 Mixing of randomized blobs

To understand the effect of viscous fingering on fluid mixing we numerically solve the governing equations, Eqs. (2.3)–(2.4), on a square domain with periodic boundary conditions. The periodic boundary conditions allow us to focus on the dissipative nature of viscous fingering in absence of any boundary effects.

We investigate a scenario in which the two fluids are segregated as a set of randomly-shaped blobs of the more viscous fluid surrounded by the connected, less viscous fluid (Fig. 2-3). This flow set up is analogous to that used to study scalar fields in decaying grid turbulence [268]. Each fluid occupies 50% of the volume and, since the boundary conditions are bi-periodic, $\langle c \rangle \equiv 0.5$ throughout the entire simulation. The characteristic diameter of the initial blobs is about one-sixth of the length of the domain, and the system evolves under an imposed pressure gradient from left to right. If both fluids had the same viscosity, the blobs would simply translate in the x-direction and slowly diffuse into the ambient fluid. The situation is radically different in the presence of a viscosity contrast.

Onset of fingering driven by advection creates new interfacial area through stretching and splitting of the initial interface around the blobs, thereby enhancing diffusive mixing because both the interfacial area and the concentration gradients are larger. The competition between fingering-induced stretching and diffusive forces yields a

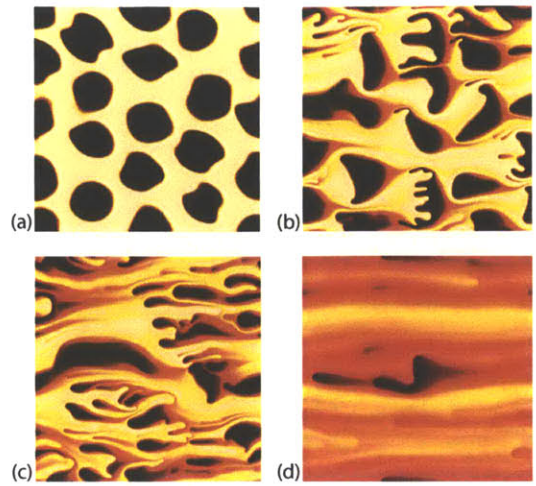

Figure 2-3: Snapshots of the concentration field at increasing time steps from a numerical simulation of miscible viscous fingering. A set of more viscous blobs (dark) is displaced through a less viscous fluid (light) under left-to-right flow and periodic boundary conditions. Fingers of the less viscous fluid initiate at the unstable interface, grow inside the more viscous blobs, split into multiple fingers, coalesce together and connect across the blobs as the two fluids mix. The displacement corresponds to a viscosity ratio $M = \exp(2) \approx 7$ and Péclet number $\mathrm{Pe} = 10^4$.

non-monotonic time evolution of the scalar dissipation rate, which achieves a maximum precisely as a result of fingering-induced mixing (Fig. 2-4). Since less viscosity implies higher mobility, fingering also causes channeling of the low viscosity fluid, which bypasses large areas of the flow domain, thereby reducing the overall mixing efficiency. At later times, the strength of the instability decays due to homogenization of the mixture and, asymptotically, mixing is again controlled by diffusion. During this regime, we find the scalings $\epsilon \sim t^{-2}$, $\sigma^2 \sim t^{-1}$, and $s \sim t^{1/2}$.

Heterogeneity and disorder induced by viscous fingering leads to flow fields with statistical properties that resemble those of decaying turbulence (Fig. 2-5). Both the mechanical energy dissipation rate and the scalar energy dissipation rate increase with time synchronously due to viscous fingering, before beginning to decline due to diffusion.

To illustrate that mixing under viscous fingering is strongly dependent on the flow conditions, we simulate the scenario in which blobs of less viscous fluid are transported and dispersed through a more viscous ambient fluid. Viscous fingers now emerge out of the blobs and into the connected fluid. The initial interfacial area available for

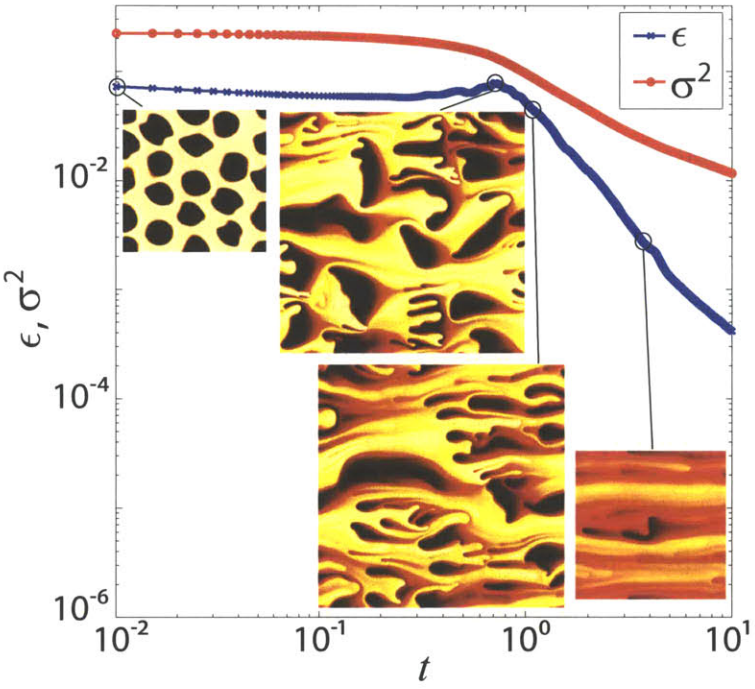

Figure 2-4: Decay of miscible viscous fingering. A binary mixture of initially segregated fluids is driven at constant flow rate in a periodic domain. The variance of concentration, σ^2 (red), a proxy for the degree of mixing, decreases monotonically with time. The mean scalar dissipation rate, ϵ (blue), increases at early times due to the onset of fingering, and decays monotonically at later times. The simulation parameters are $R = 2, \mathrm{Pe} = 10^4$. See also Video 2 in [1].

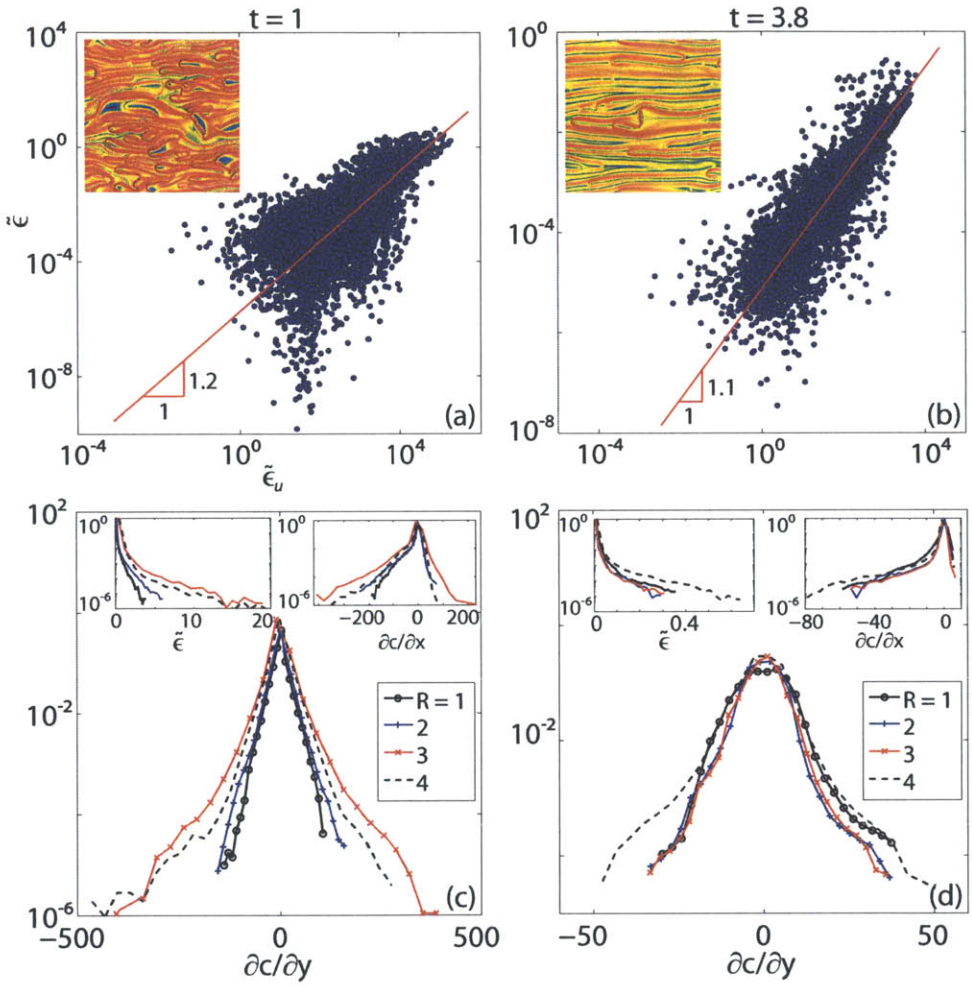

Figure 2-5: The dissipative structure of viscous fingering. (a),(b) The mechanical and scalar dissipation rates synchronize as mixing advances, as shown by the scatter plots of mechanical (ϵ_u) against scalar (ϵ) dissipation rates at early (a) and late (b) times. At late times we find $\epsilon_u \sim \epsilon^\alpha$, with $\alpha \approx 1$. Inset, logarithm of the scalar dissipation rate. (c),(d) Probability density function (PDF) of the derivatives of the concentration field and scalar dissipation rate. (c) At early times, $\partial c/\partial y$ exhibits characteristic exponential tails. This behavior is similar to that of passive scalars in turbulent flows [268]. (e) At late times, the PDFs tend toward a Gaussian behavior. The skewness of $\partial c/\partial x$ reflects the inhomogeneity of the flow, which is driven at a constant rate from left to right.

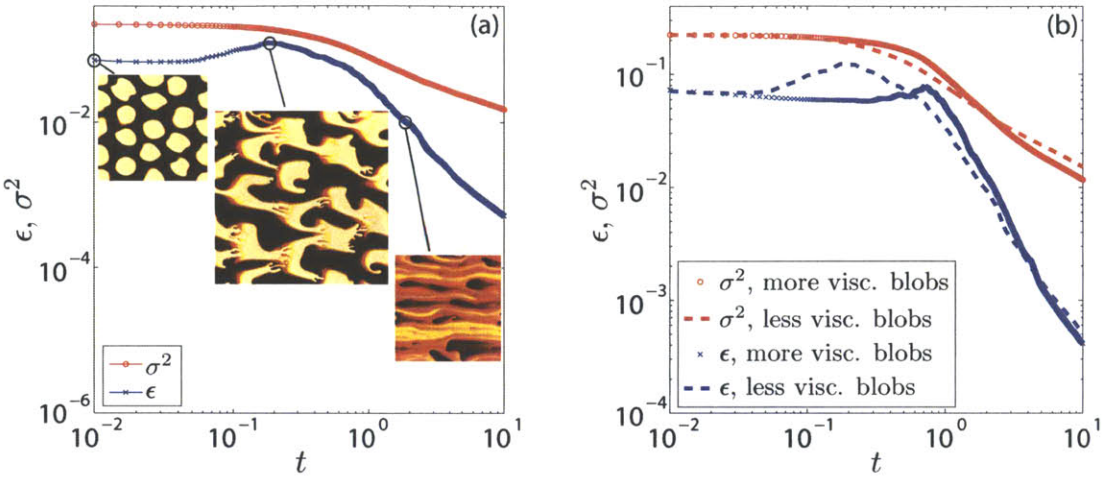

Figure 2-6: **a**, Evolution of mean scalar dissipation rate (blue) and concentration variance (green) for blobs of less viscous fluid in a more viscous medium. **b**, Comparison of the two scenarios, when the initial blobs are either more viscous or less viscous than the ambient fluid. The case with less viscous blobs leads to earlier and larger hump in the evolution of the scalar dissipation rate ϵ. This results in faster decay of the concentration variance at early times. The simulations correspond to $R = 2$, $\mathrm{Pe} = 10^4$.

the initiation and growth of the fingers is larger in this case than in the previous configuration (blobs of more viscous fluid). Moreover, the less viscous fluid must initially penetrate through the more viscous fluid before it forms a connected 'phase'. As a result of the earlier finger initiation and more aggressive tip splitting, the scalar dissipation rate ϵ exhibits a larger and earlier hump in the scalar dissipation rate (Fig. 2-6), which translates into faster mixing.

2.5 Conclusion

We analyze the mixing process in viscously unstable laminar flows, by means of high-resolution numerical simulations. We present a numerical scheme for the high-resolution simulation of the viscous fingering process that is stable for arbitrarily high viscosity contrasts, for which the traditional schemes become unstable. Using the results from simulations, we characterize the evolution of the degree of mixing between two fluids of different viscosities. We show that viscous fingering leads to two competing effects. On one hand, it enhances mixing by inducing disorder in the

velocity field, and increasing the interfacial area between the fluids. On the other, it causes channeling of the low viscosity fluid, which bypasses large areas of the flow domain—these regions remain unswept thereby reducing the overall mixing efficiency. This competition between creation of fluid–fluid interfacial area and channeling results in nontrivial mixing behavior.

Our results show that interfacial area and dissipation rate are the central variables to understand mixing enhanced by viscous fingering. From a design perspective, the viscosity contrast that provides optimum mixing time depends on the Péclet number, and arises from a delicate balance between interface stretching due to flow disorder, and channeling due to the higher mobility of the less viscous fluid. The use of ideas from turbulence modeling, synthesized in our two-equation model, provides a framework to upscale the dissipative effects of fingering in large-scale flow models.

Chapter 3

Macroscopic model of mixing from viscous fingering

3.1 Introduction

We are interested in developing an upscaled model to quantify the degree of mixing, χ, in a viscously unstable displacement by capturing the nontrivial interplay between channeling and creation of interfacial area as a result of viscous fingering. The objective is to obtain a mixing model in terms of evolution equations for the global variables, the concentration variance σ^2 and the mean scalar dissipation rate ϵ, that incorporates their dependency on the governing physical parameters, the log-viscosity ratio R and Péclet number Pe. We derive the model for a bi-periodic domain (periodic flow in both longitudinal and transverse directions) under the assumptions of high Péclet number and statistical homogeneity, which are used to provide closure for the terms in the evolution equation of ϵ, Eq. (2.19). We verify our assumptions by observations in the high-resolution numerical simulations of the viscous fingering process. We then use the $\sigma^2 - \epsilon$ model to predict the range of viscosity contrast that maximizes mixing in a periodic domain.

3.2 Mixing model

To arrive at such a macroscopic description, we must model the "advective" and "diffusive" terms in the exact equation for evolution of the mean scalar dissipation rate, Eq. (2.19). The advective term involves the interaction between velocity gradients and concentration gradients. This interaction is responsible for stretching of the interface between the less and the more viscous fluids, as well as tip-splitting and channeling events. We capture the macroscopic effect of velocity gradients through mean mechanical energy dissipation rate, ϵ_u, which is strongly correlated to the mean scalar dissipation rate in a statistically homogeneous and isotropic flow [173]. The diffusive term in Eq. (2.19) is responsible for the removal of the fluid interfaces, which arise due to the splitting and channeling events, or due to the initial configuration (e.g. initial interfaces of the blobs in Fig. 2-3(a)).

3.2.1 Mechanical dissipation rate

We introduced the mean mechanical energy dissipation rate, ϵ_u, in Eq. (2.14). ϵ_u is a macroscopic quantity defined in terms of the velocity gradients. It captures the dissipation of mechanical energy due to changes in velocity correlations and changes in intensity of the flow disorder (intensity of the viscous fingering process) in the domain. ϵ_u is calculated from $\nabla^s \boldsymbol{u}$, which is the rate-of-strain tensor responsible for interface stretching. From Darcy's equation [Eq. 2.4], we have

$$\nabla \boldsymbol{u} = -\mu^{-1} \left[R \nabla c \otimes \nabla p + \nabla \left(\nabla p \right) \right]. \tag{3.1}$$

In a viscous fingering process, $R\nabla c \otimes \nabla p$ and $\nabla \left(-\nabla p \right)$ terms evolve similarly in time (Fig. 3-1). Thus, we propose the scaling

$$\nabla \boldsymbol{u} \sim -\mu^{-1} \left[R \nabla c \otimes \nabla p \right] \sim R \boldsymbol{u} \otimes \boldsymbol{g}. \tag{3.2}$$

Therefore, assuming a spatially-averaged kinematic viscosity $\langle \nu \rangle$, ϵ_u can be approxi-

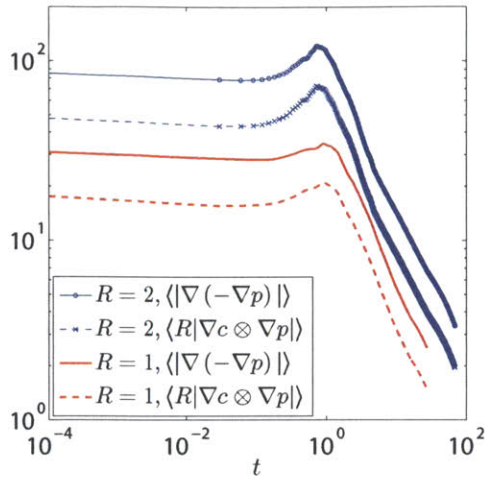

Figure 3-1: Evolution in time of the terms $\langle R\,|\nabla c \otimes \nabla p|\rangle$ and $\langle|\nabla\,(-\nabla p)|\rangle$ from direct numerical simulations for Pe $= 10^4$ and two different values of R ($R = 1, 2$). The time evolution of both terms is very similar.

mated as,

$$\begin{aligned} \epsilon_u &\sim 2\langle\nu\rangle R^2 \left\langle \mu^{-2} \left|(\nabla c \otimes \nabla p)^{\mathrm{s}}\right|^2 \right\rangle \\ &\sim 2\langle\nu\rangle R^2 \left\langle \left|(\boldsymbol{u} \otimes \boldsymbol{g})^{\mathrm{s}}\right|^2 \right\rangle . \end{aligned} \tag{3.3}$$

Using the Frobenius norm of a tensor,

$$\left|(\boldsymbol{u} \otimes \boldsymbol{g})^{\mathrm{s}}\right|^2 = \frac{1}{2}\left[|\boldsymbol{u}|^2\,|\boldsymbol{g}|^2 + (\boldsymbol{u}\cdot\boldsymbol{g})^2\right] . \tag{3.4}$$

Hence,

$$\epsilon_u \sim \langle\nu\rangle R^2 \left\langle |\boldsymbol{u}|^2\,|\boldsymbol{g}|^2 \left(1 + \cos^2\theta\right)\right\rangle , \tag{3.5}$$

where θ is the angle between vectors $\boldsymbol{u}$ and $\boldsymbol{g}$ at the interface. Assuming homogeneity of the viscous fingering process, we can split the average of the product as product of the averages (as in the case of statistically homogeneous turbulence [254]). Neglecting the $\cos^2\theta$ term, which is small compared to the other term,

$$\epsilon_u \sim \langle\nu\rangle R^2 \langle|\boldsymbol{g}|^2\rangle \langle|\boldsymbol{u}|^2\rangle \tag{3.6}$$

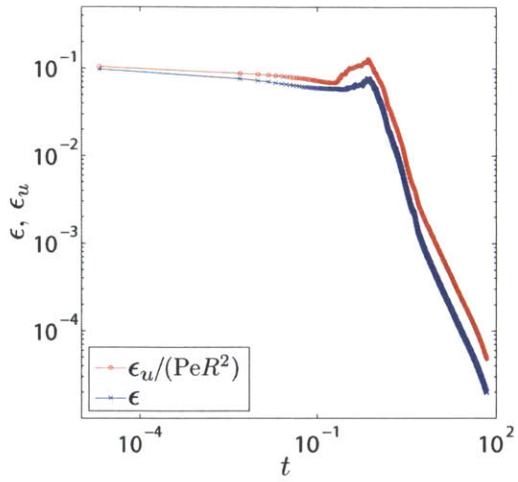

Figure 3-2: Evolution of ϵ and $\epsilon_u/(\mathrm{Pe}R^2)$ from direct numerical simulation, for $R = 2$ and $\mathrm{Pe} = 10^4$. The two variables evolve similarly, confirming the proposed scaling in Eq. (3.7).

Taking the mean flow speed U as constant and using $\epsilon \equiv \langle |\boldsymbol{g}|^2 \rangle / \mathrm{Pe}$, we obtain,

$$\epsilon_u \sim R^2 \mathrm{Pe} \epsilon. \tag{3.7}$$

Thus, the mean mechanical dissipation rate and the mean scalar dissipation rate evolve similarly during the viscous fingering process. We have verified this relationship by means of direct numerical simulation (Fig. 3-2). This is an important result which allows us to model the interface stretching due to velocity disorder in terms of scalar gradients.

3.2.2 Scalar dissipation rate

Mean scalar dissipation rate, ϵ, controls the rate of mixing as is evident from Eq. (2.11). Evolution of ϵ is governed by a balance between higher-order advective and diffusive flux terms in Eq. (2.19). From Eq. (3.2), we approximate the advective term in Eq. (2.19) as,

$$\frac{2}{\mathrm{Pe}} \langle \nabla \boldsymbol{u} : \boldsymbol{g} \otimes \boldsymbol{g} \rangle \sim \frac{2}{\mathrm{Pe}} \langle R \, |\boldsymbol{g}|^2 \, (\boldsymbol{u} \cdot \boldsymbol{g}) \rangle \tag{3.8}$$

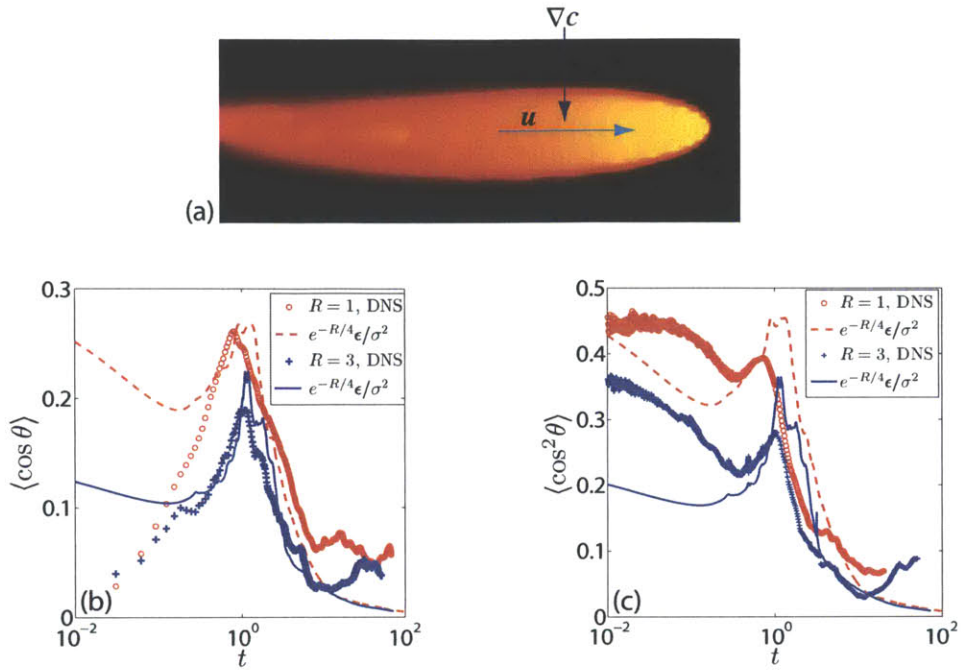

Figure 3-3: Effect of channeling on the evolution of $\langle \cos\theta \rangle$ and $\langle \cos^2\theta \rangle$. **a,** channeling of the less viscous fluid at high R means that vectors $\boldsymbol{u}$ and ∇c are approximately orthogonal ($\theta \approx \pi/2$) along the body of the channel except near the tip. This reduces $\langle \cos\theta \rangle$ because channels dominate the flow (suppress tip-splitting) in the entire domain. **b, c,** Comparison of the time evolution of $\langle \cos\theta \rangle$ and $\langle \cos^2\theta \rangle$ from the direct numerical simulations and the proposed model $\langle \cos\theta \rangle = e^{-R/4}\epsilon/\sigma^2$, for $R = 1, 3$ and $\mathrm{Pe} = 10^4$.

Assuming, as before, statistical homogeneity at high Pe,

$$\begin{aligned} \frac{2}{\mathrm{Pe}} \langle R\,|\boldsymbol{g}|^2\,(\boldsymbol{u}\cdot\boldsymbol{g}) \rangle &\sim -\frac{2R}{\mathrm{Pe}} \langle |\boldsymbol{g}|^3 \rangle \langle |\boldsymbol{u}| \rangle \langle \cos\theta \rangle \\ &\sim -2R\sqrt{\mathrm{Pe}} \langle \cos\theta \rangle \epsilon^{3/2}, \end{aligned} \tag{3.9}$$

where we used the definition of ϵ. We take $\langle \cos\theta \rangle = e^{-R/4}\epsilon/\sigma^2$, a model that agrees well with the simulations (Fig. 3-3). The effect of channeling at higher viscosity contrasts is to reduce $\langle |\boldsymbol{g}| \rangle$ (by reducing the total interfacial area) and realign the concentration gradient vector to become orthogonal to the velocity vector. Hence,

$$\frac{2}{\mathrm{Pe}} \langle \nabla\boldsymbol{u} : \boldsymbol{g} \otimes \boldsymbol{g} \rangle \sim -2R\sqrt{\mathrm{Pe}} e^{-R/4} \frac{\epsilon^{5/2}}{\sigma^2}. \tag{3.10}$$

Now, we model the diffusive term in Eq. (2.19),

$$\frac{2}{\mathrm{Pe}^2}\langle \nabla \boldsymbol{g} : \nabla \boldsymbol{g} \rangle = \frac{2}{\mathrm{Pe}^2}\langle |\nabla \boldsymbol{g}|^2 \rangle = \frac{2}{\mathrm{Pe}^2}\frac{\langle |\nabla \boldsymbol{g}|^2 \rangle}{\mathrm{var}(\boldsymbol{g})} \cdot \mathrm{var}(\boldsymbol{g}), \tag{3.11}$$

where $\mathrm{var}(\boldsymbol{g}) = \langle |\boldsymbol{g}|^2 \rangle - \langle |\boldsymbol{g}| \rangle^2$. Under the assumption of a unique characteristic transverse length scale in the problem,

$$\frac{\langle g_i^2 \rangle}{\langle |\nabla g_i|^2 \rangle} \sim \frac{\langle c^2 \rangle}{\langle |\nabla c|^2 \rangle}, \quad \frac{\langle g_i \rangle}{\langle |\nabla g_i|^2 \rangle} \sim \frac{\langle c \rangle}{\langle |\nabla c|^2 \rangle}. \tag{3.12}$$

Therefore, using the definition of the dissipation length scale s, we can write,

$$\frac{\mathrm{var}(g_i)}{\langle |\nabla g_i|^2 \rangle} \sim \frac{\mathrm{var}(c)}{\langle |\nabla c|^2 \rangle} = s^2 \tag{3.13}$$

For the diffusive term, this means,

$$\frac{2}{\mathrm{Pe}^2}\langle \nabla \boldsymbol{g} : \nabla \boldsymbol{g} \rangle \sim \frac{2}{\mathrm{Pe}^2}\frac{\langle |\nabla c|^2 \rangle}{\mathrm{var}(c)}\mathrm{var}(\boldsymbol{g}) = \frac{2}{\mathrm{Pe}}\frac{\epsilon}{\sigma^2}\mathrm{var}(\boldsymbol{g}). \tag{3.14}$$

If we can assume that $\langle |\boldsymbol{g}|^2 \rangle \sim \langle |\boldsymbol{g}| \rangle^2$, then $\mathrm{var}(\boldsymbol{g}) \sim \langle |\boldsymbol{g}|^2 \rangle = \epsilon \mathrm{Pe}$, which leads to

$$\frac{2}{\mathrm{Pe}^2}\langle \nabla \boldsymbol{g} : \nabla \boldsymbol{g} \rangle \sim 2\frac{\epsilon^2}{\sigma^2}. \tag{3.15}$$

This scaling for diffusive decay of ϵ provides insight into the relation among $d\epsilon/dt$, ϵ and σ^2: the rate of decay of the mean dissipation rate due to diffusion follows the non-monotonicity in ϵ, with its strength scaled by the variance, which is monotonic in time. Using this insight, we can further improve the model for the diffusive term. Using the ADE,

$$\begin{aligned} \frac{2}{\mathrm{Pe}^2}\langle \nabla \boldsymbol{g} : \nabla \boldsymbol{g} \rangle &\sim 2\langle (\partial_t c + \boldsymbol{u} \cdot \boldsymbol{g})^2 \rangle \\ &\sim 2\langle (\partial_t c)^2 + \partial_t c\, (\boldsymbol{u} \cdot \boldsymbol{g}) \rangle \end{aligned} \tag{3.16}$$

We model $\langle (\partial_t c)^2 \rangle \sim \frac{1}{\sigma^2}\left(\frac{d\sigma^2}{dt}\right)^2 \sim \epsilon^2/\sigma^2$, and $-\langle \partial_t c\, (\boldsymbol{u} \cdot \boldsymbol{g}) \rangle \sim \langle (\boldsymbol{u} \cdot \boldsymbol{g})^2 \rangle \sim \mathrm{Pe}\epsilon \langle \cos^2 \theta \rangle$. From Fig. 3-3 and the scaling of the diffusive term with ϵ and σ^2 found through

numerical simulation, we obtain

$$\frac{2}{\mathrm{Pe}^2}\langle \nabla \boldsymbol{g} : \nabla \boldsymbol{g} \rangle \sim \sqrt{R\mathrm{Pe}e^{-R/4}} \left(\frac{\epsilon}{\sigma}\right)^{5/2}. \tag{3.17}$$

Using Eqs. (3.10) and (3.17), the model equation for ϵ under viscous fingering ($R > 0$) becomes

$$\frac{d\epsilon}{dt} - AR\sqrt{\mathrm{Pe}}e^{-R/4}\frac{\epsilon^{5/2}}{\sigma^2} + B\sqrt{R\mathrm{Pe}e^{-R/4}} \left(\frac{\epsilon}{\sigma}\right)^{5/2} = 0, \tag{3.18}$$

where A and B are two model parameters. Eq. (3.18) has two terms corresponding to fingering-induced enhancement and diffusion-driven decrease in the dissipation rate. The advection-driven term is negative and gives the rising behavior in ϵ with time whereas the diffusion-driven term is positive and gives the declining behavior in ϵ. Above model is valid for $R > 0.5$, i.e., in presence of viscous fingering.

Eqs. (2.11) and (3.18) form a coupled system of first-order ODEs which can be solved with initial values of σ^2 and ϵ. This two-equation model is analogous to the k-epsilon models in turbulence [209]. We test the performance of the mixing model by comparing the predicted decay of variance and scalar dissipation rate with results from the direct numerical simulations (Fig. 3-4). Mixing times predicted from the model compare well with those obtained from the simulations, reaching a minimum around $R = 2.5$. Channeling of the less viscous fluid is persistent at high Pe, as shown by the surface of mixing time as a function of mobility ratio and Pe [Fig. 3-5].

3.2.3 Mixing model for fluids of equal viscosity

When the viscosities are equal, there is no viscous fingering and the two fluids mix due to diffusion only. The mixing model presented in Eq. (3.18) cannot capture evolution of the mean dissipation rate, ϵ, for fluids of equal viscosity as the modeled terms become zero for $R = 0$. An alternative is to use Eq. (3.15) for the diffusive term, i.e.,

$$\frac{d\epsilon}{dt} = -B\frac{\epsilon^2}{\sigma^2}. \tag{3.19}$$

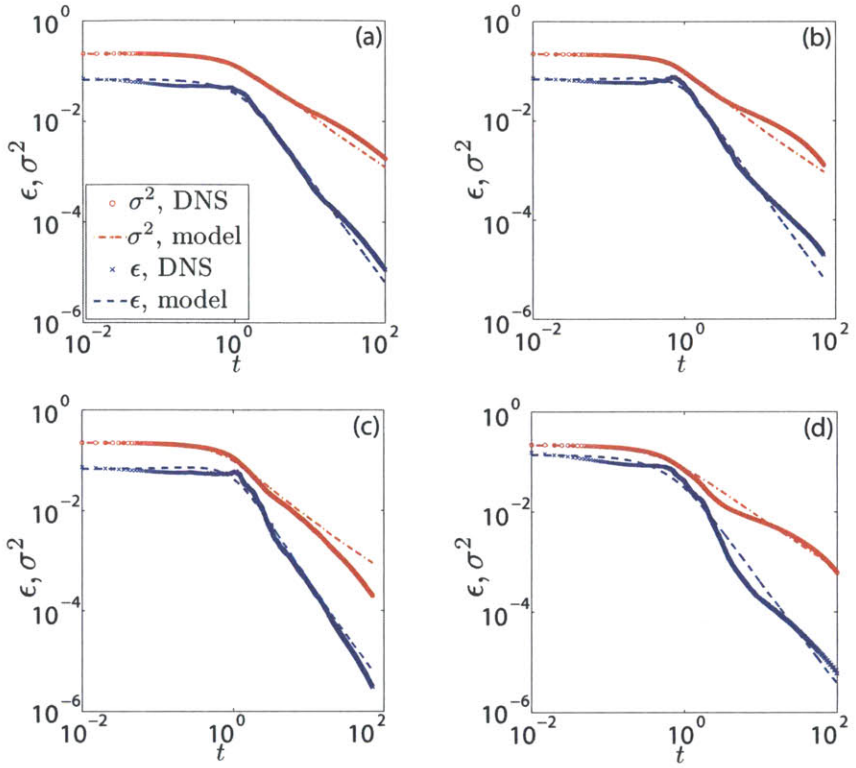

Figure 3-4: Performance of the mixing model given by Eqs. (2.11) and (3.18). Comparison of the evolution of ϵ and σ^2 in the simulation (DNS) and the proposed model for different values of R and Pe. (a) $R = 1$, Pe $= 10^4$. (b) $R = 2$, Pe $= 10^4$. (c) $R = 3$, Pe $= 10^4$. (d) $R = 3$, Pe $= 4 \times 10^3$. The same values of the two model parameters were used for all cases: $A = 0.76$, $B = 0.84$.

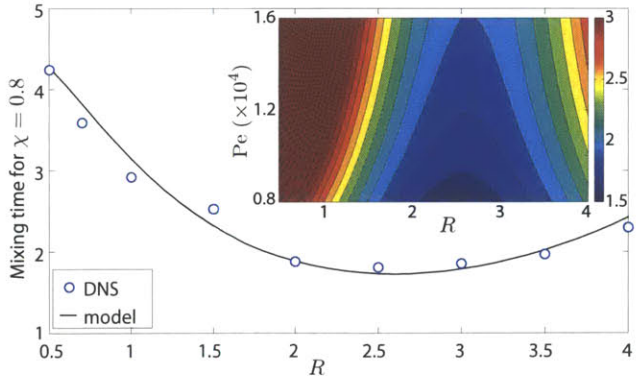

Figure 3-5: Mixing time, that is, time to reach 80% degree of mixing, plotted for different mobility contrasts and Pe=10^4, from both simulations and the $\sigma^2 - \epsilon$ model. Mixing time behaves non-monotonically with R, increasing at high R due to channeling. Inset: mixing time surface from the model as a function of R and Pe. $A = 0.76, B = 0.84$.

The evolution of mean dissipation rate, and therefore mixing, may involve interactions among the various interfaces in the domain if such interfaces are prescribed in the initial configuration of the concentration field. Eq. (3.19) does not take into account the effect of interactions among the interfaces into the evolution of mixing.

We derive an analytical model for evolution of ϵ for $R = 0$. Let's consider a two-dimensional square domain in $x \in [-0.5, 0.5]$, $y \in [-0.5, 0.5]$, which has two fluids of equal viscosity separated in the middle at $y = 0$ by a stable interface parallel to the x axis. The dimensionless velocity field is $\boldsymbol{u} = [1, 0]$ and the ADE can be solved analytically to obtain the concentration field as $c = \frac{1}{2}\left[1 - \text{erf}\left(\frac{y}{2}\sqrt{\frac{\text{Pe}}{t}}\right)\right]$. In absence of viscous fingering, there are no gradients along x and the mean scalar dissipation rate in this configuration becomes

$$\epsilon = \frac{1}{\text{WPe}} \int \left(\frac{dc}{dy}\right)^2 dy, \tag{3.20}$$

where W is the width of the domain. After substituting for c, we obtain an analytical solution for ϵ as

$$\epsilon = \frac{1}{2\sqrt{2\pi t \text{Pe}}} \text{erf}\left(\frac{W}{2}\sqrt{\frac{\text{Pe}}{2t}}\right). \tag{3.21}$$

Now, let's increase the number of interfaces from one to four in a stripe configuration (Fig. 3-6a), for which we can solve the ADE exactly to obtain,

$$\begin{aligned} c(x, y, t) = 1 + \frac{1}{2}\Bigg[&\text{erf}\left(\frac{y + 0.1}{2}\sqrt{\text{Pe}/t}\right) - \text{erf}\left(\frac{y - 0.1}{2}\sqrt{\text{Pe}/t}\right) \\ &- \text{erf}\left(\frac{y + 0.3}{2}\sqrt{\text{Pe}/t}\right) + \text{erf}\left(\frac{y - 0.3}{2}\sqrt{\text{Pe}/t}\right)\Bigg]. \end{aligned} \tag{3.22}$$

We can use Eq. (3.20) to calculate ϵ. The evolution of the interface thickness, and ϵ, transitions from power-law to exponential to an error-function-like behavior in time, with transition times depending on the initial configuration of the fluid interfaces. ϵ decays with time as $t^{-1/2}e^{-C_3 t}$, where C_3 is a positive constant. Assuming

$$\epsilon = \frac{C_1 e^{-C_3 t}}{C_2 + \sqrt{t}}, \tag{3.23}$$

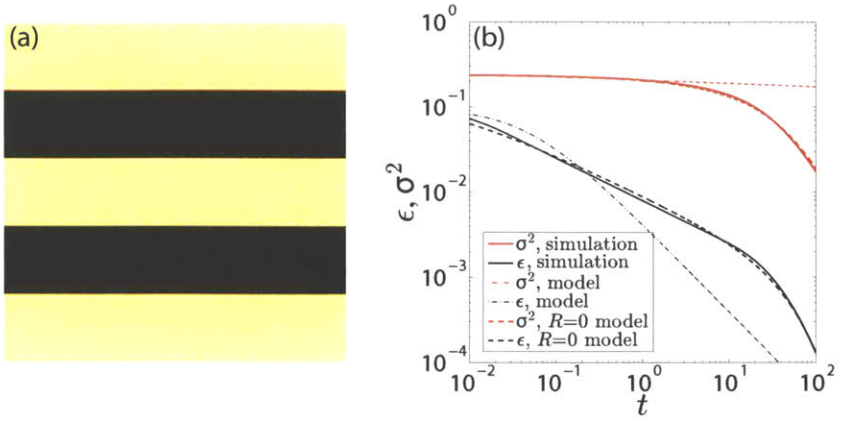

Figure 3-6: (a) Two fluids of equal viscosity in a stripe configuration at $t = 0$. Mean flow is from left to right and boundary conditions are periodic in both x and y directions. Pe = 10000. (b) Evolution of mixing quantities from the simulation (solid lines), from the diffusive model in Eq. (3.19) (thin dash-dot lines), and from the $R = 0$ model in Eq. (3.24) (thick dash lines). $B = 50, C_1 = 0.01, C_3 = 0.02$.

where C_1 and C_2 are also positive constants, we obtain the following model equation for evolution of ϵ,

$$\frac{d\epsilon}{dt} + C_3\epsilon + \frac{1}{2C_1}\frac{\epsilon^2}{\sqrt{t}e^{-C_3 t}} = 0, \tag{3.24}$$

where $C_1 = \mathrm{Pe}^{-1/2}$. This model agrees well with the results from numerical simulations of both the stripe configuration and the blobs configuration for $R = 0$ (Fig. 3-6b). Blobs configuration was introduced in Sec. 2.4.2.

3.3 Effective average viscosity

As a result of the exponential dependence of fluid viscosity on solvent concentration (Sec. 2.2), the average (effective) viscosity in the flow domain decreases as the less viscous fluid starts to mix with the more viscous one. The rate of decrease is faster at early times and slower at later times, giving rise to an inflection point in the evolution of the average viscosity. Since the rate of change in viscosity is linked to changes in interface length resulting from fingering, we hypothesize that ϵ and $d\overline{\mu}/dt$ are intimately related. Here, we present a relationship between the mean scalar dissipation rate, ϵ, and the domain average viscosity, $\overline{\mu}$.

The average mixture viscosity $\overline{\mu}$ can be expressed as

$$\overline{\mu} = \frac{1}{A_t} \int_0^1 \mu dA, \tag{3.25}$$

where dA is the area enclosed by contours $c = c^* + \delta c^*$ and $c = c^*$, and μ is the mixture viscosity inside dA and $A_t = 1$ is the total area of the domain. The area (mass) occupied by the fluid in regions where $c \leq c^*$ at a given time t is also the area enclosed by concentration isosurface $c = c^*$, and is defined as

$$A(c^*, t) \equiv \int_{c \leq c^*} dS, \tag{3.26}$$

Since the A–c and A–μ relations are one-to-one at any given time (Fig. 3-7), we can replace the integral in A with an equivalent integral in μ,

$$\overline{\mu} = \frac{1}{A_t} \int_1^{e^R} A d\mu. \tag{3.27}$$

Differentiating with respect to time,

$$\frac{d\overline{\mu}}{dt} = \frac{1}{A_t} \int_1^{e^R} \frac{\partial A}{\partial t} d\mu. \tag{3.28}$$

Using the the divergence-free velocity condition and the identity [190]

$$\oint_{c=c^*} \frac{(\,\cdot\,)}{|\nabla c|} dl = \frac{\partial}{\partial c^*} \int_{c \leq c^*} (\,\cdot\,)\, dS, \tag{3.29}$$

where the circuit integral is defined on the concentration contour $c = c^*$, we obtain

$$\frac{\partial}{\partial t} A(c^*, t) = -\frac{1}{\mathrm{Pe}} \frac{\partial}{\partial c^*} \int_{c \leq c^*} \nabla^2 c dS, \tag{3.30}$$

which is a statement that the contour area changes only due to diffusive flux (from fluid in $c > c^*$ region to the fluid in $c < c^*$ region) as pure advection conserves the contour area. Using Eq. (3.29), the right-hand-side term in Eq. (3.30) can be written

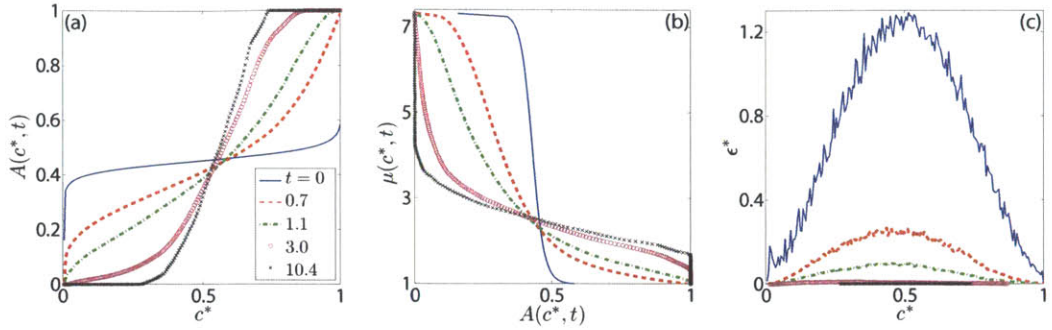

Figure 3-7: Evolution of the variables $A(c^*)$, $\mu(c^*)$ and ϵ^* during the simulation of mixing of blobs of more viscous fluid with $R = 2$, $\mathrm{Pe} = 10^4$ (Fig. 2-3). (a) Plot of $A(c^*, t)$, the area of the domain enclosed by the contour of $c = c^*$, that is, satisfying the inequality $c \leq c^*$ [Eq. (3.26)]. It is a monotonically increasing function of c^* that evolves in time due to mixing from a perfectly segregated state to a fully homogenized mixture. (b) Relation between the average viscosity $\mu(c^*)$ and contour area $A(c^*)$, which is a one-to-one relation at all times. High values of viscosity, in the range $\sim e^R$, are quickly suppressed due to mixing. (c) Plot of the conditional mean dissipation rate ϵ^* as a function of the contour concentration c^*, which satisfies that $\epsilon^* = 0$ at both $c^* = 0$ and $c^* = 1$.

as

$$\begin{aligned} \int_{c\leq c^*} \nabla^2 c dS = \oint_{c=c^*} \nabla c \cdot \boldsymbol{n} dl = \oint_{c=c^*} \nabla c \cdot \frac{\nabla c}{|\nabla c|} dl \\ = \frac{\partial}{\partial c^*} \int_{c\leq c^*} |\nabla c|^2 \, dS. \end{aligned} \tag{3.31}$$

Hence Eq. (3.30) can be transformed into

$$\frac{\partial}{\partial t} A(c^*, t) = -\frac{1}{\mathrm{Pe}} \frac{\partial}{\partial c^*} \left(\langle |\nabla c|^2 \rangle_{c^*} \frac{\partial A}{\partial c^*} \right), \tag{3.32}$$

where the average of a field on the tracer contour $c = c^*$ is defined as

$$\langle \cdot \rangle_{c^*} \equiv \frac{\partial}{\partial A} \int_{c\leq c^*} (\cdot) \, dS. \tag{3.33}$$

Eq. (3.32) can be expressed in terms of the mean dissipation rate,

$$\frac{\partial A}{\partial t} = -\frac{\partial}{\partial c^*} \left(\epsilon^* \frac{\partial A}{\partial c^*} \right), \tag{3.34}$$

where $\epsilon^* = \frac{1}{\mathrm{Pe}}\langle|\nabla c|^2\rangle_{c^*}$ is the conditional mean dissipation rate of scalar variance for $c = c^*$. Integrating ϵ^* with respect to A,

$$\begin{aligned}\int_0^1 \epsilon^* dA &= \frac{1}{\mathrm{Pe}} \int_{c^*=0}^{c^*=1} d\left(\int_{c\le c^*} |\nabla c|^2 \, dS\right) \\ &= \frac{1}{\mathrm{Pe}} \left[\int_{c\le c^*} |\nabla c|^2 \, dS\right]_{c^*=0}^{c^*=1} \\ &= \frac{1}{\mathrm{Pe}} \int |\nabla c|^2 \, dS = A_t \epsilon,\end{aligned} \tag{3.35}$$

and using Eq. (3.34), we obtain

$$\frac{d\overline{\mu}}{dt} = -\frac{1}{A_t} \int_1^{e^R} \frac{\partial}{\partial c^*} \left(\epsilon^* \frac{\partial A}{\partial c^*}\right) d\mu. \tag{3.36}$$

For our viscosity model $\mu(c) = e^{R(1-c)}$, $d\mu = -R\mu dc$, so

$$\begin{aligned}\frac{d\overline{\mu}}{dt} &= \frac{R}{A_t} \int_1^0 \mu \frac{\partial}{\partial c^*} \left(\epsilon^* \frac{\partial A}{\partial c^*}\right) dc \\ &= -\frac{R}{A_t} \int_{c^*=0}^{c^*=1} \mu d\left(\epsilon^* \frac{\partial A}{\partial c^*}\right).\end{aligned} \tag{3.37}$$

Since $\epsilon^* = 0$ at $c^* = 0$ and $c^* = 1$ (Fig. 3-7),

$$\begin{aligned}\frac{d\overline{\mu}}{dt} &= -\frac{R}{A_t} \left[\left(\mu\epsilon^* \frac{\partial A}{\partial c^*}\right)_{\epsilon^*=0}^{\epsilon^*=0} - \int_{e^R}^1 \epsilon^* \frac{\partial A}{\partial c^*} d\mu\right] \\ &= -\frac{R}{A_t} \int_0^1 \epsilon^* \frac{\partial A}{\partial c^*} R\mu dc = -\frac{R^2}{A_t} \int_0^1 \mu\epsilon^* dA \\ &\sim -\frac{R^2\overline{\mu}}{A_t} \int_0^1 \epsilon^* dA.\end{aligned} \tag{3.38}$$

Finally, using Eq. (3.35) in Eq. (3.28), we obtain the desired relation:

$$\frac{d\overline{\mu}}{dt} \sim -R^2\overline{\mu}\epsilon, \tag{3.39}$$

or, equivalently,

$$\frac{d\log\overline{\mu}}{dt} \sim -R^2\epsilon. \tag{3.40}$$

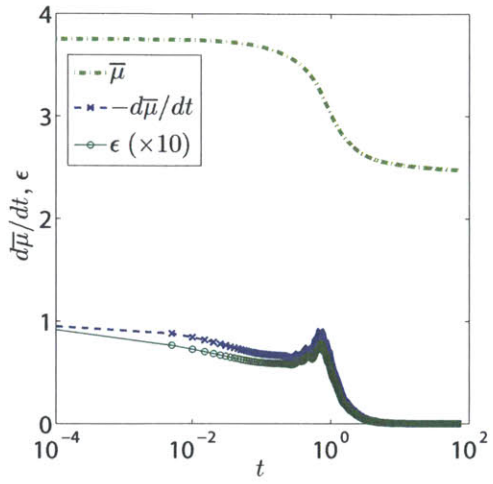

Figure 3-8: Relationship between the rate of decrease in average viscosity and the mean scalar dissipation rate [Eq. (3.39)]. The inflection point in the average viscosity curve, which corresponds to a minimum in the $d\overline{\mu}/dt$, occurs at the same time as ϵ reaches its maximum. The numerical simulations correspond to $R = 2$ and $\mathrm{Pe} = 10^4$.

Thus, our analysis suggests that the rate of decrease in mixture viscosity is directly proportional to the mean dissipation rate and that, as a result, a maximum ϵ corresponds to a maximum (with negative sign) in $d\overline{\mu}/dt$. This result, which is confirmed by direct numerical simulations (Fig. 3-8), could allow the determination of ϵ in a lab experiment where average viscosity is being measured at discrete time intervals.

3.4 Discussion and conclusions

Viscous fingering acts as an agent for enhanced mixing by creating additional interfacial area and disorder in the flow field. The rate of mixing quantified through the mean scalar dissipation rate, ϵ, increases at early times as additional interface is created through finger stretching and tip-splitting.

The impact of the viscous instability on mixing, however, is nontrivial. For moderate viscosity contrasts (roughly $M < 10$, or $R < 2.5$), larger M implies a larger increase in ϵ due to fingering, and therefore faster mixing. However, as M is increased beyond a value of 10, channeling of the less viscous fluid starts to dominate the flow, leading to flow focusing across the entire flow domain and inhibiting the growth of adjacent fingers. As a result of this channeling phenomenon, which slows down the

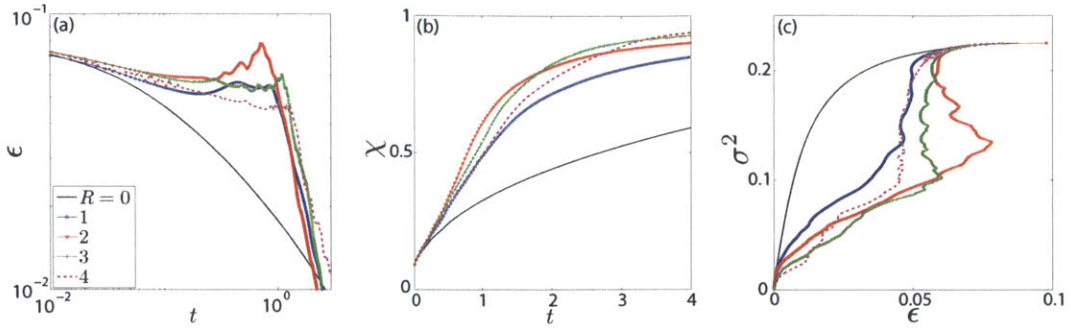

Figure 3-9: (a) Evolution of the mean scalar dissipation rate ϵ. (b) Evolution of the degree of mixing $\chi = 1 - 4\sigma^2$. (c) Crossplot of σ^2–ϵ, for different values of the viscosity ratio, and $\mathrm{Pe} = 10^4$. The largest hump in dissipation rate, which leads to fastest initial mixing, occurs for $R \sim 2.5$.

creation of additional interface area, growth in ϵ is not only delayed but also limited in the magnitude (Fig. 3-9). Hence, in this regime of very large viscosity contrast, mixing is less efficient. Fastest mixing is achieved at an optimum viscosity ratio that maximizes the creation of fluid-fluid interfacial area across which diffusive mixing takes place. Channeling and tip-splitting play an important role in this balancing act, which makes degree of mixing a nonmonotonic function of the viscosity contrast.

We presented an upscaled model of fingering-driven mixing under the assumption of statistical homogeneity. The model captures the characteristic stretching of the material interface over which diffusive mixing takes place. It takes the form of two coupled Ordinary Differential Equations (ODE) to be solved for the concentration variance and the mean scalar dissipation rate and it reproduces accurately the evolution of these two quantities as observed in high-resolution numerical simulations. At the heart of the model, which is inspired by turbulence modeling, is the recognition that the properties of the velocity field (through modeling of the mechanical dissipation rate) are essential in the homogenization of concentration gradients. We guided and validated the model by means of direct numerical simulations of miscible viscous fingering over a large range of viscosity ratios and Péclet numbers. For values of the viscosity ratio larger than 20, the traditional (and very efficient) streamfunction–vorticity formulation is numerically unstable. We used a high-resolution implicit mobility numerical method that, while being computationally more expensive, guar-

antees stability and allowed us to obtain fully-resolved simulations of the fingering phenomenon.

Chapter 4

Synergetic fluid mixing from viscous fingering and alternating injection

4.1 Introduction

Efficient fluid mixing at low Reynolds numbers is challenging, because one cannot rely on either turbulence or inertial effects to induce disorder in the velocity field. Several strategies have been proposed to achieve fast mixing in small devices such as microfluidic cells [244, 198], including grooved walls [245], bubble capillary flows [102], pulsating injection [106], electroosmosis [107], electrokinetics [210], and acoustic stimulation [97]. Alternating injection of two fluids has also been proposed to enhance mixing in laminar-flow conditions [174, 51].

Recently, we have shown that miscible viscous fingering—a hydrodynamic instability that takes place when a less viscous fluid displaces a more viscous fluid—can enhance mixing in periodic Darcy flows, such as flows in Hele-Shaw cells or porous media [135]. Enhanced mixing due to viscous fingering emerges from the velocity disorder and the additional interfacial area created between the two fluids as a result of the hydrodynamic instability. Creation of new fluid-fluid interfaces is accelerated

by tip-splitting of the fingers and retarded by channeling, which are the two primary mechanisms controlling the dynamics of viscous fingering [135, 125, 279, 184]. Fluid mixing from viscous fingering is determined by the delicate balance of these two mechanisms. Such a balance results in nontrivial mixing behavior as the viscosity contrast between the two fluids is increased. For periodic flows, high-resolution simulations have shown that there is an optimum viscosity contrast for fastest mixing [135].

Periodic flows, however, while conceptually important to gain understanding, are difficult to achieve in practice. Here, we study mixing of two miscible fluids of different viscosities in a microfluidic channel or porous medium due to the combined effect of viscous fingering and alternating injection, and find that the two can act synergistically to achieve rapid mixing at low Reynolds numbers and high Péclet numbers, typical of microfluidic flows. We perform high-resolution numerical simulations that elucidate the phenomenon and guide us to formulate a macroscopic model that captures the universal signature of mixing from viscous fingering and alternating injection. Previous studies of viscous fingering in alternating injection [47, 64, 184] analyze *spreading* of a single slug as a result of viscous fingering, where the quantities of interest are the transverse-averaged concentration and the longitudinal variance of the concentration field. However, it is *mixing*, not spreading, that controls chemical reactions and dilution of peak concentrations [69], a process that requires estimating the variance of the concentration field [159, 32]. We then use our theory to address important practical questions, such as: (1) what is the minimum streamwise distance required to achieve a prescribed degree of mixing inside the channel; and (2) is there an optimum viscosity ratio that exploits the synergy between viscous fingering and alternating injection to promote mixing while hampering channeling?

4.2 Mathematical model

We consider flow of two fluids of different viscosities μ_1 and μ_2, where $\mu_1 < \mu_2$, through a homogeneous two-dimensional porous medium or a Hele-Shaw cell (two parallel plates separated by a thin gap). We adopt a Darcy formulation, which is well

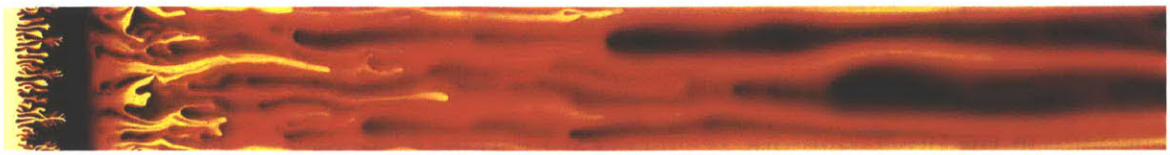

Figure 4-1: Snapshot of the concentration field during the alternating injection of more viscous (dark) and less viscous (light) fluids. Viscous fingering at the displacement front promotes mixing of the two fluids. At high viscosity contrast, however, a few dominating fingers coalesce to form persistent channels. These channels serve as preferential pathways for subsequent slugs of the less viscous fluid, inhibit transverse mixing, and shield growth of adjacent fingers. The displacement corresponds to a viscosity ratio $M \approx 33$ ($R = 3.5$) and Péclet number $\mathrm{Pe} = 2000$. See supplementary videos [1].

accepted for single-phase flows in porous media [18] and has been used extensively to model flow in a Hele-Shaw cell for a range of Péclet numbers and viscosity ratios [22, 125, 249, 279, 219, 63]. Although three-dimensional effects could play a role in a viscously-unstable Hele-Shaw flow, these would require 3D Stokes simulations that would incur a formidable computational cost, and likely would not introduce a fundamental qualitative departure from our findings. The porosity ϕ and permeability k are constant. The length and width of the domain are L and W, respectively. We define concentration c as the volume fraction of the less viscous fluid in the mixture. We assume that the more viscous fluid completely fills the cell initially. We assume an exponential viscosity model $\mu(c) = \mu_1 e^{R(1-c)}$ where $R = \ln M$ and $M = \mu_2/\mu_1$ is the viscosity contrast. We simulate alternating injection, in which one cycle corresponds to a slug of the less viscous fluid entering the flow cell at constant rate from the left boundary followed by a slug of the more viscous fluid at the same rate. Let $A_s = \phi W l_s$ be the volume of the less viscous slug. The mean velocity is in the x-direction and of magnitude U. The outlet is a natural outflow boundary. The two fluids are assumed to be first-contact miscible, neutrally buoyant and incompressible. First-contact miscibility means the fluids mix instantaneously in all proportions to form a single phase and surface tension effects are absent. Like in many previous studies on viscous fingering [45, 219, 63, 64], the diffusion coefficient D between the fluids is assumed to be constant, isotropic and independent of concentration. Although D likely is velocity-dependent, this effect appears not to play a major role

on macroscopic features of viscous fingering at high Péclet numbers and late times [279], and a hydrodynamic dispersion model for flows with large viscosity contrast, especially in the pre-asymptotic regime, is still lacking [206, 219].

To non-dimensionalize the system, we choose the "slug length" l_s as the characteristic length, U as the characteristic velocity, μ_1 as the characteristic viscosity, $P = \mu_1 U l_s/k$ as the characteristic pressure, and $T = \phi l_s/U$ as the characteristic time. The governing equations in dimensionless form are Eq. (2.3) [249] in $x \in [0, L/l_s]$ and $y \in [0, W/l_s]$ where $\boldsymbol{u} = [u, v]$ and p are the velocity and pressure fields. The initial condition is $c|_{t=0} = 0$. The boundary conditions are $c|_{y=0} = c|_{y=W/l_s}$(periodic in y), $\boldsymbol{u} \cdot \boldsymbol{n}|_{x=0} = -1$ (inflow), $p|_{x=L/l_s} = 0$ (outflow) and alternating injection

$$(\boldsymbol{u} \cdot \boldsymbol{n})c|_{x=0} = \begin{cases} -1, & \text{if } 0 < \text{rem}(t, 1/r_s) \leq 1, \\ 0, & \text{if } 1 < \text{rem}(t, 1/r_s) < 1/r_s, \end{cases} \tag{4.1}$$

where $\boldsymbol{n}$ is the outward unit normal and rem$(\cdot)$ is the remainder function. We fix the aspect ratio $L/W = 8$ and the slug ratio $r_s = 0.5$ (1 : 1 fluid volume ratio). The slug ratio is also the dimensionless concentration of the perfectly mixed fluid. The dimensionless parameters governing fluid mixing are the Péclet number $\text{Pe} = U l_s/D$, the log-viscosity contrast R in the viscosity law, and the dimensionless length L/l_s of the channel. The dimensionless diffusive timescale for mixing is $t_{\text{diff}} = \text{Pe}$.

We discretize Eq. (2.3) using sixth-order compact finite differences in the streamwise direction and the Fast Fourier Transform (FFT) in the transverse direction, which is periodic [136, 219, 45]. We advance in time using a third-order Runge-Kutta scheme. To gain numerical stability at high M, we solve the pressure equation Eq. (2.4) directly using finite volumes with a two-point flux approximation, instead of using the stream function vorticity approach [249]. Fig. 4-1 shows a snapshot of the concentration field from an alternating-injection simulation.

4.3 Three regions of mixing

Fluid mixing results in decay of the concentration variance, and the mean scalar dissipation rate determines the rate of this decay [209, 159, 135, 124]. To investigate mixing in a channel under alternating injection, we study the transversely averaged profiles of the degree of mixing and the scalar dissipation rate. While these profiles oscillate with time as the slugs of the two pure fluids enter the domain in alternating fashion, time-averaging leads to slowly-varying longitudinal profiles. We define the longitudinal concentration variance $\overline{\sigma^2}(x,t) \equiv \overline{c^2} - \overline{c}^2$, the longitudinal degree of mixing $\overline{\chi}(x,t) \equiv 1 - \overline{\sigma^2}/\sigma^2_{\max}$, and the longitudinal scalar dissipation rate $\overline{\epsilon}(x,t) \equiv \overline{|\boldsymbol{g}|^2}/\mathrm{Pe}$, where $\boldsymbol{g} \equiv \nabla c$. Overbar operator denotes averaging in the transverse direction and in time,

$$\overline{(\cdot)} \equiv \int_0^{W/l_s} \int_{t-t_w/2}^{t+t_w/2} (\cdot)\, dt' dy, \tag{4.2}$$

where t' is a dummy variable for integration, and t_w is the time window of averaging. We average over a time window of three injection cycles. We also verified that a time window of one injection cycle gives similar results.

The fundamental observation is the development of three distinct mixing regions along x (Fig. 4-2). Region I, closest to the inlet, is a region of active mixing as a result of the vigorous interaction between fingers from intermittent injection of the less-viscous fluid. Region II is a well-mixed region, whose extent grows over time. Region III is a region of poorly mixed fluid ahead of the well-mixed region, dominated by the presence of channels of well-mixed fluid that penetrate through the ambient, more viscous fluid. We have confirmed with simulations (not shown here) that the behavior of the system is qualitatively and quantitatively the same even if the effect of Korteweg stresses [47] is included in the formulation.

The key descriptor of the flow is the location of the well-mixed front $x_f(t)$ separating Regions II and III, as a function of time. This front corresponds to the position at which the average degree of mixing is maximum, $\overline{\chi}_f(t) = \max_x \overline{\chi}(x,t)$ [Fig. 4-2(e)]. It also corresponds to the point at which the transverse average of the scalar dissipation rate is minimum, $\overline{\epsilon}_f(t) = \min_x \overline{\epsilon}(x,t)$ [Fig. 4-2(f)].

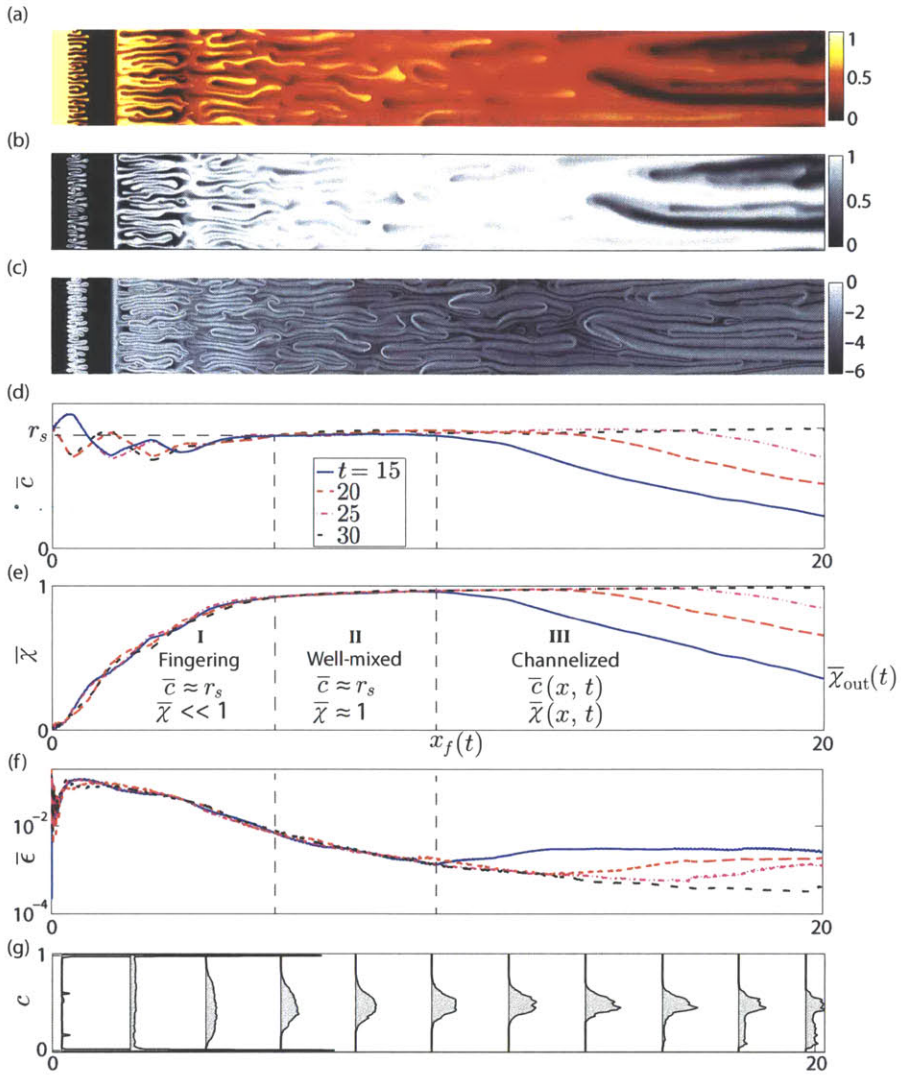

Figure 4-2: (a) Concentration c, (b) degree of mixing χ, and (c) scalar dissipation rate $\log \epsilon$ from an alternating injection simulation with viscosity ratio $M = \exp(2) \approx 7$ and Péclet number $\text{Pe} = 2000$ at time $t = 18.6$. The degree of mixing is high (red) where mixing has already taken place. Scalar dissipation rate is high (red) at the interfaces where the fluid is actively being mixed. (d), (e), and (f) are longitudinal profiles of concentration $\overline{c}$, degree of mixing $\overline{\chi}$, and scalar dissipation rate $\overline{\epsilon}$, averaged over a moving time-window (of duration equal to 3 injection cycles, although the same behavior holds for different averaging windows). $\overline{\epsilon}$ reaches a maximum where fingering begins and a minimum where channeling begins, congruent with a non-monotonic degree of mixing $\overline{\chi}$ with x. (g) The time-averaged PDF of concentration evolves from two delta-like functions (segregated pure fluids near $x = 0$ in Region I) to a Gaussian-like function (well-mixed fluids in Region II) to an anomalous distribution (channeling in Region III). The vertical dashed lines indicate the boundaries of the three mixing regions at time $t = 15$; x_f denotes the position of the well-mixed front, which is the position of the maximum longitudinal degree of mixing in the domain, $\overline{\chi}_f$, at a given time.

4.4 Mixing model

We now formalize these qualitative observations and develop an analytical model of the average degree of mixing in the channel. We formulate two submodels: one for the channelized region (III), and one for the active-mixing and well-mixed regions (I and II). Each submodel originates from the exact average equations of mean concentration $\overline{c}$, concentration variance $\overline{\sigma^2}$ and mean scalar dissipation rate $\overline{\epsilon}$. For example, we obtain the exact equations for $\overline{c}$ and $\overline{c^2}$ by premultiplying the advection–diffusion equation (2.3) by 1 and c, respectively, integrating in y, making use of the divergence theorem and incorporating periodicity in y:

$$\partial_t \overline{c} + \partial_x \left(\overline{uc} - \frac{1}{\mathrm{Pe}} \partial_x \overline{c} \right) = 0, \tag{4.3}$$

$$\partial_t \overline{c^2} + \partial_x \left(\overline{uc^2} - \frac{1}{\mathrm{Pe}} \partial_x \overline{c^2} \right) = -2\overline{\epsilon}. \tag{4.4}$$

4.4.1 Fractional flow model

Region III is characterized by channeling, where the less viscous fluid spreads longitudinally through fast-moving channels ahead of the well-mixed front. This dominance of heterogeneous fluid displacement over mixing suggests that we can pose a hyperbolic model by neglecting diffusion. The development of hyperbolic models (also called fractional flow formulations) of *average* concentrations that capture the fingering-enhanced *spreading* has a long history [28, 117, 153]. Here, we extend this approach to develop a hyperbolic fractional-flow model of *mixing*, which of course must involve higher-order moments of the concentration field. Neglecting diffusion in Eqs. (4.3)–(4.4) (that is, taking $\mathrm{Pe} \to \infty$), we obtain a hyperbolic approximation for the propagation of the mean concentration and the mean scalar energy: $\partial_t \overline{c} + \partial_x \overline{uc} = 0$, and $\partial_t \overline{c^2} + \partial_x \overline{uc^2} = 0$, respectively. Combining these equations we immediately obtain a hyperbolic approximation for the average degree of mixing $\overline{\chi}$:

$$\partial_t \overline{\chi} + \partial_x \overline{u\chi} = 0. \tag{4.5}$$

We provide closure for this equation with a fractional flow formulation, in which we model $\overline{u\chi}$ as a function of $\overline{\chi}$ alone: the fractional flow function $f(\overline{\chi})$. Different models of the fractional flow function have been proposed for the *mean* concentration [153, 257, 82]. Here we use

$$f(\overline{\chi}) = \frac{M_{\text{eff}}\overline{\chi}}{1 + (M_{\text{eff}} - 1)\overline{\chi}}, \; M_{\text{eff}} = (\alpha + (1-\alpha)M^{\frac{1-r_s}{4}})^4 \tag{4.6}$$

where α is the mixing ratio, defined as the degree of mixing in the 'effective' displacing fluid in the channelized region III, and M_{eff} is the *effective* viscosity ratio of the more viscous to the less viscous fluid in the channelized region, estimated using the quarter-power mixing rule. Eq. (4.6) is based on Koval's model [153], modified for region III where the less-viscous fluid in the channels—with average concentration $c = r_s$—displaces the more-viscous fluid with $c = 0$. The function (4.6) is concave, so the solution to Eq. (4.5) is a rarefaction wave where the derivative $\zeta = f'(\overline{\chi})$ is the speed of propagation of degree of mixing $\overline{\chi}$ [60]. The solution at different times can therefore be understood as a simple stretching of the characteristic velocity ζ.

We test the validity of this fractional flow model by comparing the model predictions with direct numerical simulations (Fig. 4-3). In the channeling region, the averaged degree of mixing from simulations indeed behaves as a continuous rarefaction wave that stretches with time, and this is captured nicely by the analytical model. From the profiles of average degree of mixing at different times in the channelized region we compute the numerical fractional flow function, which is well approximated for a wide range of viscosity contrasts M by function (4.6) with a single value of the mixing ratio, $\alpha = 0.5$ (Fig. 4-3, inset).

4.4.2 Dissipation model

We now turn our attention to modeling Regions I and II. Because these are regions of active mixing, one cannot neglect diffusion. We develop a mixing model from the exact equations of average concentration variance $\overline{\sigma^2}$ and average scalar dissipation rate $\overline{\epsilon}$. We obtain the former by combining Eqs. (4.3)–(4.4) and the latter by taking

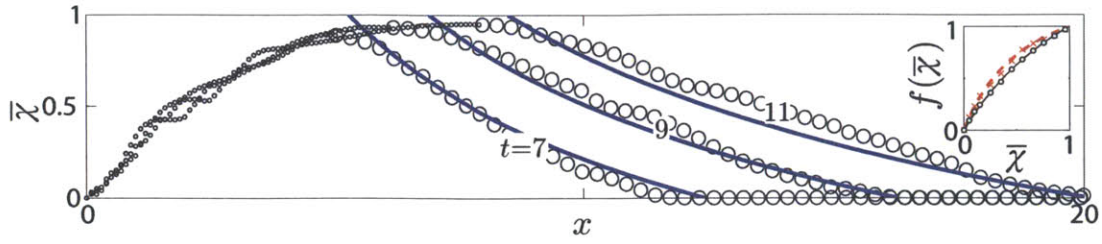

Figure 4-3: Time evolution of the profiles of average degree of mixing $\overline{\chi}$, for $R = 2$ and $\mathrm{Pe} = 2000$. The results from averaging a high-resolution simulation in the channelized region (large circles) are well captured by the hyperbolic mixing model (blue solid lines). Shown are three different times ($t = 7$, 9 and 11) that illustrate the self-similar $x \sim t$ character of the degree of mixing in the channelized region. Inset: fractional flow function obtained from averaging of the direct numerical simulations (symbols) and from the proposed model (4.6) with $\alpha = 0.5$, for $R = 2$ (black, circles) and $R = 3.5$ (red, crosses).

the gradient of the advection–diffusion equation (2.3) and then the dot product with ∇c, integrating in y and exploiting periodicity in y:

$$\partial_t \overline{\sigma^2} + \partial_x \left(\overline{uc^2} - \frac{1}{\mathrm{Pe}} \partial_x \overline{\sigma^2} \right) - 2\overline{c}\partial_x(\overline{uc}) = -2\overline{\epsilon}, \tag{4.7}$$

$$\partial_t \overline{\epsilon} + \partial_x \left(\overline{u\epsilon} - \frac{1}{\mathrm{Pe}} \partial_x \overline{\epsilon} \right) = -\frac{2}{\mathrm{Pe}} \overline{\nabla \boldsymbol{u} : \boldsymbol{g} \otimes \boldsymbol{g}} - \frac{2}{\mathrm{Pe}^2} \overline{\nabla \boldsymbol{g} : \nabla \boldsymbol{g}}. \tag{4.8}$$

The advective terms (involving u) are responsible for creation and preservation of fluid–fluid interfaces. Diffusive terms containing Pe in Eq. (4.7) and Pe^2 in Eq. (4.8) are responsible for decay of the interfaces, and they lead to a decrease in $\overline{\sigma^2}$.

From Figs. 4-2 and 4-3, it is clear that in Regions I and II the average degree of mixing $\overline{\chi}$ reaches a steady-state profile, and therefore can be described as a function of x only. The fundamental observation is that the flow approaches statistical homogeneity due to the many tip-splitting and finger-merging events and that the diffusive component of the generalized flux is much smaller than the advective component, $\partial_{xx}\overline{(\cdot)}/\mathrm{Pe} \ll \partial_x \overline{u(\cdot)}$. As a result, $\partial_t \overline{c} + \partial_x \overline{uc} = 0$, and $\partial_t \overline{c^2} + \partial_x \overline{uc^2} = -2\overline{\epsilon}$. The spatial variation in average quantities ($\overline{c}$, $\overline{c^2}$, $\overline{\epsilon}$) can be understood as the temporal variation of a parcel of fluid moving with mean velocity $\overline{u}$ (= 1 in the nondimensional

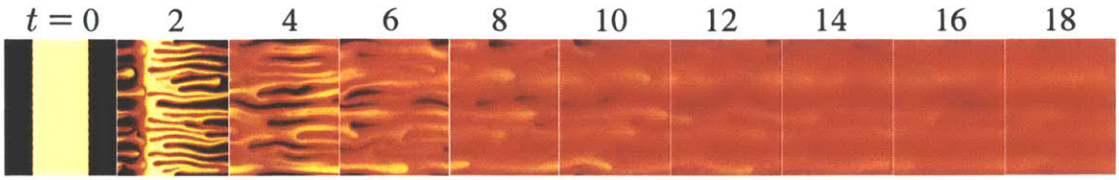

Figure 4-4: Snapshots from a periodic-flow simulation at successive times for $R = 2$ and $\mathrm{Pe} = 2000$. Notice the similarity with an alternating injection simulation (Fig. 4-2), especially away from the inlet and outlet boundaries. The domain length in the periodic simulation corresponds to one injection cycle: in this case, one-tenth of the domain length in the alternating injection simulation.

equations). In other words, we can approximate $\partial_t\overline{(\cdot)} + \partial_x\overline{u(\cdot)} \approx d\overline{(\cdot)}/dt$. This is illustrated in Fig. 4-4, which shows that a concatenation of snapshots from a simulation in a periodic domain of length equal to one injection cycle, under the space-time mapping $x = t$, closely resembles the concentration field in regions I and II in the full simulation of alternating injection [Fig. 4-2(a)].

From our key observation of space–time duality, the final approximate equations that require modeling are the average variance and scalar dissipation rate in a biperiodic domain.

$$\frac{d\overline{\sigma^2}}{dt} = -2\overline{\epsilon}, \tag{4.9}$$

$$\frac{d\overline{\epsilon}}{dt} = -\frac{2}{\mathrm{Pe}}\overline{\nabla \boldsymbol{u} : \boldsymbol{g} \otimes \boldsymbol{g}} - \frac{2}{\mathrm{Pe}^2}\overline{\nabla \boldsymbol{g} : \nabla \boldsymbol{g}}. \tag{4.10}$$

A macroscopic model of Eqs. (4.9)–(4.10), representing mixing due to viscous fingering under periodic boundary conditions, was recently developed [135, 136]. The model is a set of two ODEs governing the temporal evolution of $\overline{\sigma^2}$ and $\overline{\epsilon}$ (Eqs. (2) and (8) in [135]). The model provides closure of the higher-order terms in the exact equations based on the insights from high-resolution numerical simulations. We have confirmed that the predictions from this analytical model are in excellent agreement with direct numerical simulations of alternating injection (Fig. 4-5), and we refer to [135, 136] for the details of this mixing–dissipation model.

The space–time $(x - t)$ duality between the alternating injection flow and the periodic flow is valid for the entire length of the channel when $R = 0$ because viscous

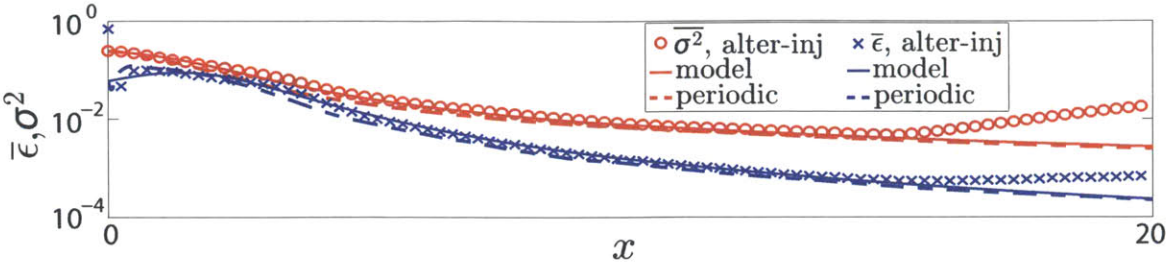

Figure 4-5: Average concentration variance ($\overline{\sigma^2}$, red) and scalar dissipation rate ($\overline{\epsilon}$, blue) from the alternating injection simulations (symbols), the analytical dissipation model (thin solid lines), and periodic simulations (dashed lines) for $R = 2$, Pe $= 2000$, at time $t = 22$. The results from the periodic simulation are computed by averaging over the entire volume at every time step, and the x-axis for these curves is time t. The values of the constants in the dissipation model [135] are: $A = 0.89$, $B = 0.51$. The model departs from the simulations ahead of the well-mixed front x_f, where the hyperbolic model applies instead (Region III, Fig. 4-3).

fingering and channeling are absent. The slugs exit the domain just as they enter except for smearing at the interfaces due to diffusion. The pseudo steady state degree of mixing oscillates between 0 and 1 throughout the length of the channel. We can obtain the mean behavior by averaging over a time-window and thereby removing the oscillations due to the alternating injection inlet boundary. We plot the longitudinal scalar dissipation rate, $\overline{\epsilon}$, and longitudinal degree of mixing, $\overline{\chi}$, in Fig. 4-6. In a purely diffusive process, the average degree of mixing increases proportional to square root of time. Because of the space–time duality, the longitudinal degree of mixing increases as square root of the downstream distance, $\overline{\chi} \approx \sqrt{x/\mathrm{Pe}}$. For $R = 0$, we can approximate $\overline{\epsilon}$ as a measure of the rate of change in $\overline{\chi}$ with x, because of the duality between the periodic flow and the alternating injection flow. More precisely,

$$\overline{\epsilon} = \frac{0.2}{\sqrt{x\mathrm{Pe}}}, \quad \overline{\chi} = 3.2\sqrt{\frac{x}{\mathrm{Pe}}}, \quad x < 0.1\mathrm{Pe}. \tag{4.11}$$

The condition on the distance results from the fact that $\overline{\chi} \leq 1$. For $x \geq 0.1\mathrm{Pe}$, $\overline{\chi} \approx 1$. We can obtain the above relations from an approximate solution to the ADE, which for $R = 0$ becomes a diffusion equation on a moving reference frame, with alternating-injection boundary condition. Above model agrees well with the simulation, especially away from the inlet as the effect of the alternating injection weakens (Fig. 4-6). The

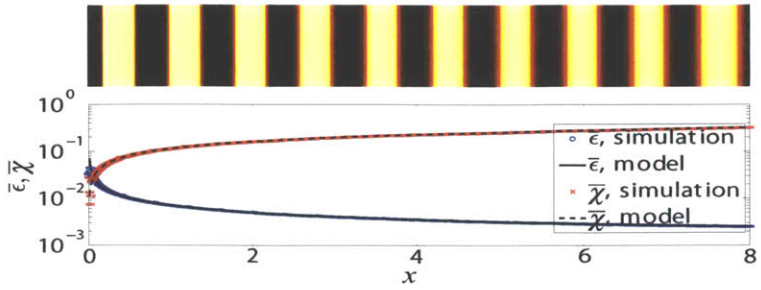

Figure 4-6: Profiles of the longitudinal dissipation rate (blue circles) and the longitudinal degree of mixing (red crosses) along the length of the cell for $R = 0, \mathrm{Pe} = 2000$. Solid and dash black lines are the theoretical predictions (Eq. (4.11)).

model can also be expressed as

$$\frac{d\overline{\sigma^2}}{dx} = -2\overline{\epsilon}, \tag{4.12}$$

where we have used the fact that the dimensionless mean speed in x is unity ($\overline{u} = 1$). Notice the similarity with Eq. (2.11), which governs temporal rate of decay of the volume-averaged concentration variance in a periodic domain. This further confirms the space–time duality between alternating injection simulation and periodic simulation.

4.5 Results

We now put the two submodels together: the dissipation model in Regions I and II, and the hyperbolic model in Region III. As a function of downstream distance x, the average degree of mixing increases monotonically (from 0) in regions I and II, and decreases monotonically (towards 0) in region III. Therefore, for a given time, the two curves given by each submodel will always cross. We define the location of the well-mixed front x_f as the point where $\overline{\chi}$ is maximum—which is modeled as the intersection of the two submodels. We use the analytical model to explore the influence of the system parameters on mixing efficiency by considering two practical measures: the minimum time to achieve a desired degree of mixing [Fig. 4-7(a)], and the maximum degree of mixing at the outlet (that is, the degree of mixing of the effluent mixture at long times) [Fig. 4-7(b)]. We find that a viscosity contrast between

the fluids leads to a dramatic increase in mixing efficiency. Mixing from alternating injection of equal-viscosity fluids ($R = 0$) is extraordinarily inefficient at all practical Péclet numbers [Fig. 4-7(a)]. Our analysis provides a natural explanation for the effect of slug size. Decreasing slug size l_s (that is, increasing alternating-injection frequency) leads to both a decrease in Péclet number $\mathrm{Pe} = Ul_s/D$ and an increase in dimensionless channel length L/l_s, and therefore results in a higher degree of mixing [Fig. 4-7(b)]. Mixing efficiency, however, does not necessarily increase uniformly with viscosity contrast between the fluids. For a given Péclet number and dimensionless channel length, there is a viscosity contrast for which the attainable degree of mixing of the effluent mixture is maximized. This optimum viscosity contrast promotes rapid creation of interfacial area from viscous fingering while disallowing strong channeling effects.

4.6 Conclusion

We have shown that the synergetic action of alternating injection and viscous fingering leads to a dramatic increase in efficiency when mixing fluids at high Péclet numbers—a notoriously challenging problem in the context of planar microfluidic devices as lab-on-a-chip systems [122, 7]. Based on observations from high-resolution simulations, we develop a theoretical model of mixing efficiency that combines a hyperbolic mixing model of the channelized region ahead, and a mixing-dissipation model of the pseudosteady region behind. Our macroscopic model quantitatively reproduces the evolution of the average degree of mixing along the flow direction, and can be used as a design tool to optimize mixing from viscous fingering in a microfluidic channel.

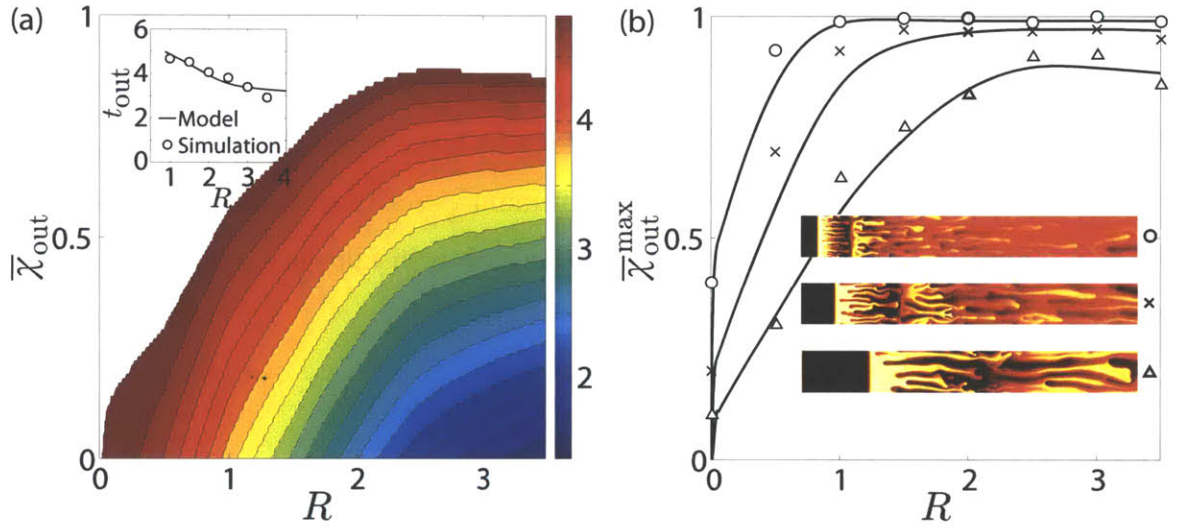

Figure 4-7: (a) Contours of the mixing time, t_{out}, as a function of the *desired* degree of mixing at the outlet, $\overline{\chi}_{\text{out}}$, and the log-viscosity contrast, R, for a domain of dimensionless length $L/l_s = 5$ and $\text{Pe} = 4800$. The white region beyond the outermost contour indicates values of $\overline{\chi}_{\text{out}}$ that cannot be achieved for those flow conditions. The inset shows the comparison of mixing time for $\overline{\chi}_{\text{out}} = 0.5$ between the mixing model and the simulations. (b) Maximum attainable degree of mixing at the outlet, $\overline{\chi}_{\text{out}}^{\text{max}}$, as a function of R for different slug sizes l_s. As l_s decreases, the Péclet number $\text{Pe} = Ul_s/D$ decreases and the dimensionless domain length L/l_s increases, which results in a higher degree of mixing. Shown are three cases: $L/l_s = 5$ (triangles), 10 (crosses), 20 (circles); $\text{Pe} = 4800$, 2400, 1200 in the same order. Solid line is from the mixing–dissipation model, and symbols from the numerical simulations. The insets show snapshots of the concentration field at long times for $R = 2$ and different slug sizes: $L/l_s = 5$ (bottom), 10 (middle), 20 (top).

Chapter 5

Coupled multiphase flow and poromechanics of faulting

5.1 Introduction

Coupling between fluid flow and mechanical deformation in porous media plays a critical role in subsurface hydrology, hydrocarbon recovery, and seismic activity in the Earth's crust. Subsidence due to groundwater withdrawal continues to pose significant challenges in many parts of the world and has been studied for decades [104, 100, 19, 187, 99, 101, 98]. Production and injection of fluids in oil, gas and geothermal fields have also been associated with surface subsidence and earthquakes along pre-existing faults [212, 274, 167, 232, 282, 93, 74, 35]. Earthquakes triggered due to groundwater withdrawal [110], reservoir impoundment [41, 169, 116], and wastewater disposal [145, 261] have been reported, as has been fluctuation in groundwater levels due to earthquakes [217, 266]. Recently, coupled flow and geomechanics has also gained attention due to its role in the long-term geologic storage of carbon dioxide CO_2 in saline aquifers, which is widely regarded as a promising technology to help mitigate climate change by significantly reducing anthropogenic CO_2 emissions into the atmosphere [155, 199, 130, 196, 247]. Injection of CO_2 requires displacement or compression of the ambient groundwater, and an overpressurization of the target aquifer, which could fracture the caprock [25], trigger seismicity and cause shear slip

on pre-existing faults [220, 221, 48, 223, 185, 186, 39, 40], and potentially compromise the caprock by activating faults [283]. A similar set of issues arises in the extraction of oil and natural gas from low-permeability hydrocarbon reservoirs, and in particular oil and gas shales. The extraction of shale-gas has undergone a revolution due to the massive deployment of a technology called hydraulic fracturing, or "fracking" [58]. Concerns have been raised regarding whether fracking may lead to venting of methane from gas shales [126] or to contamination of groundwater by fracking fluids [197, 132]. Therefore, understanding of the potential leakage through faults undergoing slip from injection overpressure has become a cornerstone of the scientific discussion surrounding the viability of CCS as a climate change mitigation technology [283, 141, 284] and the risks associated with the production of shale gas [269, 76, 270].

Despite the growing environmental, industrial and economic importance of coupled flow and geomechanics, many aspects remain poorly understood. One of the key unresolved issues is the ability to describe the mechanical and hydraulic behavior of faults, and the influence of the full stress tensor and change in pressure on fault slip. Injection and production of fluids from a geologic reservoir induce changes in the state of stress, both within and outside of the reservoir, and these can affect the stability of pre-existing faults. The effects of injection and production depend on the initial state of stress, the elastic moduli of the geologic structures, and the fault frictional properties. The effects are not always intuitively obvious, and should be quantified using geomechanical models. This requires the development of a new generation of geomechanical models that include coupling between fluid flow and fault motion.

Currently, geomechanical models typically treat faults as 'failure zones' that are discretized as three-dimensional elements where the rheology is allowed to be different (e.g., plastic with weakening failure) than in the rest of the domain (e.g., elastoplastic with hardening law) [221, 39, 40]. This approach has several limitations, including the inability to model actual slip along a surface of discontinuity, and the dependence of the simulation results on the level of grid refinement. Other models represent faults as surfaces using interface elements e.g. [91], but so far these models are uncoupled to flow and they model fault slip using a penalty method [108]. Such methods require *a*

priori selection of the penalty parameters for the fault, and therefore cannot represent dynamically-evolving fault strength, such as slip-weakening or rate- and state-friction models [71].

The interactions between flow and geomechanics have been modeled computationally using various coupling schemes [68, 134, 138, 175, 182, 233, 234, 256, 259, 258, 148, 149, 147, 150]. In the fully implicit method, one solves the coupled discrete nonlinear system of equations simultaneously, typically using the Newton-Raphson scheme [246, 201, 163, 166, 90]. The fully implicit method guarantees unconditional stability if the mathematical problem is well posed, but the simulation of flow and geomechanics for realistic fields becomes computationally very expensive [233, 256, 138]. Sequential approaches to modeling coupled flow and geomechanics are highly desirable because they offer the flexibility of using separate simulators for each subproblem [86, 227, 182, 224]. The design and analysis of sequential methods with appropriate stability properties for poromechanics and thermomechanics has a long history [277, 10, 11, 9, 233, 175, 134]. Recently, a new sequential method for coupled flow and geomechanics, termed the 'fixed-stress split', has been proposed and analyzed [148, 149, 150]. Stability and convergence analyses have shown that the fixed-stress split inherits the dissipation properties of the continuum problem and is therefore unconditionally stable, both in the linear (poroelastic) and nonlinear (poroelastoplastic) regime. The analysis has shown that the fixed-stress split enjoys excellent convergence properties, even in the quasi-incompressible limit. It has also been shown recently that the stability and convergence properties of the fixed-stress split for single-phase flow carry over to multiphase systems if a proper definition of pore pressure, the 'equivalent pore pressure' [53], is used [150].

In this Chapter, we present a new computational model for coupled flow and geomechanics of faulted reservoirs. We couple a flow simulator with a mechanics simulator using the fixed-stress scheme [149]. We employ a rigorous formulation of nonlinear multiphase geomechanics [52] based on the increment in mass of fluid phases, instead of the more common, but less accurate, scheme based on the change in porosity [233, 182, 256, 259, 258, 224]. Our nonlinear formulation is required to

properly model systems with high compressibility or strong capillarity [52], as can be the case for geologic CO_2 sequestration [220, 221] groundwater extraction from unconfined aquifers [100, 110], and shale gas production [76]. To account for the effect of surface stresses along fluid-fluid interfaces, we use the equivalent pore pressure in the definition of multiphase effective stress [53, 150]. We model faults as surfaces of discontinuity using interface elements [3]. This allows us to model stick-slip behavior on the fault surface for dynamically evolving fault strength.

5.2 Governing equations

5.2.1 Balance laws

We use a classical continuum representation in which the fluids and the solid skeleton are viewed as overlapping continua [18, 54]. The governing equations for coupled flow and geomechanics are obtained from conservation of mass and balance of linear momentum. We assume that the deformations are small, that the geomaterial is isotropic, and that the conditions are isothermal. Let Ω be our domain of interest and $\partial\Omega$ be its closed boundary. Under the quasistatic assumption for earth displacements, the governing equation for linear momentum balance of the solid/fluid system can be expressed as

$$\nabla \cdot \boldsymbol{\sigma} + \rho_b \boldsymbol{g} = \mathbf{0}, \tag{5.1}$$

where $\boldsymbol{\sigma}$ is the Cauchy total stress tensor, $\boldsymbol{g}$ is the gravity vector, and $\rho_b = \phi \sum_{\beta}^{n_{\text{phase}}} \rho_\beta S_\beta + (1-\phi)\rho_s$, is the bulk density, ρ_β and S_β are the density and the saturation of the fluid phase β, ρ_s is the density of the solid phase, ϕ is the true porosity, and n_{phase} is the number of fluid phases. The true porosity is defined as the ratio of the pore volume to the bulk volume in the current (deformed) configuration. Assuming that the fluids are immiscible, the mass-conservation equation for each phase α is

$$\frac{dm_\alpha}{dt} + \nabla \cdot \boldsymbol{w}_\alpha = \rho_\alpha f_\alpha, \tag{5.2}$$

where the accumulation term dm_α/dt describes the time variation of fluid mass relative to the motion of the solid skeleton, $\boldsymbol{w}_\alpha$ is the mass-flux of fluid phase α relative to the solid skeleton, and f_α is the volumetric source term for phase α. Balance equations (5.1) and (5.2) are coupled by virtue of poromechanics. On one hand, changes in the pore fluid pressure lead to changes in effective stress, and induce deformation of the porous material—such as ground subsidence caused by groundwater withdrawal. On the other hand, deformation of the porous medium affects fluid mass content and fluid pressure. The simplest model of this two-way coupling is Biot's macroscopic theory of poroelasticity [24, 103, 52]. In the remainder of this section we provide the mathematical description of poroelasticity, first for single-phase, and then for multiphase fluid systems.

5.2.2 Single-phase poromechanics

For isothermal single-phase flow of a slightly compressible fluid in a poroelastic medium with no stress dependence of permeability, the single-phase fluid mass conservation equation reduces to

$$\frac{dm}{dt} + \nabla \cdot \boldsymbol{w} = \rho_f f, \tag{5.3}$$

where m is the fluid mass content (fluid mass per unit bulk volume of porous medium), ρ_f is the fluid density, $\boldsymbol{w} = \rho_f \boldsymbol{v}$ is the fluid mass flux (fluid mass flow rate per unit area and time), and $\boldsymbol{v}$ is the seepage velocity relative to the deforming skeleton, given by Darcy's law:

$$\boldsymbol{v} = -\frac{\boldsymbol{k}}{\mu}\left(\nabla p - \rho_f \boldsymbol{g}\right), \tag{5.4}$$

where $\boldsymbol{k}$ is the intrinsic permeability tensor, μ is the fluid dynamic viscosity and p is the pore-fluid pressure [18]. It is useful to define the fluid content variation ζ,

$$\zeta := \frac{\delta m}{\rho_{f,0}}, \tag{5.5}$$

where $\delta m = m - m_0$ is the increment in fluid mass content with respect to the initial reference state, and $\rho_{f,0}$ is the reference fluid density.

The self-consistent theory of poroelastic behavior proposed by Biot [24] links the changes in total stress and fluid pressure with changes in strain and fluid content. Following [52], the poroelasticity equations can be written in incremental form as

$$\begin{aligned} \delta\boldsymbol{\sigma} &= \boldsymbol{C}_{dr} : \boldsymbol{\varepsilon} - b\delta p\mathbf{1} \\ \zeta &= b\varepsilon_v + \frac{1}{M}\delta p, \end{aligned} \tag{5.6}$$

where $\boldsymbol{C}_{dr}$ is the rank-4 drained elasticity tensor, $\mathbf{1}$ is the rank-2 identity tensor, $\boldsymbol{\varepsilon}$ is the linearized strain tensor, defined as the symmetric gradient of the displacement vector $\boldsymbol{u}$,

$$\boldsymbol{\varepsilon} := \frac{1}{2}\left(\nabla\boldsymbol{u} + \nabla^T\boldsymbol{u}\right), \tag{5.7}$$

and $\varepsilon_v = \mathrm{tr}(\boldsymbol{\varepsilon})$ is the volumetric strain. It is sometimes useful to express the strain tensor as the sum of its volumetric and deviatoric components:

$$\boldsymbol{\varepsilon} = \frac{1}{3}\varepsilon_v\mathbf{1} + \boldsymbol{e}, \tag{5.8}$$

from which it follows that the volumetric stress $\sigma_v = \mathrm{tr}(\boldsymbol{\sigma})/3$ satisfies:

$$\delta\sigma_v = K_{dr}\varepsilon_v - b\delta p. \tag{5.9}$$

Equation (5.6) implies that the effective stress in single-phase poroelasticity, responsible for skeleton deformation, is defined in incremental form as

$$\delta\boldsymbol{\sigma}' := \delta\boldsymbol{\sigma} + b\delta p\mathbf{1}. \tag{5.10}$$

Note that we use the convention that tensile stress is positive. Biot's theory of poroelasticity has two coupling coefficients: the Biot modulus M and the Biot coefficient b. They are related to rock and fluid properties as [52]

$$\frac{1}{M} = \phi_0 c_f + \frac{b - \phi_0}{K_s}, \quad b = 1 - \frac{K_{dr}}{K_s}, \tag{5.11}$$

where $c_f = 1/K_f$ is the fluid compressibility, K_f is the bulk modulus of the fluid, K_s is the bulk modulus of the solid grain, and K_{dr} is the drained bulk modulus of the porous medium.

To set the stage for the numerical solution strategy of the coupled problem, it is useful to write the fluid mass balance equation (5.3) (the pressure equation) in a way that explicitly recognizes the coupling with mechanical deformation. Equations (5.6) state that the increment in fluid mass content has two components: increment due to expansion of the pore space and increment due to increase in the fluid pressure. Assuming small deformations and applying linearization from the reference state to the current state, we can write Eqs. (5.6) as

$$\boldsymbol{\sigma} - \boldsymbol{\sigma}_0 = \boldsymbol{C}_{dr} : \boldsymbol{\varepsilon} - b\,(p - p_0)\,\mathbf{1}, \tag{5.12}$$

$$\frac{1}{\rho_{f,0}}(m - m_0) = b\varepsilon_v + \frac{1}{M}(p - p_0). \tag{5.13}$$

Substituting Eq. (5.13) into Eq. (5.3), we obtain the fluid mass balance equation in terms of the pressure and the volumetric strain:

$$\frac{1}{M}\frac{\partial p}{\partial t} + b\frac{\partial \varepsilon_v}{\partial t} + \nabla \cdot \boldsymbol{v} = f. \tag{5.14}$$

Linearizing the relation between volumetric total stress and volumetric strain with respect to the reference state,

$$\sigma_v - \sigma_{v,0} = K_{dr}\varepsilon_v - b\,(p - p_0)\,, \tag{5.15}$$

allows us to express the change in porosity as the sum of a volumetric stress component and a fluid pressure component. From $m = \rho_f \phi$ and Eq. (5.13),

$$\frac{\rho_f}{\rho_{f,0}}\phi - \phi_0 = \frac{b}{K_{dr}}\left(\sigma_v - \sigma_{v,0}\right) + \left(\frac{b^2}{K_{dr}} + \frac{1}{M}\right)\left(p - p_0\right). \tag{5.16}$$

Using the effective stress equation, Eq. (5.15), we can rewrite Eq. (5.14) in terms of pressure and volumetric total stress:

$$\left(\frac{b^2}{K_{dr}} + \frac{1}{M}\right)\frac{\partial p}{\partial t} + \frac{b}{K_{dr}}\frac{\partial \sigma_v}{\partial t} + \nabla \cdot \boldsymbol{v} = f. \tag{5.17}$$

Note that Eqs. (5.14) and (5.17) are both exact and, therefore, equivalent. They both recognize the two-way poromechanical coupling, but they lead naturally to different operator splits in a sequential solution method: the fixed-strain split and the fixed-stress split, respectively [149, 147]. Note that, by virtue of the poromechanical coupling, quantities like fluid compressibility and rock compressibility do not appear explicitly in the equation. Instead, the fluid-rock compressibility behavior is determined from the poroelastic coefficients K_{dr}, b, and M [149].

One-way coupled approach

Fluid mass balance Eq. (5.17) is coupled to the mechanics through two terms: modified compressibility, $(b^2/K_{dr} + 1/M)$, and the source term, $(b/K_{dr})\partial\sigma_v/\partial t$. When the fluid compressibility is much higher than the rock compressibility, i.e., $c_f \gg 1/K_{dr} > 1/K_s$, and assuming $c_p = b/(\phi_0 K_{dr}) + 1/K_s$, where c_p is the 'pore compressibility' [233], we obtain

$$(\phi_0 c_f + \phi_0 c_p)\frac{\partial p}{\partial t} + \nabla \cdot \boldsymbol{v} = f, \tag{5.18}$$

where the coupling term corresponding to change in the mean stress is negligible because pressure change is dominated by the high fluid compressibility. Eq. (5.18), which is not coupled to the deformation field, serves as the single-phase fluid mass balance equation in traditional reservoir simulators [13]. We obtain a similar pressure equation under uniaxial strain and constant vertical stress because $\partial\sigma_v/\partial t = 0$, and $(b^2/K_{dr} + 1/M)$ becomes equivalent to the storage coefficient [267].

Pressure fields from solution of Eq. (5.18) can still be used in Eq. (5.1) to ob-

tain displacement fields that evolve in time. This is called the one-way coupled approach [267]. The mechanics problem is coupled to the flow problem, but not vice versa. The one-way coupled approach is computationally less expensive than the fully-coupled or two-way coupled approaches because the flow problem is solved independent of the mechanics problem with no requirement of convergence between the two problems. This leads us to the question: when do we need the fully-coupled (or the two-way coupled) approach, or, when is the one-way coupled approach accurate enough? As illustrated above, accuracy of the one-way coupled approach increases as the compressibility of the fluid increases (e.g. pores occupied by air instead of water), or conditions of uniaxial strain and constant vertical stress prevail. However, the two-way coupled approach is more desirable when small changes in the pore pressure can potentially trigger large-scale changes in the mechanical structure, e.g., faulting and fracturing.

5.2.3 Multiphase poromechanics

In the multiphase or partially saturated fluid system, it is not possible to linearize Eqs. (5.6) around a reference state because [52]:

1. Gases are very compressible,

2. Capillary pressure effects are intrinsically nonlinear, and

3. Phase saturations vary between 0 and 1 and, therefore, a typical problem samples the entire range of nonlinearity.

Therefore, following [52], we use the incremental formulation of poromechanics for multiphase systems, which does not assume physical linearization of total stress from the initial state to the current (deformed) state.

To make progress, we make a modeling assumption that allows us to express the deformation of a multiphase porous material in terms of the increment in applied total stresses and internal fluid pressures. Similar to the single-phase case (Eq. (5.6)), we adopt an effective stress formulation in the multiphase poromechanics [26, 27] because

constitutive modeling of porous materials is usually done in terms of the effective stress. Under this formulation, we split the total stress on the porous material into two parts: one that is responsible for deformation of the material (the effective stress), and another component that is responsible for changes in the fluid pressures,

$$\delta\boldsymbol{\sigma} = \boldsymbol{C}_{dr} : \boldsymbol{\varepsilon} - \sum_{\beta} b_{\beta}\delta p_{\beta}\mathbf{1}, \tag{5.19}$$

where b_β are the Biot coefficients for individual phases such that $\sum_\beta b_\beta = b$, where b is the Biot coefficient of the saturated porous material. It is common to further assume that b_β are proportional to the respective saturations S_β [165, 56, 164].

The effective stress concept allows us to treat a multiphase porous medium as a mechanically equivalent single-phase continuum [146, 193]. The appropriate form of the effective stress equation Eq. (5.19) in a multiphase system is still an active area of research [112, 55, 193, 264, 192, 150]. Here we use the concept of *equivalent pressure* [55] in the effective stress equation (Eq. (5.19)),

$$p_E = \sum_{\beta} S_\beta p_\beta - U, \tag{5.20}$$

where $U = \sum_\beta \int p_\beta dS_\beta$ is the interfacial energy computed from the capillary pressure relations [150]. The equivalent pressure accounts for the interface energy in the free energy of the system, and leads to a thermodynamically consistent and mathematically well-posed description of the multiphase fluid response to the solid deformation [150]. For a system with two phases, the wetting phase w and the non-wetting phase g, the capillary pressure is

$$P_c(S_w) \equiv P_{wg}(S_w) = p_g - p_w, \tag{5.21}$$

and the interfacial energy is $U = \int_{S_w}^{1} P_{wg} dS$. Assuming $b_\beta = bS_\beta$ [165, 56, 164], and using Eq. (5.20) in Eq. (5.19), we obtain the stress-strain relationship for multiphase linear poroelasticity:

$$\delta\boldsymbol{\sigma} = \delta\boldsymbol{\sigma}' - b\delta p_E \mathbf{1}, \quad \delta\boldsymbol{\sigma}' = \boldsymbol{C}_{dr} : \boldsymbol{\varepsilon}. \tag{5.22}$$

Once we have a definition of the effective stress in multiphase systems, we now express the change in the fluid mass in terms of the mechanical deformation and the change in the fluid pressures. In the deformed configuration, the mass of phase α per unit volume of porous medium is

$$m_\alpha = \rho_\alpha S_\alpha \phi (1 + \varepsilon_v). \tag{5.23}$$

Note that, by definition, the sum of all fluid phase saturations satisfies $\sum_\beta^{n_{\text{phase}}} S_\beta \equiv 1$. Extending Eq. (5.13) for multiphase systems [52, 53], we have

$$\left(\frac{dm}{\rho}\right)_\alpha = b_\alpha d\varepsilon_v + \sum_\beta N_{\alpha\beta} dp_\beta, \tag{5.24}$$

where $\boldsymbol{N} = \boldsymbol{M}^{-1}$ is the inverse Biot modulus. In a multiphase system, the Biot modulus is a symmetric positive definite tensor $\boldsymbol{M} = [M_{\alpha\beta}]$, and the Biot coefficient is a vector. To determine the coupling coefficients $N_{\alpha\beta}$ as a function of the primary variables (pressure, saturations, and displacement), and rock and fluid properties, we develop an alternate expression for the differential increment in fluid mass. Using Eq. (5.23),

$$dm_\alpha = d(\rho_\alpha S_\alpha \phi (1 + \varepsilon_v)), \tag{5.25}$$

which can be expanded as

$$\left(\frac{dm}{\rho}\right)_\alpha = \phi \frac{\partial S_\alpha}{\partial P_{\alpha\beta}} dP_{\alpha\beta} + \phi S_\alpha c_\alpha dp_\alpha + \phi S_\alpha d\varepsilon_v + S_\alpha d\phi, \tag{5.26}$$

where $c_\alpha = \frac{1}{\rho_\alpha}\frac{d\rho_\alpha}{dp_\alpha}$ is the compressibility of the fluid phase α, and $\partial S_\alpha / \partial P_{\alpha\beta}$ is the inverse capillary pressure derivative. Above, repeated indices do not imply summation and we have assumed infinitesimal deformations. We can express the increment in porosity, $d\phi$, as a function of the volumetric effective stress, $d\sigma'_v$, to obtain a

closed-form expression of Eq. (5.26). Under infinitesimal deformation theory [52], the volumetric dilation ε_v can be partitioned into the matrix dilation, $\varepsilon_s = \sigma_{sv}/K_s$, and the pore dilation,

$$(1-\phi)\varepsilon_v = (1-\phi)\varepsilon_s + (\phi - \phi_0), \tag{5.27}$$

and the volumetric Cauchy total stress can be partitioned into the volumetric matrix stress, σ_{sv}, and the fluid pressure as

$$\sigma_v = (1-\phi)\sigma_{sv} - \phi p_E. \tag{5.28}$$

Substituting σ_{sv} from Eq. (5.28) into Eq. (5.27) and differentiating, we obtain

$$d\phi = \frac{b-\phi}{K_{dr}}\left(d\sigma_v' + (1-b)dp_E\right), \tag{5.29}$$

where we assumed $1 + \varepsilon_v + (p_E/K_s) \approx 1$. Equation (5.29) implies that an increment in porosity is related to increments in volumetric effective stress and fluid pressures, similar to Eq. (5.16) in the single-phase case. Substituting $d\varepsilon_v$ from Eq. (5.22) and $d\phi$ from Eq. (5.29) into Eq. (5.26) allows us to express the increment in the phase mass as a function of the increments in the total volumetric stress and phase pressures. Equating this to Eq. (5.24) yields the desired expressions for the coupling coefficients $N_{\alpha\beta}$, which for a water-gas system are

$$\begin{aligned} N_{gg} &= -\phi\frac{\partial S_w}{\partial P_{wg}} + \phi S_g c_g + S_g^2 N, \\ N_{gw} = N_{wg} &= \phi\frac{\partial S_w}{\partial P_{wg}} + S_g S_w N, \\ N_{ww} &= -\phi\frac{\partial S_w}{\partial P_{wg}} + \phi S_w c_w + S_w^2 N, \end{aligned} \tag{5.30}$$

where $N = \frac{(b-\phi)(1-b)}{K_{dr}}$, and the subscripts w and g denote water and gas phases, respectively.

Finally, we obtain the multiphase flow equation for phase α in a poroelastic medium by substituting the two constitutive relations, the effective stress equation, Eq. (5.22), and the fluid mass increment equation, Eq. (5.24), in the mass balance equation, Eq. (5.2):

$$\frac{\partial}{\partial t}\left(\rho_\alpha \sum_\beta \left(N_{\alpha\beta} + \frac{b_\alpha b_\beta}{K_{dr}}\right) p_\beta\right) + \frac{1}{K_{dr}}\frac{\partial}{\partial t}\left(\rho_\alpha b_\alpha \sigma_v\right) + \nabla\cdot\boldsymbol{w}_\alpha = \rho_\alpha f_\alpha, \quad \forall\alpha = 1,\ldots,n_{\text{phase}}. \tag{5.31}$$

The role of $\boldsymbol{N}$ and $\boldsymbol{b}$ as the coupling coefficients among different fluid phases and the solid phase is evident from the above equation. The bulk density, ρ_b, in the mechanical equilibrium equation, Eq. (5.1), also acts as a coupling parameter because it is a function of the porosity and the phase saturations. Because we assume that the fluids are immiscible, the mass-flux of phase α is $\boldsymbol{w}_\alpha = \rho_\alpha \boldsymbol{v}_\alpha$, where we adopt the traditional multiphase-flow extension of Darcy's law [188, 18]

$$\boldsymbol{v}_\alpha = -\frac{\boldsymbol{k}k_\alpha^r}{\mu_\alpha}(\nabla p_\alpha - \rho_\alpha \boldsymbol{g}), \tag{5.32}$$

where μ_α and k_α^r are the dynamic viscosity and the relative permeability of phase α in presence of other fluid phases.

5.2.4 Poromechanics of faults

There are two basic approaches to represent faults in a three-dimensional medium: either as a three-dimensional fault zone e.g. [221], or a two-dimensional fault surface [91]. The advantage of representing faults as surfaces of discontinuity is that they can more faithfully describe the localized (discontinuous) displacement at the fault, and one can incorporate models of dynamic frictional strength (like the rate- and state-friction model) capable of reproducing run-away fault slip characteristic of earthquakes. Moreover, introducing discrete fault surfaces does not preclude modeling an adjacent fault zone with appropriate rheology.

A central feature of our work is that we treat faults as surfaces of discontinuity

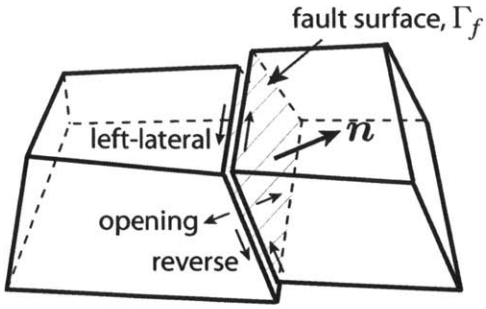

Figure 5-1: Schematic of a 2D fault surface in a 3D domain. Discontinuity in the displacement across the fault is illustrated through slip on the fault. The fault coordinate system is defined in terms of tangential and normal motion on the fault with positive values associated with left-lateral, reverse, and opening motions. $\boldsymbol{n}$ is the fault normal vector on the left side face of the fault.

embedded in the continuum, across which displacement is allowed to be discontinuous to recognize the possibility of fault slip (Fig. 5-1). We use zero-thickness elements, also known as interface elements or cohesive elements in the finite element literature [111, 21, 160, 91], to represent the fault surfaces. Mathematically, the fault surface is treated as an interior boundary between the two adjacent domains. The two sides of the fault surface, which need not be planar, are designated as the '+' side and the '−' side, and the fault normal vector, $\boldsymbol{n}$, points from the negative side to the positive side. Slip on the fault is the displacement of the positive side relative to the negative side,

$$(\boldsymbol{u}_+ - \boldsymbol{u}_-) - \boldsymbol{d} = \boldsymbol{0} \text{ on } \Gamma_f, \tag{5.33}$$

where $\boldsymbol{u}_+$ and $\boldsymbol{u}_-$ are the displacements on the two sides of the fault surface, denoted by Γ_f, and $\boldsymbol{d}$ is the fault slip vector (in the same coordinate system as the displacements). Fault slip is governed by the effective traction on the fault, which is a function of the effective stress tensors on both sides of the fault, the fault normal direction, and the fault constitutive law. We impose the effective traction on the fault by introducing a Lagrange multiplier, $\boldsymbol{l}$, which is a force per unit area required to satisfy the equilibrium equation for a given relative displacement, $\boldsymbol{d}$, across the fault. The magnitude of the effective normal traction on the fault is $\sigma'_n = \boldsymbol{l} \cdot \boldsymbol{n}$. A positive value of σ'_n indicates that a tensile effective stress is transmitted across the

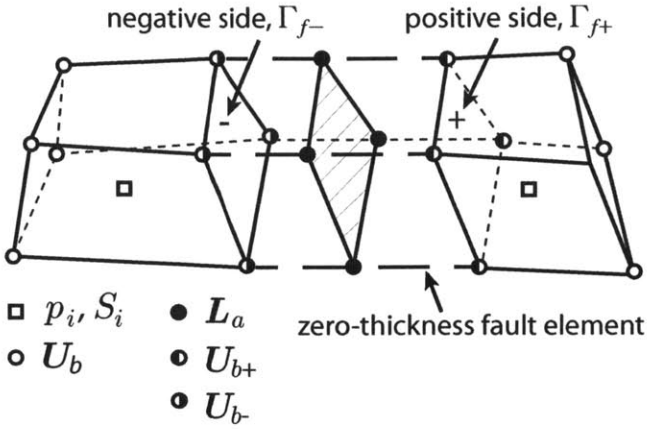

Figure 5-2: Exploded view of our computational representation of a fault, illustrating different node types, locations of different variables, and the zero-thickness fault elements. Fluid pressures and saturations are located at the element centers as they are discretized using the finite volume method. Displacements and Lagrange multipliers at the fault are discretized using the nodal-based finite element method. There are two types of nodes in the domain: the regular displacement nodes and the fault nodes. Regular nodes carry displacements $\boldsymbol{U}_b$. Fault nodes carry three types of variables at the same location: the displacement on the positive side of the fault, $\boldsymbol{U}_{b_+}$, the displacement on the negative side of the fault, $\boldsymbol{U}_{b_-}$, and the Lagrange multiplier, $\boldsymbol{L}_a$.

fault surface. The shear traction vector is, by definition, tangent to the fault surface and its magnitude is

$$\tau = |\boldsymbol{l} - \sigma'_n \boldsymbol{n}|. \tag{5.34}$$

Models of fault strength

Shear tractions on the fault are limited by fault friction, or fault strength. A fault constitutive model is used to compute the frictional stress τ_f on the fault as

$$\tau_f = \begin{cases} \tau_c - \mu_f \sigma'_n, & \sigma'_n < 0, \\ \tau_c, & \sigma'_n \geq 0, \end{cases} \tag{5.35}$$

where τ_c is the cohesive strength of the fault, and μ_f is the coefficient of friction, which must be modeled as a function of displacement evolution on the fault. Commonly used fault friction models are

1. Static friction model, where μ_f is a constant.

2. Slip-Weakening model, where μ_f is a function of the slip magnitude $|\boldsymbol{d}|$ and drops linearly from its static value, μ_s, to its dynamic value, μ_d, over a critical slip distance d_c,

$$\mu_f = \begin{cases} \mu_s - (\mu_s - \mu_d)\frac{|\boldsymbol{d}|}{d_c}, & |\boldsymbol{d}| \leq d_c, \\ \mu_d, & |\boldsymbol{d}| > d_c. \end{cases} \tag{5.36}$$

3. Rate- and State-dependent friction model [71, 70, 218, 230, 179],

$$\begin{aligned} \mu_f &= \mu_0 + A \ln\left(\frac{V}{V_0}\right) + B \ln\left(\frac{V_0 \theta}{d_c}\right), \\ \frac{d\theta}{dt} &= 1 - \frac{\theta V}{d_c}, \end{aligned} \tag{5.37}$$

   where $V = |d\boldsymbol{d}/dt|$ is the slip rate magnitude, μ_0 is the steady-state friction coefficient at the reference slip rate V_0, A and B are empirical dimensionless constants, and θ is the macroscopic variable characterizing state of the surface.

In the Rate- and State-dependent friction model, which is based on laboratory experiments of frictional sliding on rock surfaces and fault gouges, evolution of the coefficient of friction is determined from the combined effect of the evolution of the state variable, θ, and the slip rate or velocity, V. Here, θ may be understood as the frictional contact time [71], or the average maturity of contact asperities between the sliding surfaces [215]. Evolution of θ is assumed to be independent of changes in the normal traction, σ_n', that can accompany the fault slip due to changes in the fluid pressure. The model accounts for the decrease in friction as the slip increases (slip-weakening), and increase in friction (healing) as the time of contact or slip velocity increases (Fig. 5-3). The two effects act together such that $A > B$ leads to strengthening of the fault, stable sliding and creeping motion, and $A < B$ leads to weakening of the fault, frictional instability, and accelerating slip. In this way, the model is capable of capturing repetitive stick-slip behavior of faults and the resulting seismic cycle [70, 230].

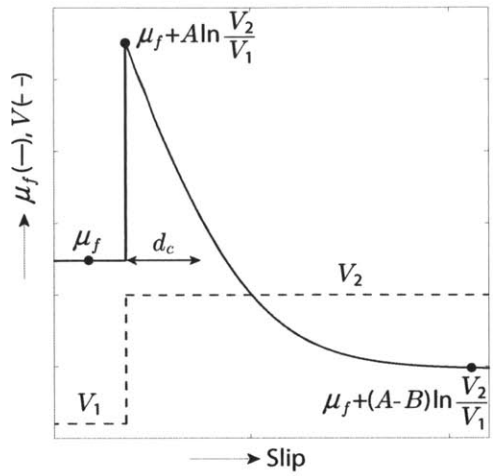

Figure 5-3: Rate- and State-dependent friction model. Coefficient of friction on the fault, μ_f, evolves with the slip rate or velocity, V, and the state variable, θ, as per Eq. (5.37). For a sudden increase in the slip velocity from V_1 to V_2, the coefficient of friction first increases sharply due to a sudden increase in resistance from contact asperities, and then declines slowly due to slip-weakening. The final steady-state value of the coefficient of friction can be lower than the initial steady-state value if $A - B < 0$, as shown above.

We use the Mohr-Coulomb theory to define the failure criterion for the fault [133]. When the shear traction on the fault is below the friction stress, $\tau \leq \tau_f$, the fault does not slip. When the shear traction is above the friction stress, $\tau > \tau_f$, the contact problem is solved to determine the Lagrange multipliers and slip on the fault. The Lagrange multipliers attain values that are compatible with the frictional stress.

Fault pressure in the failure criterion

Traditionally, in the Andersonian faulting theory [8], fault slip is modeled in a 'dry environment', that is, in the absence of fluids. In some cases, presence of fluid was recognized through the effective stress concept, however, dynamics of flow was not considered for reasons of conceptual and computational simplicity, as well as for the belief that fluid flow plays a secondary role in the release of tectonic stresses [127]. The effect of pore pressure was accounted for by modifying the coefficient of fault friction, μ_f [20]. In the case of mature faults, the fault permeability to flow can be very low due to comminution of grains [37, 17], and therefore it may appear that flow has a secondary role in determining the stability of these faults. However, precisely because

of low permeability in fault zones, the fluid pressure can be highly heterogeneous in space, with different values across the fault. A difference in fluid pressure across the fault leads to a pressure jump $[\![p]\!]_{\Gamma_f} = p_+ - p_-$, where p_+ and p_- are the equivalent multiphase pressures (Eq. (5.20)) on the 'positive' and the 'negative' side of the fault. One of the key features of the 2D representation of faults is the ability to reproduce a finite jump in the pressure, $[\![p]\!]_{\Gamma_f}$, across the fault. This pressure jump leads to discontinuity in the effective stress across the fault, such that, the total stress is continuous,

$$\boldsymbol{\sigma}'_- \cdot \boldsymbol{n} - bp_-\boldsymbol{n} = \boldsymbol{\sigma}'_+ \cdot \boldsymbol{n} - bp_+\boldsymbol{n}, \tag{5.38}$$

a requirement for momentum balance on the fault. Then the question arises, how can this pressure jump across a fault be incorporated in the formulation? This is important because it dictates stability of the fault.

Fault stability can be assessed by evaluating the failure criterion on both sides of the fault separately. The side of the fault where the criterion is met first, determines the fault stability. Equivalently, this can be achieved by defining a *fault pressure* that is a function of the pressures on the two sides, p_+ and p_-. Introducing the fault pressure allows us to uniquely define the normal traction on fault σ'_n, which determines the fault friction τ_f (Eq. (5.35)). Since the failure criterion, $\tau > \tau_f$, is first reached with the larger pressure, we define the fault pressure, p_f, as

$$p_f = \max(p_-, p_+). \tag{5.39}$$

5.2.5 Boundary and initial conditions

The mathematical model requires that initial and boundary conditions be defined for both the fluid flow and mechanical problems. We consider one pressure, p_α, and $n_{\text{phase}} - 1$ saturations, $\{S_\beta, \forall \beta \neq \alpha\}$, as the primary variables of the multiphase flow problem, where α is one of the fluid phases. Pressures of the remaining $n_{\text{phase}} - 1$ phases can be uniquely determined from the $n_{\text{phase}} - 1$ capillary pressure relations (Eq. (5.21)). Saturation S_α is determined from the constraint that the sum of all

saturations is identically equal to 1.

Geologic reservoirs are located at depth, while the effect of coupled flow and deformation, such as subsidence and earthquakes, are observed at the ground surface. The weight of the overburden rock plays an important role in determining the ground subsidence even when it is not part of the flow domain. The flow domain could also be laterally confined due to sedimentary or stratigraphic features such as pinch-outs, sealing faults, or other types of hydraulic barriers. As a result, the boundaries of the flow domain and the mechanical domain may not coincide. The mechanical domain is usually extended such that it encapsulates the flow domain [233], which also reduces spurious boundary effects

Since the flow equation, Eq. (5.31), is a statement of balance of fluid fluxes with fluid accumulation, the most natural boundary condition for the flow problem is a flux boundary condition. It is a common practice to define the flow domain such that it can be modeled as a closed system, in which case the normal component of the fluid flux of each phase α across the boundary is zero,

$$\boldsymbol{v}_\alpha \cdot \boldsymbol{n} = 0 \text{ on } \Gamma_v, \tag{5.40}$$

where $\boldsymbol{n}$ is the outward unit normal to the boundary Γ_v. Non-zero boundary fluxes can similarly be prescribed. When the flow domain is in communication with an external system with known pressure (such as an aquifer of known capacity), it is possible to prescribe a mixed boundary condition, where a linear combination of pressure and normal pressure gradient across the boundary, for a given phase, is expressed in terms of the pressure outside the boundary

$$C_1 \frac{\partial p_\alpha}{\partial n} + p_\alpha = \overline{p} \text{ on } \Gamma_p, \tag{5.41}$$

where C_1 is a constant related to the boundary transmissibility and $\overline{p}$ is the known external pressure [42, 92]. The parts of the boundary with prescribed external pressure and flux must be non-overlapping and cover the entire boundary, i.e., $\Gamma_p \cap \Gamma_v = \emptyset$, $\Gamma_p \cup \Gamma_v = \partial\Omega$.

For the mechanical problem, displacements are the primary variables. The boundary condition can be prescribed either in terms of the displacements or the tractions or a suitable combination of both along the boundary,

$$\boldsymbol{u} = \overline{\boldsymbol{u}} \text{ on } \Gamma_u, \qquad \boldsymbol{\sigma} \cdot \boldsymbol{n} = \overline{\boldsymbol{t}} \text{ on } \Gamma_\sigma, \tag{5.42}$$

where $\overline{\boldsymbol{u}}$ is a prescribed displacement, and $\overline{\boldsymbol{t}}$ is a prescribed traction. Γ_u and Γ_σ boundaries may overlap because a node can have a prescribed displacement in one direction and prescribed tractions in other directions. However, they must satisfy $\Gamma_u \cup \Gamma_\sigma = \partial\Omega$.

Initialization of a coupled multiphase poromechanics problem requires careful attention. The common practice is to initialize the problem under the assumption of flow and mechanical equilibrium. Pressures and saturations in the multiphase flow problem can be initialized using the concept of Vertical Equilibrium [61], which assumes that the fluids are distributed vertically satisfying capillary–gravity equilibrium. Since initialization is performed at a time before any well starts to flow, this is usually a good assumption. Initial pressures are calculated based on hydrostatics, using prescribed fluid contacts and a datum pressure in the flow domain. Initial saturations are calculated from the initial capillary pressures, and they also honor the fluid contacts. Since hydrostatic pressures depend on fluid densities, which in turn depend on fluid compressibilities, which further depend on pressure, initialization is done iteratively–two to three iterations are sufficient for most problems.

We initialize the mechanical problem with zero displacement field. Therefore, initial stresses are prescribed such that they balance body forces and boundary tractions.

5.3 Numerical formulation

In this section we discuss the numerical formulation and discretization of the coupled multiphase flow and geomechanics problem. We first present the space discretization,

followed by the time discretization and, finally, the fully discrete system of algebraic equations.

5.3.1 Space discretization

We use the finite volume method for discretization of the flow problem [13], and the nodal-based finite element method for discretization of the mechanics problem [129, 278]. We use a single, unstructured computational grid for both the flow and the mechanics problems. The pressures and saturations degrees of freedom are located at the element center, and the displacement vector degrees of freedom are located at the element nodes (Fig. 5-1). This space discretization is locally mass conservative at the element level, yields a continuous displacement field, and enjoys excellent stability properties [138, 207, 208, 147].

Elements with nodes on the fault surface deserve special consideration. Each node on the fault is triplicated to create a 'b_+' node on the positive side, a 'b_-' node on the negative side, and a Lagrange node 'a' in the middle. These nodes store the positive side displacement $\boldsymbol{u}_+$, the negative side displacement $\boldsymbol{u}_-$, and the Lagrange multiplier $\boldsymbol{l}$, respectively. All three nodes are physically collocated in the initial grid, so elements representing the fault are *zero-thickness elements*. Slip on the fault is related to the positive and the negative side displacement fields through Eq. (5.33). The Lagrange multipliers are the fault tractions required to satisfy both the equilibrium equation, Eq. (5.43), and the friction constraint $\tau \leq \tau_f$ with τ_f from Eq. (5.35). We define a fault coordinate system to relate the quantities commonly used in describing the fault motion (reverse or normal slip, and left or right lateral slip; see Fig. 5-1) to the global displacements. In three dimensions, the fault coordinate system is defined with along-strike (lateral), along-dip (reverse or normal), and normal-to-fault (opening) directions (Fig. 5-2). In the fault coordinate system, the fault normal vector in 3D is $\boldsymbol{n}_f = [0, 0, 1]^T$, where superscript T indicates transpose.

Mechanics problem

Using standard arguments from functional analysis [34] that is, multiplying by the test functions (which act as weighting functions in the integral form of the differential equation, and satisfy essential boundary conditions), integrating over the domain, applying the divergence theorem, inserting the essential and natural boundary conditions, and exploiting symmetry of the stress tensor, we arrive at the weak form of the governing equations for the mechanics problem: Find $(\boldsymbol{u}, \boldsymbol{l})$ belonging to appropriate functional spaces satisfying the essential boundary conditions ($\boldsymbol{u} = \overline{\boldsymbol{u}}$ on Γ_u) such that

$$\int_{\Omega} \nabla^s \boldsymbol{\eta} : (\boldsymbol{\sigma}' - bp_E \mathbf{1}) d\Omega + \int_{\Gamma_{f_+}} \boldsymbol{\eta} \cdot (\boldsymbol{l} - bp_f \boldsymbol{n}) d\Gamma - \int_{\Gamma_{f_-}} \boldsymbol{\eta} \cdot (\boldsymbol{l} - bp_f \boldsymbol{n}) d\Gamma - \int_{\Omega} \boldsymbol{\eta} \cdot \rho_b \boldsymbol{g} d\Omega - \int_{\Gamma_\sigma} \boldsymbol{\eta} \cdot \bar{\boldsymbol{t}} d\Gamma = \mathbf{0}, \tag{5.43}$$

$$\int_{\Gamma_f} \boldsymbol{\eta} \cdot (\boldsymbol{u}_+ - \boldsymbol{u}_- - \boldsymbol{d}) d\Gamma = \mathbf{0}, \tag{5.44}$$

for all test functions $\boldsymbol{\eta}$ ($n_{\text{dim}} \times 1$ vector) belonging to the appropriate functional space satisfying $\boldsymbol{\eta} = \mathbf{0}$ on Γ_u. Here, we used the multiphase effective stress equation, Eq. (5.22). p_E is the equivalent pressure (Eq. (5.20)), p_f is the fault pressure (Eq. (5.39)), and ρ_b is the bulk density, all of which depend on the phase pressures and saturations, and, therefore, on the solution of the flow problem. For linear elastic and isotropic material, the elasticity tensor $\boldsymbol{C}_{dr}$ is given in terms of the Young modulus, E, and the Poisson ratio, ν.

Let the domain be partitioned into non-overlapping elements (grid blocks), $\Omega = \cup_{j=1}^{n_{\text{elem}}} \Omega_j$ where n_{elem} is the number of volumetric elements. A fault is treated as an interior boundary with its domain, Ω_f, partitioned into non-overlapping fault elements, $\Omega_f = \cup_{j=1}^{n_{f,\text{elem}}} \Omega_{f,j}$, where the subscript f indicates variables associated with a fault. The displacement, the Lagrange multiplier, and the slip fields are approximated

as follows:

$$\boldsymbol{u} \approx \boldsymbol{u}_h = \sum_{b=1}^{n_{\text{node}}} \eta_b \boldsymbol{U}_b = \boldsymbol{\eta}_b \cdot \boldsymbol{U}_b, \tag{5.45}$$

$$\boldsymbol{l} \approx \boldsymbol{l}_h = \sum_{a=1}^{n_{f,\text{node}}} \eta_a \boldsymbol{L}_a = \boldsymbol{\eta}_a \cdot \boldsymbol{L}_a, \tag{5.46}$$

$$\boldsymbol{d} \approx \boldsymbol{d}_h = \sum_{a=1}^{n_{f,\text{node}}} \eta_a \boldsymbol{D}_a = \boldsymbol{\eta}_a \cdot \boldsymbol{D}_a, \tag{5.47}$$

where subscript h indicates the finite element approximation, n_{node} is the number of displacement nodes, and $n_{f,\text{node}}$ is the number of Lagrange nodes. Under the summation sign, $\boldsymbol{U}_b$ are the displacement vectors at the element nodes (including the displacements $\boldsymbol{U}_{b_+}$ and $\boldsymbol{U}_{b_-}$ at the fault nodes), and $\boldsymbol{L}_a$ and $\boldsymbol{D}_a$ are the Lagrange multiplier vectors and the slip vectors at the Lagrange nodes of the fault. $\boldsymbol{L}_a$ and $\boldsymbol{D}_a$ are in the fault coordinate system (Fig. 5-1). Dot product in the rightmost expressions denotes a matrix-vector product. $\boldsymbol{U}_b$ in the rightmost expression is a global vector over all the nodes, hence, of size $n_{\text{dim}} n_{\text{node}} \times 1$. Similarly, $\boldsymbol{L}_a$ and $\boldsymbol{D}_a$ on the right hand side are global vectors over all the Lagrange nodes, hence, of size $n_{\text{dim}} n_{f,\text{node}} \times 1$. The interpolation functions, η_b and η_a, are the usual C^0–continuous isoparametric functions, such that they take a value of 1 at the respective nodes, and 0 at all other nodes. $\boldsymbol{\eta}_b$ is a $n_{\text{dim}} \times n_{\text{dim}} n_{\text{node}}$ matrix and in 2D it takes the form

$$\boldsymbol{\eta}_b = \begin{bmatrix} \eta_1 & 0 & \eta_2 & 0 & \dots & \eta_{n_{\text{node}}} & 0 \\ 0 & \eta_1 & 0 & \eta_2 & \dots & 0 & \eta_{n_{\text{node}}} \end{bmatrix}. \tag{5.48}$$

Similarly, $\boldsymbol{\eta}_a$ is a $n_{\text{dim}} \times n_{\text{dim}} n_{f,\text{node}}$ matrix. After substitution of the finite element approximations into the weak form of the problem [Eqs. (5.43)–(5.44)], we obtain the

discrete equations in residual form:

$$\begin{aligned}\mathbf{0} &= \int_{\Omega} \boldsymbol{B}_b : (\boldsymbol{\sigma}'_h - bp_{E,h}\mathbf{1})d\Omega \\ &+ \int_{\Gamma_{f+}} \boldsymbol{\eta}_{b_+} \cdot \boldsymbol{\eta}_a \cdot (\boldsymbol{L}_a - bp_{f,h}\boldsymbol{n}_f)d\Gamma - \int_{\Gamma_{f-}} \boldsymbol{\eta}_{b_-} \cdot \boldsymbol{\eta}_a \cdot (\boldsymbol{L}_a - bp_{f,h}\boldsymbol{n}_f)d\Gamma \\ &- \int_{\Omega} \boldsymbol{\eta}_b \cdot \rho_{b,h}\boldsymbol{g}d\Omega - \int_{\Gamma_\sigma} \boldsymbol{\eta}_b \cdot \bar{\mathbf{t}}d\Gamma, \qquad (5.49)\end{aligned}$$

$$\mathbf{0} = \int_{\Gamma_f} \boldsymbol{\eta}_a \cdot (\boldsymbol{\eta}_{b_+} \cdot \boldsymbol{U}_{b_+} - \boldsymbol{\eta}_{b_-} \cdot \boldsymbol{U}_{b_-} - \boldsymbol{\eta}_a \cdot \boldsymbol{D}_a)d\Gamma, \qquad (5.50)$$

where $\boldsymbol{B}_b = \nabla^s \boldsymbol{\eta}_b$ is the linearized strain tensor, which, in 2D, takes the form

$$\boldsymbol{B}_b = \begin{bmatrix} \partial_x\eta_1 & 0 & \partial_x\eta_2 & 0 & \dots \\ 0 & \partial_y\eta_1 & 0 & \partial_y\eta_2 & \dots \\ \partial_y\eta_1 & \partial_x\eta_1 & \partial_y\eta_2 & \partial_x\eta_2 & \dots \end{bmatrix}, \qquad (5.51)$$

corresponding to the compact engineering notation for stress and strain inside an element as $\boldsymbol{\sigma}'_h = [\sigma'_{h,xx}, \sigma'_{h,yy}, \sigma'_{h,xy}]^T$ and $\boldsymbol{\varepsilon}_h = [\varepsilon_{h,xx}, \varepsilon_{h,yy}, 2\varepsilon_{h,xy}]^T$, respectively [129]. Identity tensor in the compact notation is $\mathbf{1} = [1, 1, 0]^T$. $\boldsymbol{\eta}_{b_+}$ and $\boldsymbol{\eta}_{b_-}$ are $n_{\text{dim}} \times n_{\text{dim}} n_{f,\text{node}}$ matrices. Effective stress is computed as $\delta\boldsymbol{\sigma}'_h = \boldsymbol{D}\boldsymbol{\varepsilon}_h = \boldsymbol{D}\boldsymbol{B}_b\boldsymbol{U}_b$, where in 2D

$$\boldsymbol{D} = \frac{E(1-\nu)}{(1+\nu)(1-2\nu)} \begin{bmatrix} 1 & \frac{\nu}{1-\nu} & 0 \\ \frac{\nu}{1-\nu} & 1 & 0 \\ 0 & 0 & \frac{1-2\nu}{2(1-\nu)} \end{bmatrix}, \qquad (5.52)$$

is the elasticity matrix, E is the Young modulus, and ν is the Poisson ratio. With these substitutions, the integrand in the first term in Eq. (5.49) becomes $\boldsymbol{B}_b^T\boldsymbol{D}\boldsymbol{B}_b\boldsymbol{U}_b - bp_{E,h}\boldsymbol{B}_b^T\mathbf{1}$. Note that in the second and the third term of Eq. (5.49), it is assumed that the fault pressure is collocated with the Lagrange multiplier node and, therefore, can be interpolated identically. Eq. (5.49) results in $n_{\text{dim}}n_{\text{node}}$ equations, and Eq. (5.50) results in $n_{\text{dim}}n_{f,\text{node}}$ equations.

We solve Eq. (5.49) subject to the slip constraint

$$\delta \boldsymbol{D}_a = \begin{cases} \mathbf{0}, & \tau_a \leq \tau_{f,a}, \\ \boldsymbol{f}(\tau_a, \tau_{f,a}, \boldsymbol{L}_a), & \tau_a > \tau_{f,a}, \end{cases} \tag{5.53}$$

where τ and τ_f are from Eq. (5.34) and Eq. (5.35), respectively. $\boldsymbol{f}(\cdot)$ is a vector function of fault tractions and fault friction that determines slip on the fault, and it is determined by solving the contact problem.

Multiphase flow problem

The flow problem is discretized using the finite volume method on the same grid defined for the mechanical domain, $\Omega = \cup_{i=1}^{n_{\text{elem}}} \Omega_i$. For simplicity, let us consider two fluid phases, water and gas. Note that in each element, $S_w + S_g \equiv 1$. We integrate the fluid phase mass conservation equation, Eq. (5.31), for each phase over each element i. For the water phase, this yields

$$\begin{aligned} &\frac{\partial}{\partial t} \int_{\Omega_i} \rho_w \left(\left(N_{ww} + N_{wg} + \frac{b b_w}{K_{dr}} \right) p_g - \left(N_{ww} + \frac{b_w^2}{K_{dr}} \right) P_{wg} \right) d\Omega \\ &+ \frac{1}{K_{dr}} \frac{\partial}{\partial t} \int_{\Omega_i} \rho_w b_w \sigma_v d\Omega - \int_{\partial \Omega_i} \boldsymbol{w}_w \cdot \boldsymbol{n}_i d\Gamma = \int_{\Omega_i} \rho_w f_w d\Omega, \end{aligned} \tag{5.54}$$

where we used the capillary pressure relation, $P_{wg} = p_g - p_w$, to eliminate the water phase pressure, the Biot coefficient relation, $b_g + b_w = b$, and integration by parts for the mass-flux term to express it as a surface integral. $\boldsymbol{n}_i$ is the outward normal to the boundary of the element i. Similarly, we have a mass balance equation for the gas phase:

$$\begin{aligned} &\frac{\partial}{\partial t} \int_{\Omega_i} \rho_g \left(\left(N_{wg} + N_{gg} + \frac{b b_g}{K_{dr}} \right) p_g - \left(N_{wg} + \frac{b_g b_w}{K_{dr}} \right) P_{wg} \right) d\Omega \\ &+ \frac{1}{K_{dr}} \frac{\partial}{\partial t} \int_{\Omega_i} \rho_g b_g \sigma_v d\Omega - \int_{\partial \Omega_i} \boldsymbol{w}_g \cdot \boldsymbol{n}_i d\Gamma = \int_{\Omega_i} \rho_g f_g d\Omega. \end{aligned} \tag{5.55}$$

We approximate both the pressure and the saturation fields with a piecewise constant interpolation function, φ, such that φ_i takes a constant value of 1 over element i and

0 at all other elements. Phase pressures and saturations are approximated as

$$p_\alpha \approx p_{\alpha,h} = \sum_{i=1}^{n_{\text{elem}}} \varphi_i p_{\alpha,i}, \tag{5.56}$$

$$S_\alpha \approx S_{\alpha,h} = \sum_{i=1}^{n_{\text{elem}}} \varphi_i S_{\alpha,i}, \tag{5.57}$$

where the discrete pressures, $p_{\alpha,i}$, and phase saturations, $S_{\alpha,i}$, are located at the center of the element i (Fig. 5-2).

We can further express the mass flux term as a sum of integral fluxes between element i and its adjacent elements j:

$$\int_{\partial\Omega_i} \boldsymbol{w}_w \cdot \boldsymbol{n}_i d\Gamma = \sum_{j=1}^{n_{\text{face},i}} \int_{\Gamma_{ij}} \boldsymbol{w}_w \cdot \boldsymbol{n}_{ij} d\Gamma = \sum_{j=1}^{n_{\text{face},i}} W_{w,ij}, \tag{5.58}$$

where $n_{\text{face},i}$ is the number of faces of element i, and $\boldsymbol{n}_{ij}$ is the outward normal at the face Γ_{ij}. The inter-element flux of water, $W_{w,ij}$, can be evaluated from Darcy's law (Eq. (5.32)) as a function of the rock and fluid properties, pressures, and saturations of the element i and its adjacent elements j, using a two-point or multipoint flux approximation [162, 114, 5]. After substitution, the semi-discrete water phase mass balance equation is

$$\begin{aligned} 0 = {} & \frac{\partial}{\partial t}\left[V_{b,i}\rho_{w,i}\left(\left(N_{ww} + N_{wg} + \frac{bb_w}{K_{dr}}\right)_i p_{g,i} - \left(N_{ww} + \frac{b_w^2}{K_{dr}}\right)_i P_{wg,i}\right)\right] \\ & + \frac{\partial}{\partial t}\left(\rho_{w,i}\left(\frac{b_w\sigma_v}{K_{dr}}\right)_i V_{b,i}\right) - \sum_{j=1}^{n_{\text{face},i}} W_{w,ij} - \rho_{w,i} f_{w,i} V_{b,i}, \quad \forall i = 1, \ldots, n_{\text{elem}}, \end{aligned} \tag{5.59}$$

where subscript i refers to the value at element i. Similarly, we could write the semi-discrete equation for the gas phase:

$$\begin{aligned} 0 = {} & \frac{\partial}{\partial t}\left[V_{b,i}\rho_{g,i}\left(\left(N_{gw} + N_{gg} + \frac{bb_g}{K_{dr}}\right)_i p_{g,i} - \left(N_{gw} + \frac{b_g b_w}{K_{dr}}\right)_i P_{wg,i}\right)\right] \\ & + \frac{\partial}{\partial t}\left(\rho_{g,i}\left(\frac{b_g\sigma_v}{K_{dr}}\right)_i V_{b,i}\right) - \sum_{j=1}^{n_{\text{face},i}} W_{g,ij} - \rho_{g,i} f_{g,i} V_{b,i}, \quad \forall i = 1, \ldots, n_{\text{elem}}, \end{aligned} \tag{5.60}$$

5.3.2 Time discretization

In quasi-static poromechanics, the time derivative appears only in the accumulation term of the fluid mass balance equation (first two terms in Eq. (5.59)) which we discretize using the fully implicit Backward Euler scheme,

$$\frac{\partial m_\alpha}{\partial t} \approx \delta_t m_\alpha = \frac{m_\alpha^{n+1} - m_\alpha^n}{\delta t}, \tag{5.61}$$

where superscript n denotes the time level, and δt is the time step.

5.3.3 Fully discrete coupled system

Introducing the time discretization in the semi-discrete finite element Eqs. (5.49)–(5.50), we arrive at the following coupled system of algebraic equations

$$\begin{aligned}
\boldsymbol{R}_u = & \int_\Omega \boldsymbol{B}_b : (\boldsymbol{\sigma}_h^{n+1} - bp_{E,h}^{n+1}\mathbf{1}) d\Omega \\
& + \int_{\Gamma_{f+}} \boldsymbol{\eta}_{b_+} \cdot \boldsymbol{\eta}_a \cdot (\boldsymbol{L}_a^{n+1} - bp_{f,h}^{n+1}\boldsymbol{n}_f) d\Gamma - \int_{\Gamma_{f-}} \boldsymbol{\eta}_{b_-} \cdot \boldsymbol{\eta}_a \cdot (\boldsymbol{L}_a^{n+1} - bp_{f,h}^{n+1}\boldsymbol{n}_f) d\Gamma \\
& - \int_\Omega \boldsymbol{\eta}_b \cdot \rho_{b,h}^{n+1} \boldsymbol{g} d\Omega - \int_{\Gamma_\sigma} \boldsymbol{\eta}_b \cdot \bar{\boldsymbol{t}} d\Gamma,
\end{aligned} \tag{5.62}$$

$$\boldsymbol{R}_l = \int_{\Gamma_f} \boldsymbol{\eta}_a \cdot (\boldsymbol{\eta}_{b_+} \cdot \boldsymbol{U}_{b_+}^{n+1} - \boldsymbol{\eta}_{b_-} \cdot \boldsymbol{U}_{b_-}^{n+1} - \boldsymbol{\eta}_a \cdot \boldsymbol{D}_a^{n+1}) d\Gamma. \tag{5.63}$$

to be solved at every time step for the displacements $\boldsymbol{U}_b^{n+1}$ at the regular nodes, and the Lagrange multipliers $\boldsymbol{L}_a^{n+1}$ at the fault nodes such that the above residuals are zero. In vector form, the system of $n_{\text{dim}}(n_{\text{node}} + n_{f,\text{node}})$ algebraic equations of the mechanical problem can be expressed as follows:

$$\begin{bmatrix} \boldsymbol{R}_u \\ \boldsymbol{R}_l \end{bmatrix} = \begin{bmatrix} \mathbf{0} \\ \mathbf{0} \end{bmatrix}, \tag{5.64}$$

which needs to be solved subject to the constraint in Eq. (5.53) at every time step.

For the water–gas multiphase flow problem, we have

$$R_{w,i} = \delta_t \left[V_b \rho_w \left(\left(N_{ww} + N_{wg} + \frac{b b_w}{K_{dr}} \right) p_g - \left(N_{ww} + \frac{b_w^2}{K_{dr}} \right) P_{wg} \right) \right]_i + \delta_t \left[\rho_w \frac{b_w}{K_{dr}} \sigma_v V_b \right]_i - \sum_{j=1}^{n_{\text{face},i}} W_{w,ij} - \left[\rho_w f_w V_b \right]_i , \tag{5.65}$$

$$R_{g,i} = \delta_t \left[V_b \rho_g \left(\left(N_{gw} + N_{gg} + \frac{b b_g}{K_{dr}} \right) p_g - \left(N_{gw} + \frac{b_g b_w}{K_{dr}} \right) P_{wg} \right) \right]_i + \delta_t \left[\rho_g \frac{b_g}{K_{dr}} \sigma_v V_b \right]_i - \sum_{j=1}^{n_{\text{face},i}} W_{g,ij} - \left[\rho_g f_g V_b \right]_i \tag{5.66}$$

which must be solved at every time step for the element gas phase pressure $p_{g,i}^{n+1}$, and the element water phase saturation $S_{w,i}^{n+1}$ such that the above residuals are zero. The water phase pressure is determined with the help of the capillary pressure relation (Eq. (5.21)), and the gas saturation is determined from the constraint $S_g + S_w \equiv 1$. The system of $n_{\text{phase}} \times n_{\text{elem}}$ algebraic equations of the multiphase flow problem can be expressed as follows:

$$\begin{bmatrix} \boldsymbol{R}_w \\ \boldsymbol{R}_g \end{bmatrix} = \begin{bmatrix} \mathbf{0} \\ \mathbf{0} \end{bmatrix} . \tag{5.67}$$

The mechanics problem is coupled to the flow problem through the inverse Biot modulus $\boldsymbol{N}$, the drained bulk modulus K_{dr}, the Biot coefficient $\boldsymbol{b}$, and the bulk density ρ_b. Further, $\boldsymbol{N}$, $\boldsymbol{b}$, and ρ_b are themselves functions of fluid pressures, saturations and solid displacements.

5.4 Solution strategy

In this section, we discuss our scheme for solving the coupled system, Eqs. (5.64)–(5.67). We use a sequential-implicit solution scheme [202, 277, 10, 9, 138, 147] to solve the coupled multiphase and geomechanics problem. In this scheme, the two sub-problems of multiphase flow and mechanics are solved in sequence such that each sub-problem is solved using implicit time discretization. An outer iteration is performed over the two sub-problems to ensure full convergence of the solution at every time step.

As opposed to the simultaneous solution approach [165, 265, 134, 138], where all the unknowns (displacements, pressures, and saturations) are solved for simultaneously at each time step, the sequential iterative approach [202, 277, 10, 9, 138, 147] solves the system separately for the mechanics (displacements, Lagrange multipliers) and the flow (pressures, saturations).

5.4.1 Mechanics sub-problem

We solve the linear systems of equations of the mechanical problem using Newton's method. Given an approximation $[\boldsymbol{U}_b^{n+1}, \boldsymbol{L}_a^{n+1}]^{(k)}$ to the solution at t_{n+1}, an improved solution is obtained as $[\boldsymbol{U}_b^{n+1}, \boldsymbol{L}_a^{n+1}]^{(k+1)} = [\boldsymbol{U}_b^{n+1}, \boldsymbol{L}_a^{n+1}]^{(k)} + [\delta\boldsymbol{U}_b^{n+1}, \delta\boldsymbol{L}_a^{n+1}]^{(k)}$, where the correction is the solution to the system of linear equations:

$$\begin{bmatrix} \boldsymbol{K} & \boldsymbol{C}^T \\ \boldsymbol{C} & 0 \end{bmatrix}^{(k)} \begin{bmatrix} \delta\boldsymbol{U}_b \\ \delta\boldsymbol{L}_a \end{bmatrix}^{(k)} = - \begin{bmatrix} \boldsymbol{R}_u \\ \boldsymbol{R}_l \end{bmatrix}^{(k)}, \tag{5.68}$$

where the individual entries of the block matrix are

$$\boldsymbol{K}_{bb} = \int_\Omega \boldsymbol{B}_b^T \boldsymbol{D} \boldsymbol{B}_b d\Omega, \tag{5.69}$$

$$\boldsymbol{C}_a = \int_{\Gamma_f} \boldsymbol{\eta}_a \cdot (\boldsymbol{\eta}_{b_+} - \boldsymbol{\eta}_{b_-}) d\Gamma. \tag{5.70}$$

In the equations above, $\boldsymbol{K}$ is the stiffness matrix and it is symmetric positive definite; $\boldsymbol{C}$ is the part of the Jacobian associated with the slip constraint, Eq. (5.50), and consists of direction cosine matrices to convert from the global coordinate system to the fault coordinate system (vice versa for $\boldsymbol{C}^T$). Note that for a linear elastic material with time-independent material properties and boundary conditions, the Jacobian matrix does not change with time, although the residuals may change due to coupling with the flow. To visualize the fault contribution to the linear system, we

can write Eq. (5.68) as

$$\begin{bmatrix} \boldsymbol{K}_{bb} & \boldsymbol{K}_{bb_+} & \boldsymbol{K}_{bb_-} & \boldsymbol{0} \\ \boldsymbol{K}_{b_+b} & \boldsymbol{K}_{b_+b_+} & \boldsymbol{0} & \boldsymbol{C}_{b_+a}^T \\ \boldsymbol{K}_{b_-b} & \boldsymbol{0} & \boldsymbol{K}_{b_-b_-} & -\boldsymbol{C}_{b_-a}^T \\ \boldsymbol{0} & \boldsymbol{C}_{b_+a} & -\boldsymbol{C}_{b_-a} & \boldsymbol{0} \end{bmatrix}^{(k)} \begin{bmatrix} \delta \boldsymbol{U}_b \\ \delta \boldsymbol{U}_{b_+} \\ \delta \boldsymbol{U}_{b_-} \\ \delta \boldsymbol{L}_a \end{bmatrix}^{(k)} = - \begin{bmatrix} \boldsymbol{R}_u \\ \boldsymbol{R}_{u_+} \\ \boldsymbol{R}_{u_-} \\ \boldsymbol{R}_l \end{bmatrix}^{(k)}, \tag{5.71}$$

where

$$\boldsymbol{C}_{b_+a} = \int_{\Gamma_f} \boldsymbol{\eta}_a \cdot \boldsymbol{\eta}_{b_+} d\Gamma, \tag{5.72}$$

$$\boldsymbol{C}_{b_-a} = \int_{\Gamma_f} \boldsymbol{\eta}_a \cdot \boldsymbol{\eta}_{b_-} d\Gamma. \tag{5.73}$$

Note that the fault slip, $\boldsymbol{D}_a$, is in the right hand side, $\boldsymbol{R}_l$, and is, therefore, assumed to be known. It is either prescribed as part of the problem definition, or if a constitutive model for fault friction is given, it is separately computed from Eq. (5.53). In that case, the mechanics problem is nonlinear because fault slip is a function of the fault tractions (the Lagrange multipliers), which are limited by the fault constitutive model and depend on the slip. Hence, an iterative scheme is employed to solve the contact problem and determine the slip. The algorithm is as follows:

1. If $\tau > \tau_f$, or if $\tau < \tau_f$ but the iteration has not converged due to overshoot in slip from the previous iteration, compute the perturbation in the Lagrange multipliers, $\delta \boldsymbol{L}_a^{p+1}$, necessary to satisfy the fault constitutive model for the current estimate of slip, $\boldsymbol{D}_a^p$, as follows

$$\delta L_{a,i}^{p+1} = (1 - \delta_{i,n_{\text{dim}}}) L_{a,i}^p \left(\frac{\tau_a^p - \tau_{f,a}^p}{\tau_a^p} \right), \quad 1 \leq i \leq n_{\text{dim}}, \ \forall a = 1, \ldots, n_{f,\text{node}}, \tag{5.74}$$

   where p is the iteration number of this inner loop, and $\delta_{i,n_{\text{dim}}}$ is the delta function ensuring that only the shear components of the Lagrange multiplier are perturbed.

2. Compute the increment in fault slip, $\delta \boldsymbol{D}_a^{p+1}$, from increments in $\boldsymbol{U}_{b+}^{p+1}$ and $\boldsymbol{U}_{b-}^{p+1}$, corresponding to the perturbation in the Lagrange multipliers, assuming

that the deformation is localized to the fault nodes only. Solve three linear subsystems, extracted from Eq. (5.71), for the positive side nodes, the negative side nodes, and the Lagrange nodes on the fault

$$\begin{aligned} \boldsymbol{K}_{b+b+}\delta\boldsymbol{U}_{b+}^{p+1} &= -\boldsymbol{C}_{b+a}^{T}\delta\boldsymbol{L}_{a}^{p+1}, \\ \boldsymbol{K}_{b-b-}\delta\boldsymbol{U}_{b-}^{p+1} &= \boldsymbol{C}_{b-a}^{T}\delta\boldsymbol{L}_{a}^{p+1}, \\ \delta\boldsymbol{D}_{a}^{p+1} &= \boldsymbol{C}_{a}(\delta\boldsymbol{U}_{b+}^{p+1} - \delta\boldsymbol{U}_{b-}^{p+1}), \end{aligned} \tag{5.75}$$

where the bulk deformation term, the body weight term, and the boundary traction term from the Eq. (5.62) do not appear because they are assumed fixed during solution of the contact problem.

5.4.2 Multiphase flow sub-problem

We solve the linear system of equations of the multiphase flow problem using Newton's method. The correction vector is the solution of linear equations:

$$\begin{bmatrix} \frac{\partial \boldsymbol{R}_w}{\partial \boldsymbol{p}_g} & \frac{\partial \boldsymbol{R}_w}{\partial \boldsymbol{S}_w} \\ \frac{\partial \boldsymbol{R}_g}{\partial \boldsymbol{p}_g} & \frac{\partial \boldsymbol{R}_g}{\partial \boldsymbol{S}_w} \end{bmatrix}^{(k)} \begin{bmatrix} \delta \boldsymbol{p}_g \\ \delta \boldsymbol{S}_w \end{bmatrix}^{(k)} = - \begin{bmatrix} \boldsymbol{R}_w \\ \boldsymbol{R}_g \end{bmatrix}^{(k)}, \tag{5.76}$$

where the partial derivatives of the residuals are evaluated using the constitutive equations (Eq. (5.30) and Eq. (5.32)) that relate rock and fluid properties to the fluid pressures and saturations.

5.4.3 Fixed-stress sequential method

In this work, we use the fixed-stress sequential iterative method [149] to solve the coupled multiphase geomechanics problem. In this method, the flow sub-problem is solved first keeping the rate of the volumetric total stress fixed, then the mechanics

sub-problem is solved keeping the fluid pressures and the saturations fixed:

$$\begin{bmatrix} \boldsymbol{U}^n \\ \boldsymbol{L}^n \\ \boldsymbol{p}_g^n \\ \boldsymbol{S}_w^n \end{bmatrix} \xrightarrow{\mathcal{A}^{\text{flow}}} \begin{bmatrix} \boldsymbol{U}^* \\ \boldsymbol{L}^* \\ \boldsymbol{p}_g^{n+1} \\ \boldsymbol{S}_w^{n+1} \end{bmatrix} \xrightarrow{\mathcal{A}^{\text{mech}}} \begin{bmatrix} \boldsymbol{U}^{n+1} \\ \boldsymbol{L}^{n+1} \\ \boldsymbol{p}_g^{n+1} \\ \boldsymbol{S}_w^{n+1} \end{bmatrix}, \tag{5.77}$$

where $\mathcal{A}^{\text{flow}} : R_w = 0, R_g = 0, \delta_t \sigma_v =$ prescribed, is the multiphase flow sub-problem with fixed rate of volumetric total stress, and $\mathcal{A}^{\text{mech}} : \boldsymbol{R}_u = \boldsymbol{0}, \boldsymbol{R}_l = \boldsymbol{0}, p_g, S_w =$ prescribed, is the mechanics sub-problem with fixed flow variables. Superscript $*$ indicates intermediate solution. The volumetric total stress, σ_v, appears in the accumulation term, $\delta_t \left(\rho_g \frac{b_g \sigma_v}{K_{dr}} V_b \right)$ of the multiphase flow equations, Eq. (5.65) and Eq. (5.66). To keep the rate of σ_v fixed during the flow solve, this term is evaluated explicitly using the value of $\delta_t \sigma_v$ from the previous sequential iteration.

This sequential procedure is iterated at each time step until convergence of the full solution, which is then identical to the solution obtained using the simultaneous solution approach. Recently, it has been shown that the fixed-stress operator split is unconditionally stable, it enjoys the excellent convergence properties compared with the other unconditionally stable sequential iterative method (the undrained split) [149, 147, 150].

5.5 Implementation

We developed a coupled multiphase flow and geomechanical simulator by coupling Stanford's General Purpose Research Simulator (GPRS) [38, 200] as the flow simulator, and PyLith [3, 2] as the mechanics simulator. Below we describe the major steps in the development of this coupled simulator.

5.5.1 The flow simulator

GPRS is a general purpose, object-oriented, reservoir simulator for multiphase/multicomponent subsurface flows. It treats element connections through a general connection list, which allows for both structured and unstructured grids. GPRS is capable of handling complex production and injection scenarios in the field, such as wells perforated at multiple depths and flowing under variable rate and pressure controls. The original simulator [38, 200] does not account for coupling with the mechanical deformation, and it models the mechanical behavior of the system through a user-provided *rock compressibility* [13]. We modified and extended the original code to implement the coupling with the mechanics simulator (Fig. 5-4). In particular, we implemented the functionality to compute the modified accumulation term in the fluid phase mass balance equations, Eq. (5.65) and Eq. (5.66). We also modified the setup of the linear system to implement the flow step of the fixed-stress sequential solution scheme, Eq. (5.77).

5.5.2 The mechanics simulator

PyLith is a finite element code for the simulation of static and dynamic large-scale deformation problems [3, 271, 2]. Much of its development has been motivated by the modeling of earthquake physics; however, its applicability extends to problems at any other scale, such as the reservoir scale or the laboratory scale. Some of the advantages of PyLith are: (1) It is an open-source code and can be modified for specific purposes; (2) It is written using C++ and Python languages and is extendable; (3) It is suitable for parallel computing; (4) It allows localized deformation along discrete features, such as faults; (6) It is well integrated with meshing codes, such as LaGriT for tetrahedral meshes [156] and CUBIT for hexahedral meshes [57]. Originally, PyLith is not coupled to any fluid flow model. We modified the original PyLith code and coupled it with the flow simulator, GPRS (Fig. 5-5). In particular, we implemented a C++ class, *iGPRS*, to allow communication between the flow and the mechanics simulators. *iGPRS* provides the functionality required for exchanging information

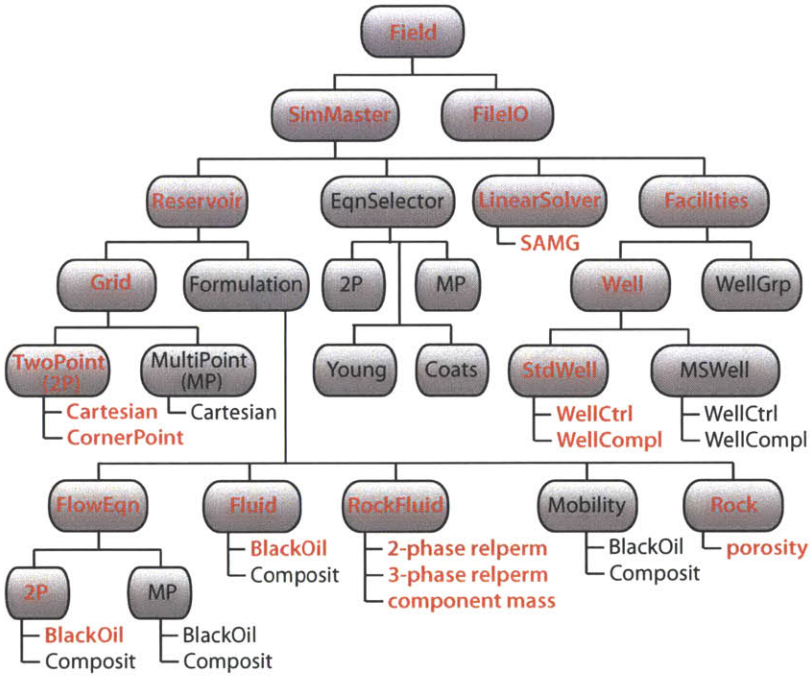

Figure 5-4: Main modules in the GPRS flow simulator. Red color indicates that the code for that particular module has been modified in the course of development of the coupled simulator. Black-oil (*BlackOil*) and Compositional (*Composit*) are two types of flow simulations. A Black-oil simulation does not consider changes in composition of the flowing phases whereas a Compositional simulation does. *2P* and *MP* denote two-point flux approximation and multi-point flux approximation, respectively.

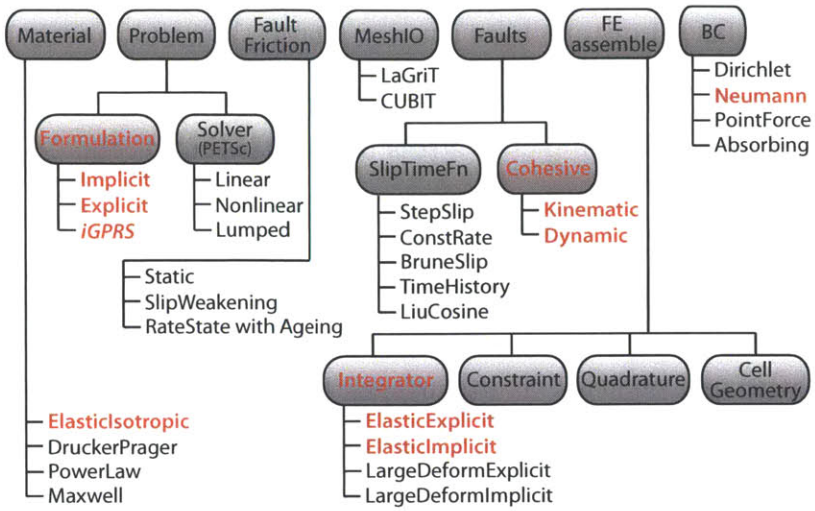

Figure 5-5: Main modules in the PyLith mechanics simulator. Red color indicates that the code for that particular module has been modified in the course of development of the coupled simulator. *iGPRS* is a new module added in PyLith that provides the functionality to interface PyLith with GPRS. It also serves as a datastore for exchanging data between the two simulators.

(pressures, saturations, and volumetric total stress) between the two simulators.

PyLith supports distributed memory parallelization (Message Passing Interface or MPI) whereas GPRS's parallelization is based on the shared memory architecture (Multi-processing or OpenMP). We integrated the two such that we can run the coupled simulator on a cluster with multiple compute nodes (distributed memory) where individual nodes have multiple cores or processors (shared memory).

5.5.3 Grid

We use a single grid for both GPRS and PyLith. The grid is generated using CUBIT [57] or LaGriT [156] software. We define geologic surfaces, material regions, faults, and pinch-outs during the geometry creation stage. Then we mesh the domain with hexahedral elements using a fine mesh in the reservoir domain and an increasingly coarse mesh in the overburden, underburden, and sideburden regions. We export the grid in a finite-element format such as the netCDF format [57], for PyLith. We process the grid file using a MATLAB script to generate the equivalent finite-volume grid in the reservoir domain with element centroid coordinates, element

bulk volumes, and face transmissibilties in the Corner Point Geometry format [229]. GPRS uses the finite-volume grid for simulating flow. The two simulators exchange pressures, saturations, and volumetric stress information inside the flow domain.

5.5.4 Implementation of faults

To support relative motion across fault surfaces, PyLith modifies the grid topology to create zero-thickness fault elements, and adds additional degrees of freedom to hold the Lagrange multipliers and fault slip vectors at the fault nodes [2, 4] (Figs. 5-1–5-2). PyLith solves the contact problem assuming that the deformation is limited to the fault nodes (Eq. (5.75)). If this assumption is not met (for example, when the fault slips over the entire domain), it leads to poor convergence of the iterative scheme used to solve the contact problem. Also, if the fault friction coefficient changes significantly with slip (for example, in Rate- and State- dependent models, Eq. (5.37)), it leads to large changes in $\tau_{f,a}$ at every iteration and the convergence may degrade. To improve the convergence, a line-search routine is used as part of the iterative scheme to find the optimum perturbation in the Lagrange multipliers [4] that minimizes the combined mismatch between the fault friction and the fault traction at all the fault nodes. We modified PyLith's original line-search routine such that the inequality constraint, $\tau \leq \tau_f$, is always honored.

5.5.5 Initialization

The flow simulation is initialized under the assumption of Vertical Equilibrium (Sec. 5.2.5) with the initial pressure and saturation fields calculated using the rock and fluid properties (depth, fluid density, capillary pressure, and fluid contacts). PyLith is initialized with the initial displacement field calculated during an elastic pre-step calculation using initial and boundary displacements and stresses. Initial stresses and boundary tractions are total stresses calculated with bulk densities that account for any fluid contact in the flow domain.

5.5.6 Linear solver

The mechanics problem, Eq. (5.68), leads to a saddle-point problem due to the use of Lagrange multipliers to implement the fault slip constraint. Custom preconditioners are required to solve the linear system efficiently. We solve Eq. (5.68) using the Portable, Extensible Toolkit for Scientific Computation (PETSc [15])'s multigrid preconditioner for the elasticity submatrix in conjunction with a custom fault preconditioner for the Lagrange multiplier submatrix [4, 2]. We solve the flow problem (Eq. (5.76)) using the SAMG multigrid preconditioner [226, 200].

5.6 Representative numerical simulations

We illustrate the validity and applicability of our modeling approach through a number of representative simulations. Some are benchmark problems and others are more realistic scenarios. We conduct these simulations using our coupled simulator.

5.6.1 The Terzaghi problem

Our first example is a uniaxial compaction test under drained conditions, also known as Terzaghi's problem [255, 267]. The purpose of Terzaghi's problem is to test the accuracy of the numerical code for fluid-to-solid coupling. The model problem is a laterally-constrained specimen, subjected to a uniform compressive traction applied suddenly at the top surface (Fig. 5-6a). All sides of the specimen are no-flux boundaries except the top surface, which is open to flow. At $t = 0^+$, the specimen compacts and the pore pressure rises to its undrained value because of the sudden application of the load, also known as the Skempton effect [236]. The undrained values of pressure and total stress serve as the initial condition for the drained part of the consolidation process. As time increases, the specimen consolidates vertically as the fluid leaks out from the top permeable surface. It is a one-dimensional problem with a constant total stress. Under these conditions, diffusion of pore pressure decouples from stress and satisfies a homogeneous diffusion equation with known analytical solution [267].

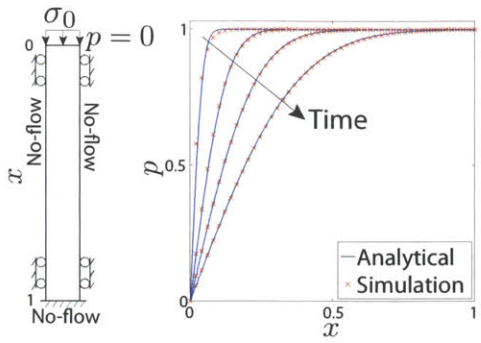

Figure 5-6: Terzaghi's uniaxial compaction problem. Model with boundary conditions is shown on the left. Comparison of pressure evolution between numerical simulation and analytical solution is shown on the right. Dimensionless pressure is plotted against dimensionless distance at four different times.

Strain due to compaction is proportional to the pressure drop.

We used the following values of the relevant parameters: specimen length of 50 m, compression of 2.125 MPa, Young's modulus of 120 MPa, drained Poisson's ratio of 0.3, Biot's coefficient of 1.0, porosity of 0.2, and hydraulic diffusivity of 1.9×10^{-6} m^2/s. Our numerical simulation agrees well with the analytical solution (Fig. 5-6b).

5.6.2 The Mandel problem

Mandel's problem [177, 228, 6] has been used as a benchmark problem for testing the validity of numerical codes of coupled poroelasticity. Its main feature, the Mandel-Cryer effect, is that the pore pressure at the center of a loaded specimen rises above its initial value because of the two-way coupling between fluid flow and solid deformation. Mandel's problem involves a long specimen of rectangular cross-section pressed on one side with an impermeable plate that applies a constant compressive stress σ_0, and fixed on two sides using impermeable roller boundaries (Fig. 5-7). The fourth side of the cross-section is free from normal and shear stresses (traction-free boundary), and is open to the atmosphere (constant pressure boundary). The porous medium is saturated with a slightly compressible fluid, water, with initial pressure set at the reference value, $p_0 = 0$. Since the specimen is long, we assume plane strain conditions, namely that the displacement and fluid flux vanish in the z direction (perpendicular

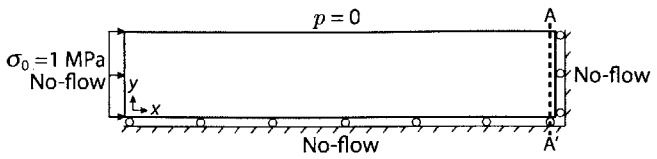

Figure 5-7: Mandel's compaction test. The model dimensions are $L_x \times L_y \times L_z =$ 50 m$\times$ 10 m $\times$ 0.5 m, discretized with 100$\times$20$\times$1 hexahedral cells. A uniform and constant compression of 1 MPa is applied on the left boundary while the right and bottom boundaries are fixed in the normal direction. Top boundary is traction-free. For the flow model, the top boundary is a drained boundary with constant pressure $p = 0$, and other three boundaries are no-flow.

to the paper). With these boundary conditions, the three-dimensional equations of poroelasticity reduce to one-dimensional equations for $\sigma_{xx}(y,t)$ and $p(y,t)$, which can be solved analytically [177, 6]. At $t = 0^+$, a uniform undrained pressure is generated by the Skempton effect, along with uniform stress $\sigma_{xx} = -\sigma_0$. The specimen expands towards the top boundary due to the Poisson effect. As time progresses, the pressure on the top boundary decreases because of fluid drainage, which makes the specimen more compliant there. If the hydraulic diffusivity is small, the effect of drainage is not observed immediately near the no-flux bottom boundary. This results into load transfer of compressive total stress towards the bottom boundary, in response to which the pressure there continues to rise above its undrained value. At long times, all excess pressure vanishes and a uniform horizontal stress, $\sigma_{xx} = -\sigma_0$, returns. Hence, the pressure evolution at points away from the drained boundary is non-monotonic, a phenomenon not observed in a purely diffusive process such as that modeled by the Terzaghi theory, where the pressure is uncoupled from the solid deformation.

We choose a Young's modulus of 18 GPa, drained Poisson's ratio of 0.25, undrained Poisson's ratio of 0.49, reference porosity of 0.05, and hydraulic diffusivity of 2.2×10^{-7} m^2/s. Fig. 5-8 compares the pressure from the analytical solution and the numerical simulation along the width of the specimen near the right boundary at different times. Notice the increase in pressure near $y = 0$ at early times, as per the Mandel-Cryer effect, before it dissipates.

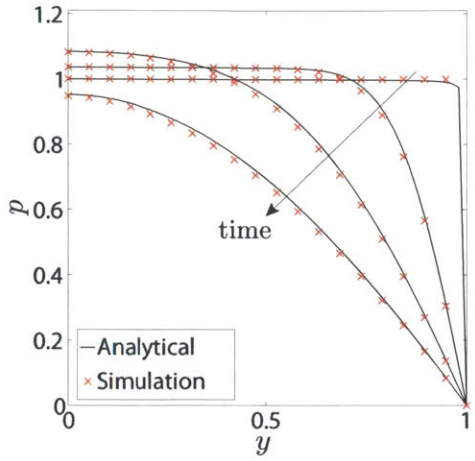

Figure 5-8: Comparison of pressure evolution from the analytical solution and from our coupled simulator for the Mandel test. Pressure is plotted along the AA′ line shown in Fig. 5-7. Pressure is non-dimensionalized with the applied compression, and distance is non-dimensionalized with the width, L_y. Note that, near $y = 0$, the pressure increases at early time in accordance with the Mandel-Cryer effect [177, 6] before beginning to decrease.

5.6.3 PUNQ-S3 subsidence

For the third test of the coupled simulator, we choose the PUNQ (Production forecast Uncertainty Quantification)-S3 reservoir model [95]. PUNQ-S3 model is inspired from a real field in West Africa. It is a dynamic 3D model with multi-well production history. Water support comes from north and west aquifers, while two faults close the reservoir on east and south sides. It has a small gas cap in the center. PUNQ model is commonly used in the oil industry as a benchmark problem for history matching and uncertainty quantification methodologies.

We constructed a geomechanical model of the PUNQ-S3 reservoir by extending the reservoir domain in all three directions to account for overburden, underburden, and sideburden (Fig. 5-9). This allows imposing a reasonable mechanical boundary condition of zero displacements on the five sides of the domain. Top boundary, which is at ground surface, is treated as a traction-free boundary. Model dimension is 13.5 km×15 km×5 km, and it is discretized with 29×38×15 hexahedral elements with average element size of 465 m×395 m×333 m over the entire domain. Reservoir dimension is 3 km×5 km× 0.1 km, and it is discretized with 19×28×5 elements with

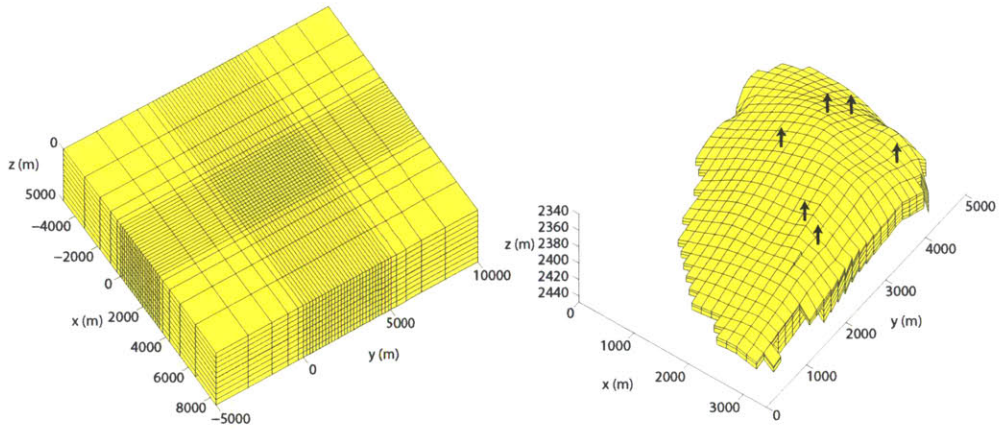

Figure 5-9: PUNQ-S3 grid. Geomechanical grid on the left and reservoir grid on the right. Reservoir domain is in the center of the geomechanical domain and is hidden from the view in the left grid. Mesh becomes coarser as one moves away from the reservoir. Reservoir grid on the right is exaggerated 20 times in the vertical direction.

average element size of 184 m×178 m×11 m in the reservoir. We assume a linearly elastic material with uniform Young's modulus of 82.54 MPa and Poisson's ratio of 0.3. A history period, simulating eight years of production from six wells located close to the gas-oil contact (GOC), was generated followed by another eight years of forecast with five additional infill wells. We obtain the pressure fields by simulating the PUNQ-S3 flow model for 16.5 years in a commercial flow simulator, Eclipse [229]. Then the mechanical deformation is calculated in a mechanics simulator assuming poroelasticity and one-way coupling from flow to mechanics. In Fig. 5-10 and Fig. 5-11, we compare the results from three different sources: our coupled simulator, industry-standard simulator (Abaqus as the mechanics simulator [235]), and Geertsma's semi-analytical solution [105]. Geertsma's semi-analytical solution takes into account the actual shape of the depleting volume and the spatial distribution of the pressure depletion.

We also investigate the effect of two-way coupling (mechanics-to-flow as the second coupling) in the PUNQ simulation since the compressibilities of the produced liquids (oil and water) are closer to that of the rock matrix (Sec. 5.2.2). To create a valid comparison between the one-way and the two-way coupled simulations, same amount of liquid (oil and water) is withdrawn from the wells in both the simulations (Fig. 5-12). As expected, subsidence is less in the two-way coupled case compared to the

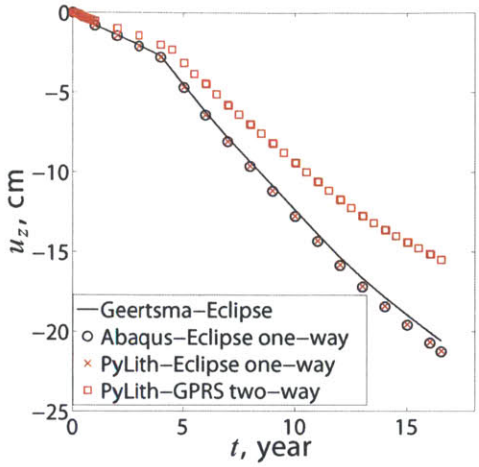

Figure 5-10: Comparison of subsidence above the center of the reservoir from Geertsma's analytical solution with pressure drop from Eclipse, from commercial simulators (Abaqus-Eclipse), and from our coupled simulator for the PUNQ-S3 model. Both the one-way coupled (only flow-to-mechanics coupling) and the more accurate two-way coupled results are shown. Note the excellent agreement between Abaqus and PyLith results. The small discrepancy between the Geertsma's analytical result and one-way coupled results is due to the finite distance from the reservoir to the fixed boundaries of the simulation domain. Effect of mechanics-to-flow coupling is evident in this reservoir as 27% difference between the one-way and two-way coupled results.

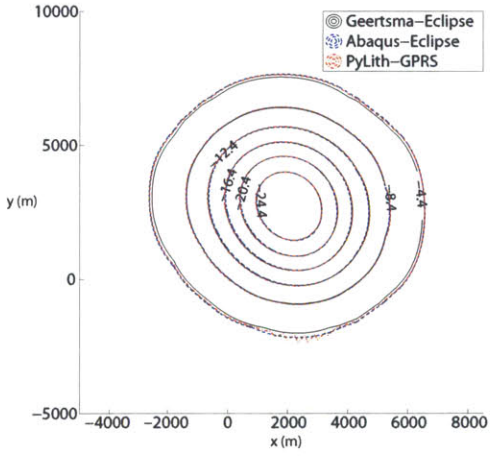

Figure 5-11: Comparison of subsidence contours from Geertsma's semi-analytical solution, from commercial simulators (Abaqus-Eclipse), and from our coupled simulator (PyLith+GPRS) for the PUNQ-S3 model. Contours of the vertical displacement (in cm) on the ground surface are plotted after 16.5 years of production. One-way coupled results are shown.

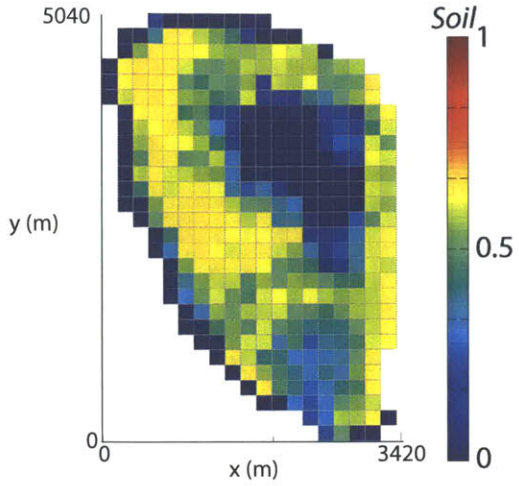

Figure 5-12: Oil saturation in Jul-1983 (t = 6025 day) from the two-way coupled simulation.

one-way coupled case (Fig. 5-10) because compaction of pores resist further pressure decline and compaction.

5.6.4 Faulting due to CO_2 injection: Plane strain

This is an example of CO_2 injection in a deep confined aquifer for the purpose of geologic carbon sequestration [39]. The aquifer is hydraulically compartmentalized with a sealing fault that cuts across it. Storage capacity of the aquifer is limited by overpressurization and slip on the fault. As described in [39], we consider a two-dimensional plane-strain model with the fault under normal faulting conditions, that is, vertical principal stress due to gravity is the largest among the three principal stresses (Fig. 5-13). We choose a value of 0.7 for the ratio of horizontal to vertical initial total stress.

CO_2 is injected at a depth of 1500 m in the confined aquifer at a constant rate of 169,000 standard cubic feet per day (0.1 kg/s) to pressurize the aquifer and induce fault slip. We use a slip-weakening model for the fault (Eq. (5.36)) in which the coefficient of friction drops linearly from 0.6 to 0.2 over a critical slip distance of 5 mm. The fault cohesion strength is 0 MPa. Permeability and porosity are as follows: 100 md and 0.1 (aquifer), 0.0001 md and 0.01 (cap rock), and 10 md and 0.1 (otherwise). Young's modulus and Poisson's ratio are 10 GPa and 0.25, respectively. We use a van

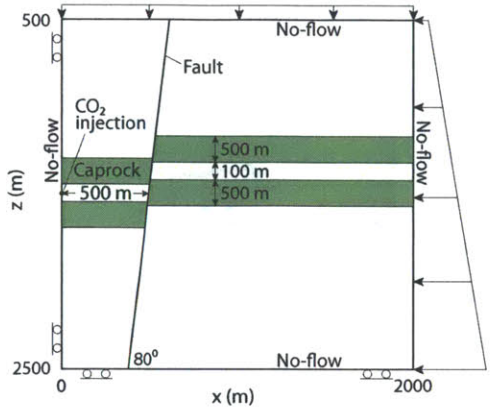

Figure 5-13: Geometry of the CO_2 injection plane strain case (adapted from [39]). CO_2 is injected in the confined aquifer at a depth of 1500 m. The aquifer is bounded on the top and bottom by a low-permeability caprock, and the fault is impermeable to flow.

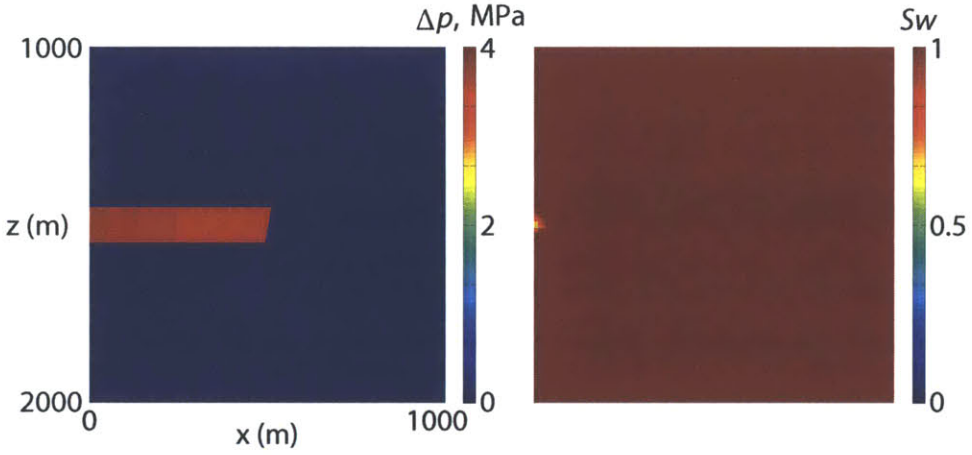

Figure 5-14: CO_2 injection in the plane strain case. Overpressure (left) and water saturation (right) at $t = 21$ day.

Genuchten capillary pressure function [262], $P_{wg} = p_g - p_w = P_o((S_n)^{-1/m} - 1)^{1-m}$, $S_n = (S_w - S_{wlc})/(1 - S_{wlc})$, $S_{wlc} = 0.1S_{wl}$, where P_o is the entry pressure and S_{wl} is the irreducible water saturation. We choose irreducible saturations of $S_{wl} = 0.12$ and $S_{gl} = 0.001$, for water and gas, respectively. We set $P_o = 13.8$ kPa and $m = 0.5$. We use Corey type relative permeability functions [36], $k_{rw} = (\hat{S}_w)^p$, $k_{rg} = (1 - \hat{S}_w)^p$ and $\hat{S}_w = (S_w - S_{wl})/(1 - S_{wl} - S_{gl})$. We choose an exponent $p = 2$. We take gas and water densities as functions of pressure from [142].

After 20 days of injection, pressure in the aquifer increases approximately uniformly by 3.6 MPa (Fig. 5-14). Overpressure causes volumetric expansion of the

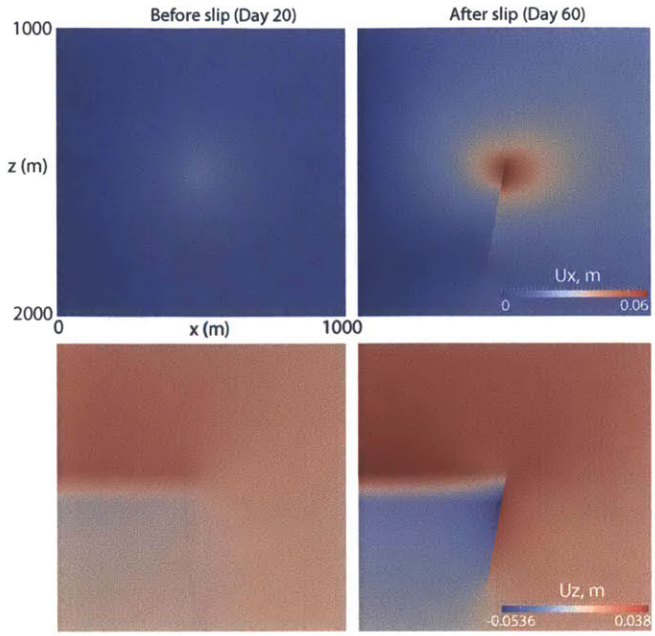

Figure 5-15: CO_2 injection in the plane strain case. Displacement fields in the horizontal and vertical directions (top row and bottom row, respectively) at two different times: $t = 20$ day (left) and $t = 60$ day (right). Notice the discontinuity in the displacement field across the fault at $t = 60$ day as a result of slip. The rupture propagates along the fault, asymmetrically away from the nucleation point at 1550 m, with the longer part below the nucleation point due to the imposed normal faulting condition. After 60 days, the rupture spans over 300 m in length.

aquifer (Fig. 5-15). This, in turn, results in an increase in the effective normal tractions throughout the aquifer, and an increase in the magnitude of shear tractions at the top and bottom boundaries of the aquifer, namely, at depths of 1450 m and 1550 m (Fig. 5-16). There are two interesting observations:

1. The stress evolution (Fig. 5-17a) is such that the bottom of the aquifer at 1550 m reaches the failure line ($\mu_s = 0.6$) first because of the applied traction boundary conditions, which favors normal faulting. Downward slip at the 1550 m depth pulls the 1450 m point down such that the direction of change in the shear traction at 1450 m depth slowly reverses until it also fails by reaching the $\mu_s = 0.6$ failure line.

2. The complete rupture sequence (Fig. 5-17b) is a combination of both seismic and aseismic slips along the fault, with multiple seismic events observed at the bottom boundary of the aquifer.

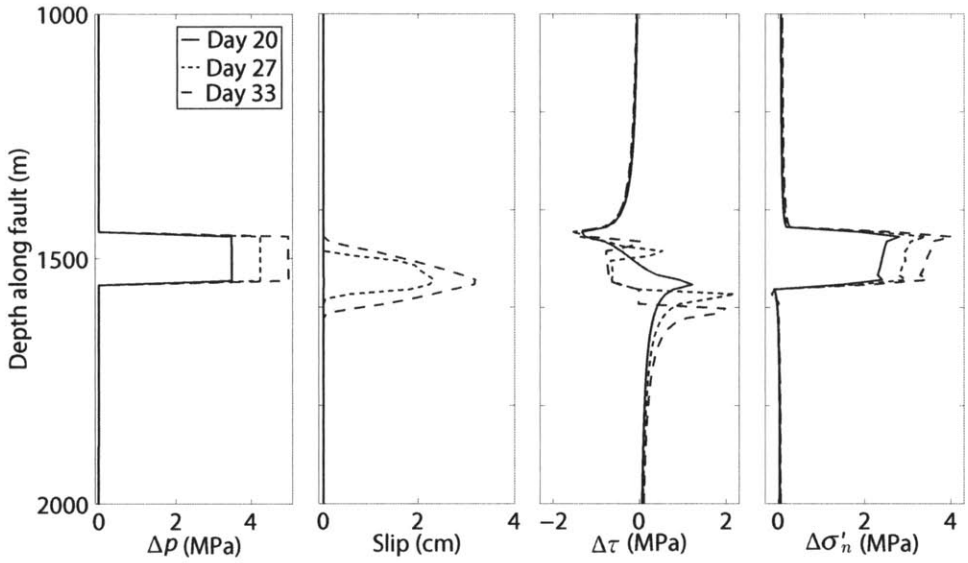

Figure 5-16: Profiles of overpressure, fault slip and change in fault tractions plotted along the fault at three different times: day 20 is just before the first slip, and day 27 and 33 are after two other seismic events noted in Fig. 5-17. The overpressure profile nicely outlines the boundaries of the aquifer. Notice the drop in the shear traction inside the aquifer, and increase outside the aquifer, due to slip events near the 1550 m boundary. Also, note that as points on the fault slip, there is an increase in shear traction at the neighboring non-slipping points, which leads to downward (respectively, upward) movement of the spike in the shear traction below (respectively, above) the aquifer.

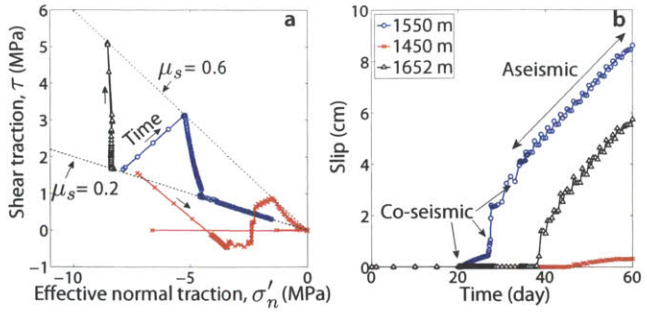

Figure 5-17: Evolution of stress state (a) and slip (b) on the fault at three depths: bottom of the aquifer (1550 m, circles), top of the aquifer (1450 m, crosses), and below the aquifer in the rupture zone (1652 m, triangles). At $t = 21$ day, rupture nucleates just underneath the aquifer at 1550 m depth, which reaches the failure criterion ($\mu_s = 0.6$ line) before any other point on the fault. This leads to an increase in shear stresses at points adjacent to 1550 m, which fail in succession. The point at 1652 m depth fails at $t = 38$ day. There is only a small change in the effective normal traction at 1652 m point because there is no overpressure below the aquifer. Change in effective normal traction is not zero because of deformation-induced stress changes. The top boundary at 1450 m ruptures at $t = 45$ day, and relaxes quickly to almost zero shear traction. Notice multiple seismic events in the slip plot. The three events marked with arrows are analyzed in Fig. 5-16.

5.6.5 Faulting due to CO_2 injection: 3D

This example is similar to the previous one except that here we consider a 4 km×4 km×2 km three-dimensional domain with a 200 m thick anticlinal aquifer (Fig. 5-18), and we use the rate and state dependent model (Eq. (5.37)) for the fault friction. The rate and state constitutive parameters are: $A = 0.002$, $B = 0.08$, $d_c = 1$ cm, $\mu_0 = 0.4$, and $\tau_c = 0$. These values strongly favor unstable sliding on the fault. Rock and fluid properties are identical to the plane strain case above. CO_2 is injected at a rate of 30 million standard cubic feet per day (17.64 kg/s) leading to overpressurization of the aquifer (Fig. 5-19). The anticline is off-centered in y leading to asymmetry in the overpressure field. Rupture nucleates at the base of the aquifer at (x, y, z) =(2850 m, 2900 m, 1600 m) after 202 days of CO_2 injection, and propagates on the fault along the bottom boundary of the aquifer. After approximately two months, a second rupture sequence begins along the layer just above the base of the aquifer. At $t = 320$ day, the underburden rock layer below the anticline reaches the failure criterion and slips, and the rupture subsequently propagates in both up-dip and down-dip directions on the

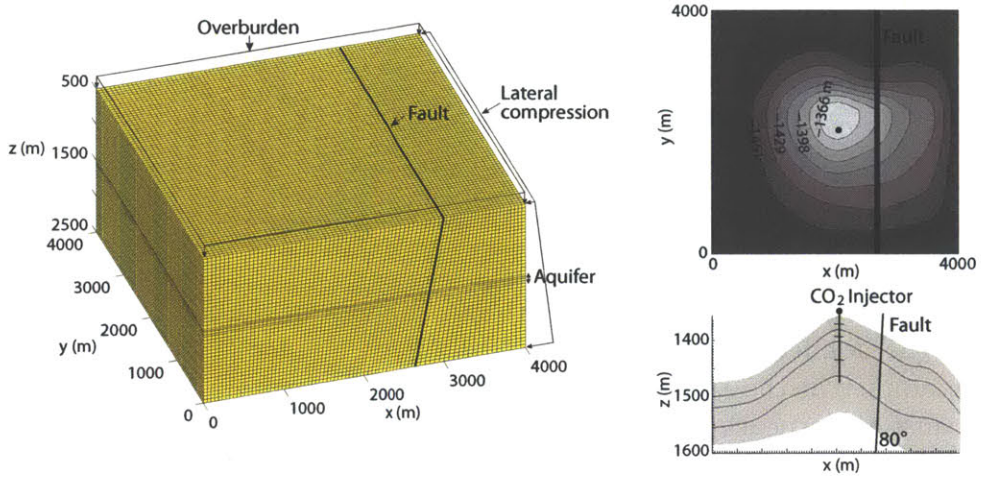

Figure 5-18: CO_2 injection in a 3D anticlinal aquifer. Left: geomechanical domain is shown with the traction boundary conditions on the top and on the right boundaries. Lateral compression is 0.7 times the overburden. Zero normal displacement is imposed on all other boundaries. No-flow boundary condition is imposed on all the boundaries. Flow domain is composed of the four layers marked as *aquifer*, and the injector is located near the center of the anticline. The fault is impermeable to flow. Right: plan view (top figure) and cross-section view (bottom figure) of the aquifer are shown. Depth contours are marked in the plan view. The cross-section view is exaggerated in the vertical direction.

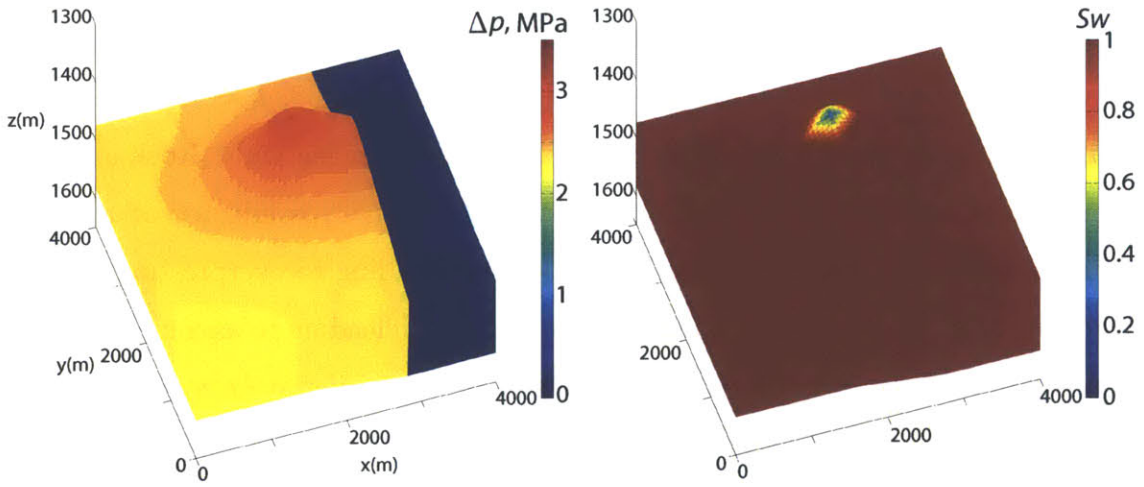

Figure 5-19: CO_2 injection in a 3D anticlinal aquifer. Overpressure (left figure) and water saturation (right figure) in the aquifer layers at $t = 202$ day, when fault slip begins.

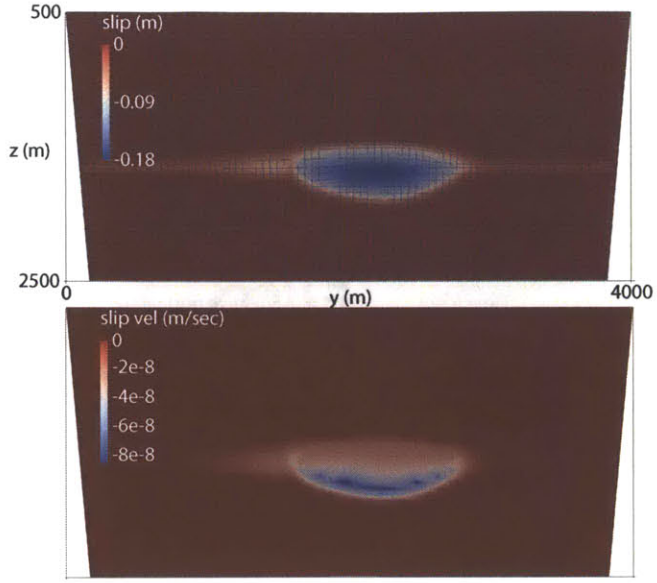

Figure 5-20: CO_2 injection in a 3D anticlinal aquifer. Slip (top) and slip velocity (bottom) on the fault plane at $t = 400$ day. A video that shows the dynamics of fault rupture from the coupled flow-geomechanics simulation is included in the Supplementary Material.

fault with higher slip velocity in the down-dip direction (Fig. 5-20). Downward slip is favored due to the imposed normal faulting condition. The rupture front adopts an ellipsoidal shape following the profile of the aquifer, which is being pressurized. In Fig. 5-21, we show the evolution of slip and traction on the fault at three points directly under the anticline–base of the aquifer, top of the aquifer, and below the aquifer in the underburden rock. Slip velocity at the base is small and constant in the beginning resulting in stable sliding; then it increases sharply due to slip-weakening before decreasing again back to a new stable sliding value that is higher than the earlier stable sliding value (Fig. 5-21). Since the fault is represented as a two-dimensional surface, we can compute the magnitude of the earthquake from the actual rupture area. The earthquake magnitude is given by the expression, $M_w = \frac{2}{3}\log_{10} M_0 - 6.0$, where the seismic moment is given by $M_0 = \int_{\Gamma_f} G|\boldsymbol{d}|d\Gamma$, $|\boldsymbol{d}|$ is the magnitude of the final slip vector at the end of the earthquake, and G is the shear modulus [121]. Substituting the values, we obtain $M_w = 3.4$ at $t = 500$ day. Note that since this is a quasi-static simulation with very small slip velocities, earthquake here refers to the seismic event producing equivalent amount of slip.

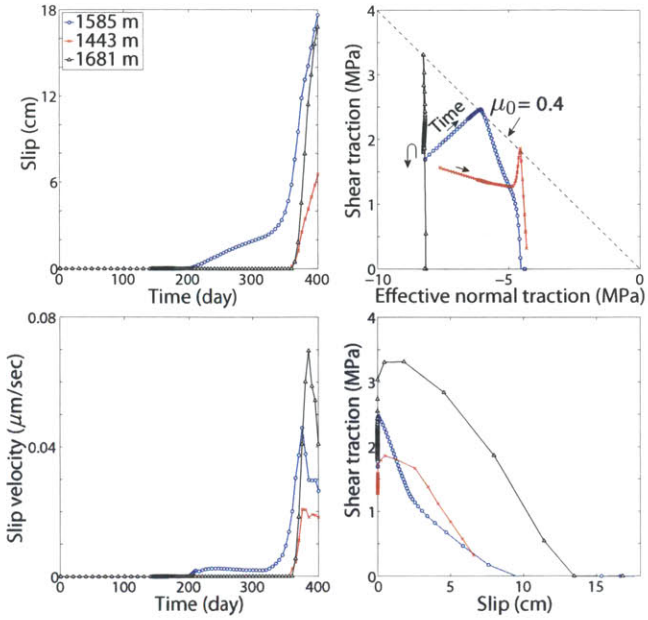

Figure 5-21: CO_2 injection in a 3D anticlinal aquifer. Evolution of slip and state of stress on the fault at three depths under the anticline: 1585 m (bottom of the aquifer), 1443 m (top layer of the aquifer), and 1681 m (below the aquifer in the underburden). Slip, slip velocity, and shear traction are in the downdip direction along the fault.

5.7 Conclusion

We have presented a new computational model to simulate the coupling between multiphase flow and poromechanics of faults, and developed a two-way coupled simulator that interlaces a geomechanics simulator (PyLith) with a multiphase flow simulator (GPRS). Our approach enjoys the following features:

1. It is computationally efficient because it relies on a sequential solution of the two-way coupled problem.

2. It is unconditionally stable, due to the use of the fixed-stress sequential split between multiphase flow and deformation. The model accounts rigorously for multiphase flow effects through a fully nonlinear poromechanics formulation.

3. It represents faults as surfaces embedded in a three-dimensional domain, therefore allowing for a discontinuous displacement field across the fault (fault slip). Our approach elucidates the role of the pressure discontinuity across the fault on the stability of the fault through the definition of a 'fault pressure'.

4. It incorporates realistic fault constitutive behavior, such as the rate- and state-dependent friction model, capable of simulating runaway fault slip typical of earthquakes.

We assume quasi-static mechanical deformation by neglecting the inertial term in the solid momentum balance equation, and we use an implicit time-marching scheme for the coupled simulation. While this is an excellent approximation prior to fault rupture, during fault slip the inertial term is not negligible due to propagation of seismic waves. We are currently extending the capabilities of our simulation tool to implement a dynamic implicit–explicit time marching scheme that can take small time steps required to resolve the propagation of rupture on the fault, while taking orders of magnitude larger time steps during aseismic periods.

Our framework allows us to investigate fault slip and earthquake induced in underground reservoirs due to coupled processes of fluid flow and mechanical deformation such as those encountered during groundwater withdrawal and geologic CO_2 storage. In this work, we have demonstrated the effectiveness and applicability of our approach through a few synthetic, but realistic, examples. We are currently applying our computational model for the study of ground deformations detected from geodetic measurements via GPS and InSAR [118, 85, 253], and for the *post mortem* analysis of natural or induced earthquakes [110, 261, 145, 35].

Chapter 6

Joint inversion of flow and surface deformation data

6.1 Introduction

Inversion is the process of estimating unknown subsurface parameters such as porosity, permeability, rock compressibility etc. by assimilating surface measurements such as the ground displacements, well rates and pressures. Usually, measurements are available at different points in space and at different time steps whereas rock parameters are assumed to vary only in space. Moreover, inversion is easier if we assume that spatial variation in each parameter follows the Gaussian distribution, which is completely defined in terms of a mean and a variance. The Kalman filter is a popular Bayesian statistics approach to estimate model parameters (state of the model) by assimilating measurements of model predictions at different points [80]. Ensemble Kalman Filter (EnKF) is a Monte Carlo approximation of the Kalman filter suitable for large-scale (many unknowns) problems such as the ones encountered in geophysical applications. It requires the ensemble covariance matrix of the prior distributions, measurements and their error covariance matrix, and a forward model to generate predictions of the measurements. Simplification in EnKF comes from the assumption that the true covariance matrix of model parameters can be substituted with the ensemble covariance matrix when the ensemble is a large enough sample from the assumed prior

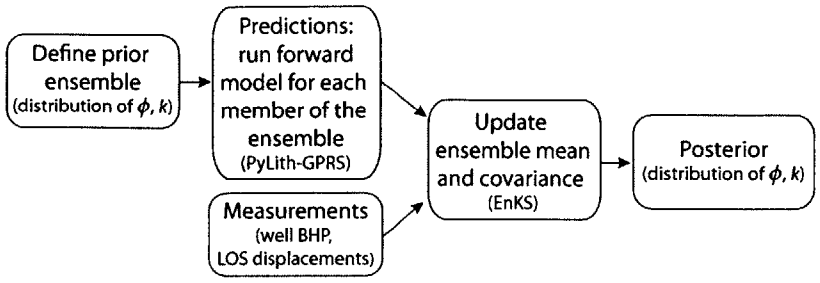

Figure 6-1: Inversion flow chart. *LOS* is an acronym for Line-Of-Sight and *BHP* is an acronym for Bottom Hole Pressure.

distributions of the parameters. See Fig. 6-1. In case of inversion of rock properties from flow and deformation data, the forward simulation model is a coupled flow and mechanics simulator. We use PyLith-GPRS as our coupled flow and geomechanics simulator.

6.2 Ensemble Kalman Smoother

We use the Ensemble Kalman Smoother (EnKS) for estimation and uncertainty reduction of the inversion parameters [78]. Let n be the number of model parameters, m be the number of measurements, and N be the number of members in the ensemble. Neglecting the uncertainty in the forward model, which is deterministic, ensemble means of the model parameters are updated as [79, 78]

$$\boldsymbol{\psi}^{\mathrm{a}} = \boldsymbol{\psi} + \boldsymbol{A}'\boldsymbol{S}^T\boldsymbol{C}^{-1}(\boldsymbol{d} - \boldsymbol{H}\boldsymbol{\psi}) \tag{6.1}$$

where $\boldsymbol{\psi}^{\mathrm{a}}$ is the updated, and $\boldsymbol{\psi}$ is the prior matrix $(n \times N)$ of ensemble means of the parameters, $\boldsymbol{d}$ is the perturbed measurement matrix $(m \times N)$, $\boldsymbol{A}'$ is the zero-mean perturbation matrix $(n \times N)$ of the ensemble, $\boldsymbol{S} \equiv \boldsymbol{H}\boldsymbol{A}'$ is the matrix $(m \times N)$ of ensemble perturbation predicted with the forward model operator $\boldsymbol{H}$ $(m \times n)$, $\boldsymbol{C} \equiv \boldsymbol{S}\boldsymbol{S}^T + \boldsymbol{E}\boldsymbol{E}^T$ is the combined matrix $(m \times m)$ of auto-covariance of predicted data, $\boldsymbol{S}\boldsymbol{S}^T$, and the measurement error covariance matrix, $\boldsymbol{E}\boldsymbol{E}^T$. $\boldsymbol{E}$ is the zero-mean measurement error matrix $(m \times N)$ for the measurement vector $\boldsymbol{d}_m$ $(m \times 1)$. The perturbed measurement matrix $\boldsymbol{d} \sim \mathcal{N}(\boldsymbol{d}_m; \boldsymbol{E}\boldsymbol{E}^T)$ is created by perturbing $\boldsymbol{d}_m$ N

times. Note that $\boldsymbol{H\psi}$ is the predicted data matrix ($m \times N$) obtained by running the forward model N times. Here, instead of using the classical implementation of Eq. (6.1) in [181] and [75], we used the square root implementation [79] in order to avoid generating random fields to perturb $\boldsymbol{d}_m$. To tackle inversions of large matrices involved, we used fast reduced-rank approximation to singular value decomposition based on random matrix theory described in [119].

6.3 Lombardia dataset

We tested the geomechanical inversion methodology on the Lombardia dataset [253]. The Lombardia site is an underground gas storage (UGS) reservoir in Po River basin of Italy. The permeable and geologically confined reservoir is used for storage of the heating gas during summer months and for withdrawal during winter months. Ground surface motion above the reservoir follows this seasonal cycle of storage and withdrawal, i.e., the surface is uplifted during the injection months, and subsided during the production months. The Lombardia site was selected for this inversion exercise because it has relatively good dataset: well bottom hole pressure (WBHP) in 26 wells of the field for Jan-1981 to Nov-2007 period, and Line-Of-Sight displacement measurements over the reservoir from the Envisat satellite for Jul-2003 to Feb-2007 period. The WBHP obtained from a previous simulation (history-match run of the reservoir) is being treated as the WBHP measurements for this study. Envisat satellite data was processed at MIT to generate smooth LOS surface displacement maps. Note that there is also Radarsat satellite dataset in this region, which was processed by a company (TRE).

We need to estimate the noise covariance or error covariance in the measurements. Assuming independent pressure measurements, we use an identity matrix for the error covariance of the pressure data. For the satellite data, the noise signals are primarily due to the atmospheric variations (water vapor etc.) and they are spatially correlated. Assuming that the noise is spatially stationary and isotropic, the covariance between any two points depends only on the distance between them. We assume that the noise

Parameter	Distribution	Mean	Standard deviation
Reservoir porosity, ϕ	Normal	0.29	0.01
Poisson's ratio, ν	Normal	0.3	0.006
Intercept a in Eq. (6.2)	Normal	-1.86433	0.234
Reservoir horizontal permeability, $\log kh_r$	Normal	2.6	0.03
Parameter	Distribution	Min	Max
Vertical-horizontal permeability ratio, kv_r/kh_r	Uniform	0.8	1.0
Aquifer-reservoir permeability ratio, k_a/k_r	Uniform	0.1	1.0

Table 6.1: Inversion parameters of the Lombardia reservoir. c_m is the uniaxial compressibility and σ'_{vert} is the effective vertical stress.

covariance decays exponentially over some length scale L_c, i.e., the (i, j) element of the error covariance matrix $\boldsymbol{E}\boldsymbol{E}^T$ in Eq. 6.1 is $\exp(-L^{ij}/L_c)$, where L^{ij} is the distance between the ith and jth measurement points [168]. This results in a block-diagonal error covariance matrix, where blocks are the covariance matrices of the individual measurements. We estimated the correlation length L_c at each of the 18 timesteps of the satellite data from the Gaussian smoothing filter applied during the data processing. Range of L_c is from approximately 2 km on 21-May-2006 to approximately 10 km on 29-Aug-2004.

6.4 Inversion parameters

Inversion parameters selected for this exercise are listed in Table 6.1 along with the values used to generate their prior distributions. These values reflect prior information or bias about these parameters. They can be derived from other independent sources such as regional geology, analogous fields, literature, expert opinions etc. We selected these values such that the range in predictions of measurements (WBHP and LOS displacement from simulations based on the prior distributions) encompass the actual measurements. We generate an ensemble of one hundred realizations by randomly drawing from these prior distributions (Fig. 6-2). We run forward model simulations

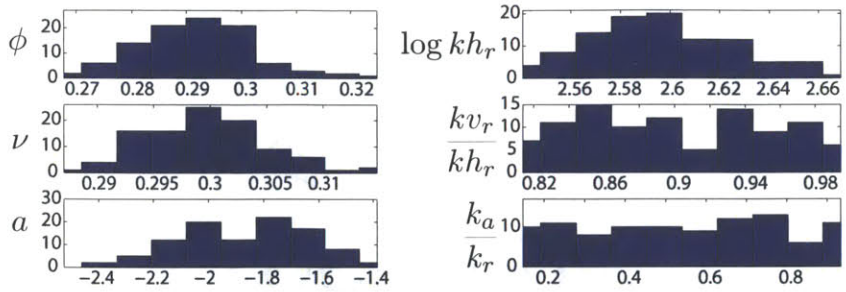

Figure 6-2: Prior distributions of the inversion parameters generated from values in Table 6.1.

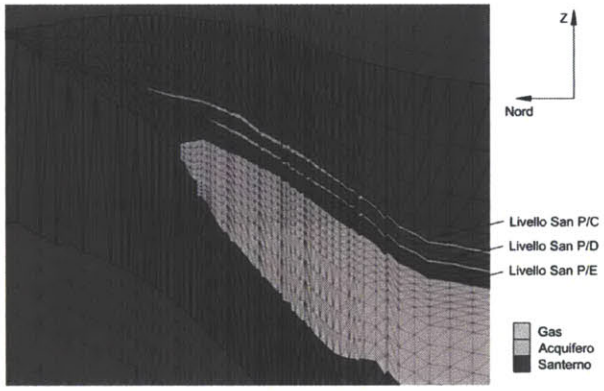

Figure 6-3: Geological model of the Lombardia reservoir with fluid contacts. Notice the San-PE horizon with its gas-water contact and the pinch-out in the north.

(GPRS and PyLith) for each of these realizations.

6.5 Forward model

A forward model generates multiple predictions of the measurements based on multiple realizations of the inversion parameters. In this study, the forward model is a one-way coupled flow and geomechanics model of the Lombardia field. The model construction is divided into three stages: construction of the geological model, construction of the flow model, and construction of the geomechanical model. An existing geological model of Lombardia reservoir that was constructed based on the seismic maps, petrophysical logs, and information about the regional geology was used for this study. Fig. 6-3 shows three important horizons in the Lombardia reservoir: San-PC, San-PD and San-PE. This study focuses on the San-PE horizon, which is the

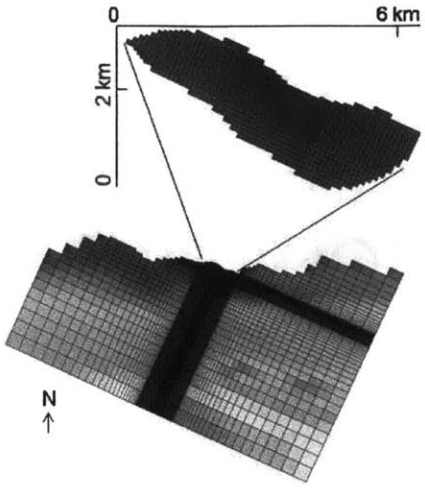

Figure 6-4: Top view of the GPRS flow model (bottom figure) and the gas-bearing region of the reservoir (top figure). Corner point geometry is used to construct an unstructured grid of the flow model. There are 10 layers in the flow model. The grid cell sizes in x and y direction increase logarithmically away from the gas-bearing region.

largest in terms of volume and has been active for the longest duration. Production from San-PE started in 1981 with 12 wells near the top of the gas cap. In 1986, 14 new wells were added to support the underground gas storage (UGS) operation. UGS operation follows the demand and supply of the heating gas, therefore, natural gas is produced during the winter months (November to April) and injected during the summer months (May to October). As shown in Fig. 6-4, the reservoir flow model ($139\times82\times10$, 56×54 km^2) includes the gas-bearing region and the aquifer in San-PE horizon. The gas region is delineated by the gas-water contact towards the south and the pinch-out towards the north. The extent of the aquifer in the south and the aquifer strength were determined during a previous history-match study. Rock properties (porosity, permeability, net-to-gross ratio, and pore compressibility), fluid PVT properties, relative permeability curves, gas-water contact, initial equilibrium pressure, and irreducible water and residual gas saturations are taken from that study. All the boundaries of the reservoir are designated as no-flow boundaries and the model is driven with well gas production and injection rate schedule. Pressure field over the entire reservoir and Well BHP (WBHP) are the two key output results from the flow simulation. Porosity, permeability and pore compressibility are the inversion

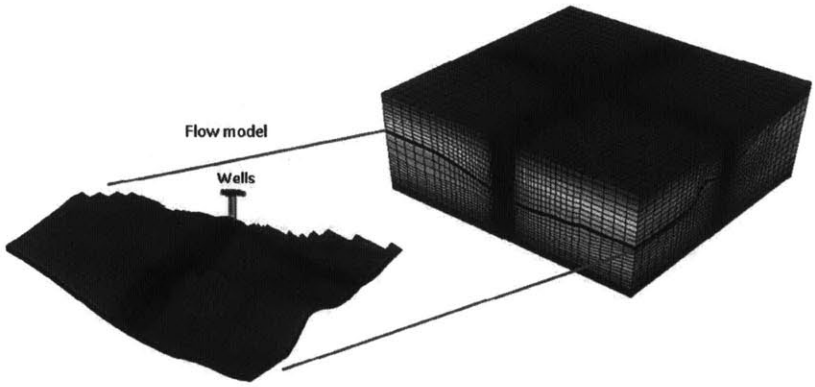

Figure 6-5: PyLith geomechanical grid with a magnified view of the GPRS flow grid. Grids are exaggerated in the vertical direction. Flow occurs only in the reservoir domain, which appears sandwiched between the overburden and the underburden. There are 10 layers in the overburden, 10 layers in the reservoir, and 15 layers in the underburden. The grid cell sizes in x and y direction increase logarithmically away from the central gas-bearing region. Wells are shown as vertical lines in the gas-bearing region of the flow model.

parameters for the flow (Table 6.1).

The geomechanical model is an unstructured finite-element grid (149×92×35, 90×90×5 km^3) created in CUBIT (from the imported ABAQUS grid) by extending the flow model in all three directions to simulate the role of overburden, underburden, and sideburden in reservoir deformation (Fig. 6-5). It also allows us to apply zero horizontal displacement boundary conditions on the four side boundaries, zero displacement on the bottom boundary, and a traction-free condition on the ground surface. The rock is assumed to be elastic with its mechanical properties assigned from an empirical relationship between the uniaxial compressibility and the effective vertical stress,

$$\log c_m = a + b \log \sigma'_{\text{vert}}, \tag{6.2}$$

as shown in Fig. 6-6. Depth varying effective stress is used to assign depth varying compressibility and Young's modulus to the geomechanical grid. Poisson's ratio is assumed to be uniform throughout the domain. The intercept a in the empirical relationship and the Poisson's ratio are the inversion parameters for the mechanics (Table 6.1).

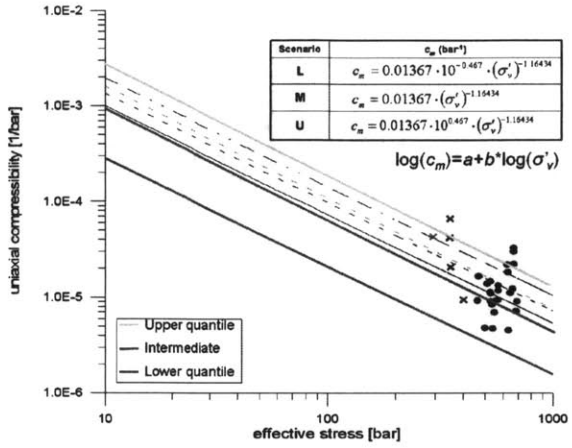

Figure 6-6: Empirical relationship between the rock compressibility c_m and the effective vertical stress σ'_{vert} [128]. Intercept a in Eq. (6.2) is one of the inversion parameters. $b = -1.16434$.

6.6 Inversion methodology

Ensemble-based inversion approach requires a number of the forward model simulations corresponding to different possible realizations of the uncertain parameters. In this study, we ran 100 forward model simulations corresponding to 100 realizations of the uncertain parameters. To save time, we run these simulations using the one-way coupled approach. In the one-way coupled approach, we first run flow simulations for each realization of porosity, permeability, rock compressibility etc. using GPRS followed by poroelastic simulations in PyLith using the pressure field at every time step obtained from the corresponding GPRS simulation. The coupling between the flow and mechanics is provided by the fluid pressure, which changes the effective stress in PyLith. There is no feedback from the mechanics simulation to the flow simulation in this one-way coupled approach. One-way coupled approach is suitable for reservoirs where the mechanics-to-flow coupling is weak e.g. in gas reservoirs (Sec. 5.2.2), where the gas compressibility is much larger than the rock compressibility. The pressure response of the reservoir is determined by the gas compressibility, reservoir permeability, aquifer pressure support (aquifer permeability), reservoir porosity, and well rates.

Inputs to EnKS are the prior distributions of the inversion parameters, predicted

WBHP of 26 wells at 200 equally-spaced discrete time steps from all the GPRS runs and predicted LOS displacements at 2436 ground locations (Persistent Scatterers) at 18 time steps from all the PyLith runs, measured WBHP and LOS displacements, and the error covariance matrix for all the measurements. Outputs of the EnKS are the posterior distributions of the inversion parameters. A narrower posterior distribution means reduction in the uncertainty associated with that particular parameter. Once the posterior distributions are obtained, we run the forward model again, with realizations drawn from the posterior distributions, to confirm the agreement between the predicted and the measured values of WBHP and LOS displacements.

6.7 Results

Quality of the EnKF solution depends on the rank and conditioning of the prior ensemble matrix [79]. In other words, EnKF works best if the prior distributions of inversion parameters capture the 'truth' scenario as well as the uncertainty around it. In our case, it means that the variation in the WBHP and LOS displacements predicted from the simulations with values from the prior distributions should encompass the WBHP and LOS displacement measurements. Fig. 6-7 shows the comparison between the predicted WBHP and the measured WBHP. We see that the spread in the predicted curves indeed captures the measurement curve for the most part. Similarly, Fig. 6-8 shows the comparison of the LOS displacement from the simulations and the measurement at four locations. Fig. 6-9 shows the comparison in terms of 2D maps of the LOS displacement. Values from one of the simulations and the satellite measurement are shown side-by-side for the area recorded by the Envisat satellite. We note that the comparison between the simulated displacement and the measured displacement is poorer than the comparison between the simulated WBHP and the measured WBHP. This can probably be attributed to higher noise in the satellite measurement and its poorer resolution in time and space compared to the WBHP measurement, which is obtained from a history-match simulation.

Once we have the prior predictions (from simulations with realizations from the

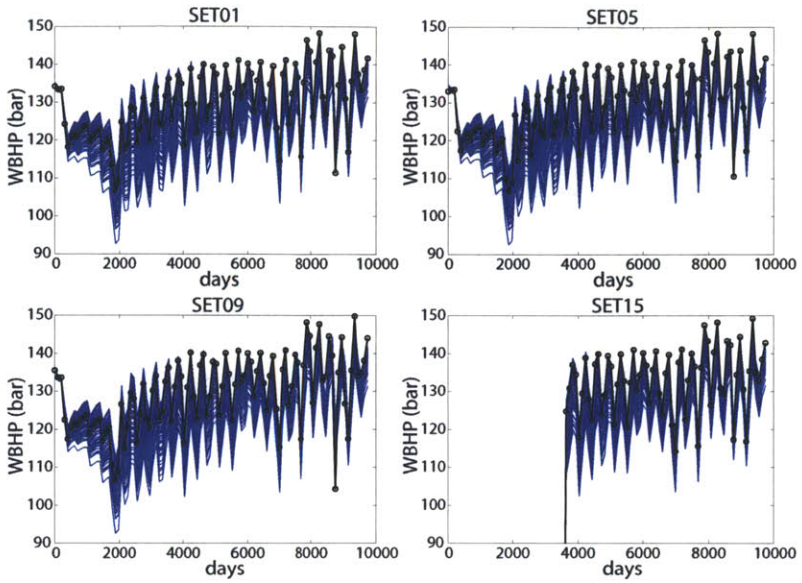

Figure 6-7: Comparison of the Well Bottom Hole Pressure (WBHP) time series from the prior predictions (blue lines) and from the measurement (black line with circles). The WBHP from the history-match run is being treated as the measurement. There are one hundred prediction curves corresponding to the ensemble size of one hundred.

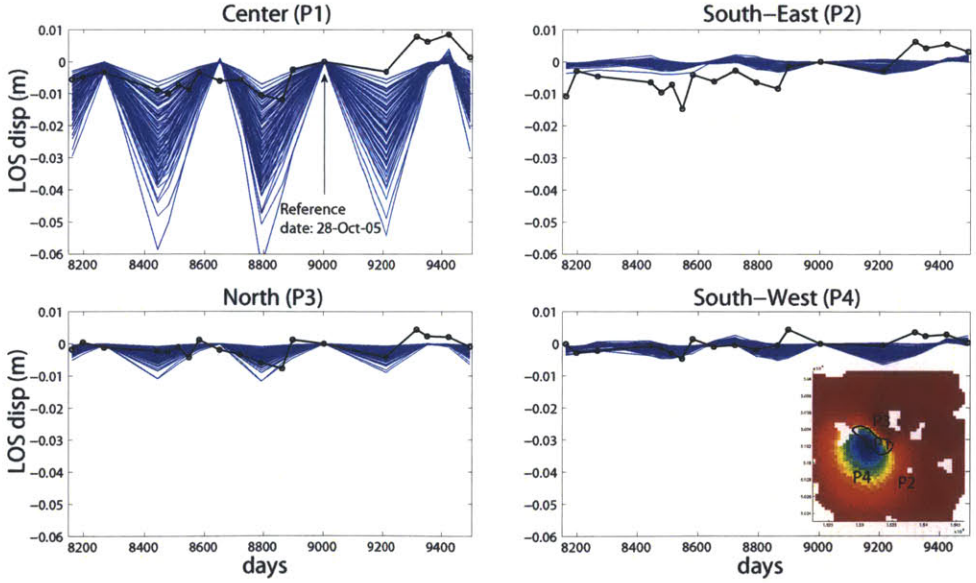

Figure 6-8: Comparison of the Line-Of-Sight (LOS) displacement time series from the prior predictions (blue lines) and the Envisat satellite data (black line with circles) at four locations, which are marked as P1, P2, P3, P4 in the inset.

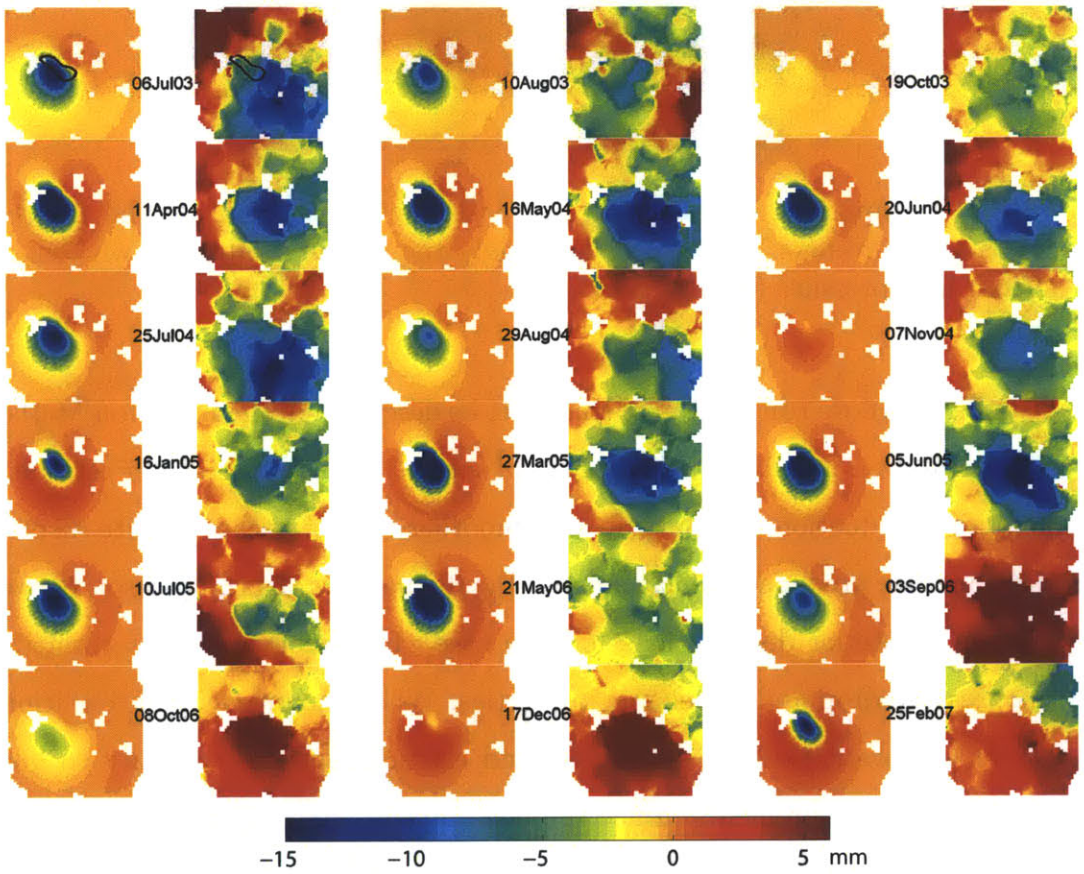

Figure 6-9: Comparison of the Line-Of-Sight (LOS) displacement map from one realization of the prior predictions (left columns) and the Envisat satellite data (right columns) at 18 timesteps. Unit is mm and negative displacement means subsidence. Outline of the gas-bearing region of the reservoir is shown with a solid black line in the first two figures.

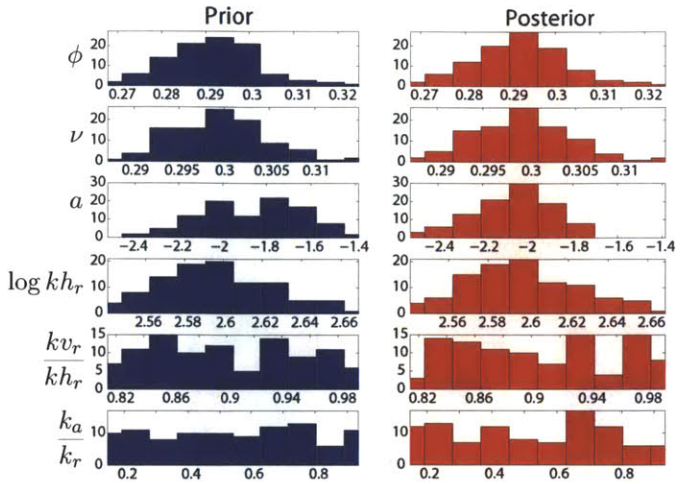

Figure 6-10: Comparison of the prior and posterior distributions of the inversion parameters with inversion performed using only the satellite data i.e. without the well bottom hole pressure (WBHP) data.

prior distributions), we run the EnKS smoother as described in the Inversion Methodology section above. To evaluate the impact of satellite data on parameter estimation and uncertainty reduction, we first run the smoother with only the satellite displacement data and the predicted displacements. Fig. 6-10 shows the comparison between the prior and posterior distributions for this case. Displacement is determined by both the pressure drop and the elastic properties. When the inversion is conditioned to displacements only, both pressure drop and elastic properties can vary to honor the displacement measurements. Since the flow rates are fixed, variation in pressure drop primarily results from variation in permeabilities. Therefore, there is no reduction of uncertainties in k_a and k_r. If it were an oil or water reservoir, we would expect to see some reduction in permeability uncertainty because in that case flow is strongly coupled to mechanics. There is only a small reduction in the uncertainty of the parameter a.

Conditioning to displacement alone is not sufficient to reduce the uncertainty in both the flow and mechanics parameters, especially in permeability which is a flow parameter. Another reason for almost no reduction in uncertainties of the parameters can be that the weights of the displacement measurement are too small in the EnKS smoother. This can be confirmed by comparing the LOS displacements predicted

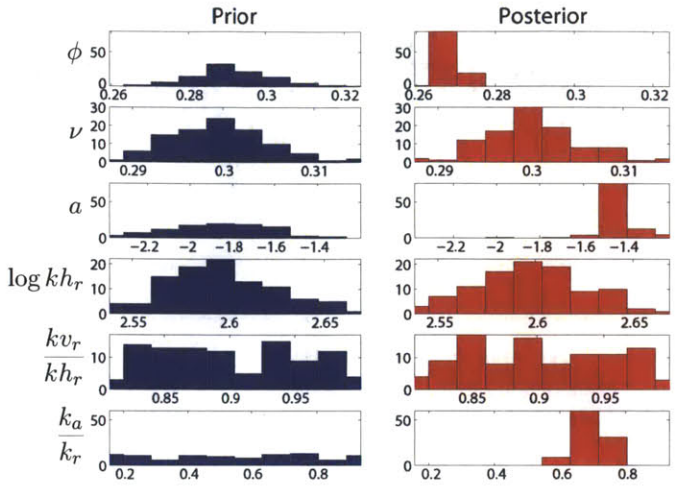

Figure 6-11: Comparison of the prior and posterior distributions of the inversion parameters with inversion performed using both the satellite data and the well bottom hole pressure (WBHP) data.

using these posterior distributions, with the measured displacements. If the spread in the predictions has not decreased compared to the prior displacements, it may indicate that the weights are too small.

Next, we run one iteration of the EnKS smoother using both the WBHP data and LOS displacement data. We used an identity matrix for the error covariance matrix of the WBHP measurement, which assumes independence of the individual pressure measurements. Fig. 6-11 shows the comparison between the prior and the posterior distributions. Since the flow rates and gas compressibility are fixed for all the realizations, pressure response is determined by the porosity and permeability. Therefore, we observe a significant reduction in the uncertainty of porosity and aquifer-reservoir permeability ratio. Reservoir permeabilities (kv_r, kh_r) are mostly unchanged because prior uncertainties in them are already small. Uncertainty reduction in rock elastic parameters, Poisson's ratio and parameter a, is due to the combined effect of conditioning to both the displacement and pressure measurements, with the latter exerting its control through the flow-to-mechanics coupling. However, we only see a minor reduction in spread of the displacement curves (compare Fig. 6-8 with Fig. 6-13). This may suggest that the pressure measurements are disproportionately weighted higher than the displacement measurements during the inversion.

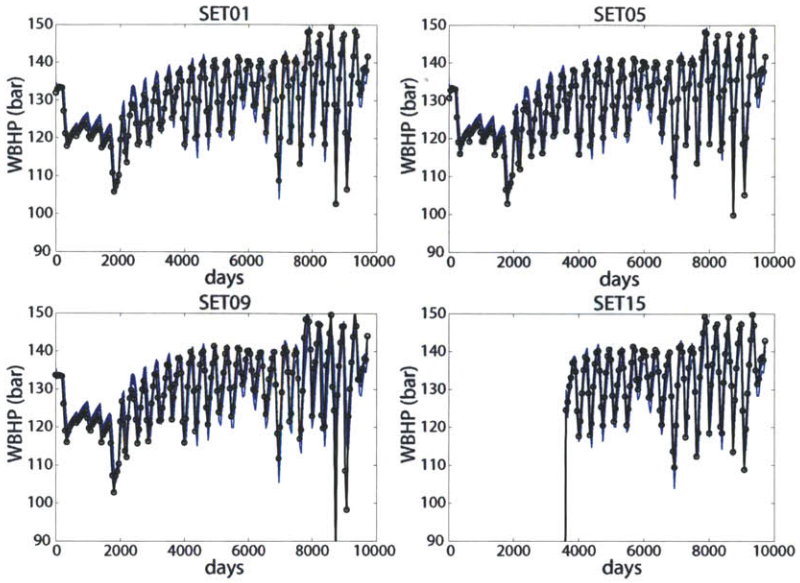

Figure 6-12: Excellent agreement between the Well Bottom Hole Pressure (WBHP) time series from the posterior predictions (blue lines) and from the history-matched run being treated as the measurement (black line with circles). Four wells are shown. There are one hundred prediction curves corresponding to the ensemble size of one hundred.

We again run the forward model simulations with one hundred realizations drawn from the posterior distributions to observe the agreement between the predicted and the measured WBHP and LOS displacements. Fig. 6-12 shows that the posterior prediction of the WBHP has, indeed, improved drastically as all the prediction curves cluster together around the measurement curve. Fig. 6-13 shows comparison between the measured displacement and displacements predicted by the posterior. The agreement between measured and predicted displacements is worse in the posterior than in the prior. This may further suggest that the displacements are weighted less than the pressures.

6.8 Discussion

We tested the geomechanical inversion methodology on the Lombardia dataset. Using the Ensemble Kalman Smoother (EnKS) as the estimator and our coupled flow and geomechanics simulator as the forward model, we have shown that it is possible to

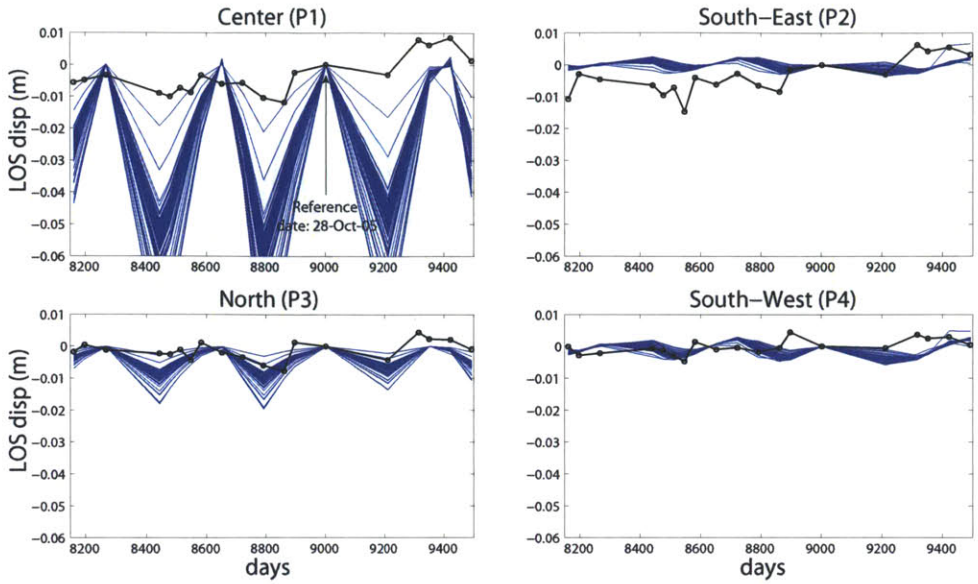

Figure 6-13: Comparison of the Line-Of-Sight (LOS) displacement time series from the posterior predictions (blue lines) and the Envisat satellite data (black line with circles) at four locations. The variability in the posterior predictions (spread of the blue curves) has decreased compared to the prior predictions (Fig. 6-8). However, the agreement between the measurement and the prediction has not improved significantly.

drastically reduce the uncertainty in the estimates of rock properties such as porosity, permeability, and compressibility. It may be possible to further improve the satellite data quality. In this study, we used data only from the ascending tracks of the Envisat. Descending track data looks similar. We can assess the impact of merging both the ascending and the descending tracks on inversion results. Also, there are two timeseries for the Envisat: (1) 06-Jul-03 to 25-Feb-07 timeseries with 19 timesteps, and (2) 05-Jun-05 to 25-Feb-07 timeseries with 13 timesteps. They were processed separately with different reference dates, 07-Nov-04 for the former and 03-Sept-06 for the latter. Compared to the timesteps in the first timeseries, there are 5 new and 8 repeat timesteps in the second timeseries. In this study we only used the first timeseries (after changing the reference timestep from 07-Nov-04 to 28-Oct-05 to better reflect the seasonal displacement profile). We did not merge the two series together, which will provide more data and potentially improve the inversion results.

Another avenue to explore is to use the TRE processed Radarsat data for the inversion exercise. It's coverage is smaller than Envisat but it has more PS stations

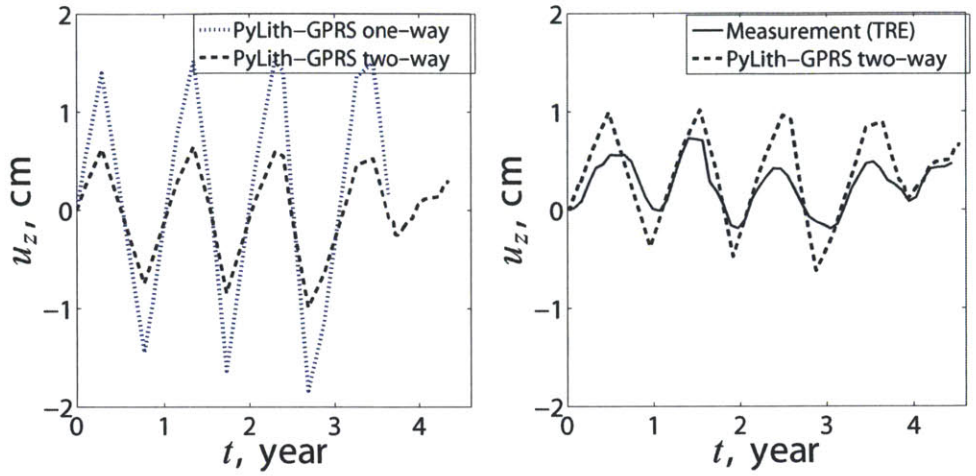

Figure 6-14: Comparison of the vertical displacement among the one-way coupled, the two-way coupled and the TRE processed data at one of the ground stations. The two-way coupled results are more accurate than the one-way coupled results, which neglect the coupling from the mechanics to the flow problem. The agreement between the two-way coupled results and the measurements is better.

around the wells and the data quality is smoother (displacement oscillates smoothly with the injection and production rates of well) as shown in Fig. 6-14. In the same figure, we also plot results from a two-way coupled simulation using rock properties of one of the realizations generated above. Notice that magnitude of the displacement is smaller in the two-way coupled case compared to the one-way coupled case due to the negative feedback from mechanics to flow.

Chapter 7

Coupled poromechanical analysis of the 2011 Lorca earthquake

7.1 Introduction

On 11 May 2011, a magnitude M_w 5.1 earthquake struck Lorca, a small city in southeast Spain (Fig. 7-1). The earthquake nucleated at a shallow depth of 3 to 5 km and caused significant damage in the city. The city is situated in the vicinity of a seismically active regional fault, the Alhama de Murcia Fault (AMF), which strikes south-west to north-east and dips north-west. The city is also close to an aquifer in the Alto Guadalentin basin in the south, which was used for extraction of water during 1960-2010. As a result of extensive pumping, the basin has experienced a very significant drop in water table, and accompanying subsidence. Based on analysis of the InSAR surface deformation data, modeling of slip on the AMF fault, and correlation between slip area and pattern of Coulomb stress change corresponding to crustal unloading due to water pumping, Gonzalez et al. [110] concluded that the earthquake was likely triggered by long-term pumping of water from the aquifer. They suggested that the drop in water table associated with groundwater pumping led to unloading of the rock close to the AMF fault, which resulted in additional compression on the fault bringing it closer to failure (Fig. 7-2).

The primary support for Gonzalez et al.'s claim comes from an estimation of

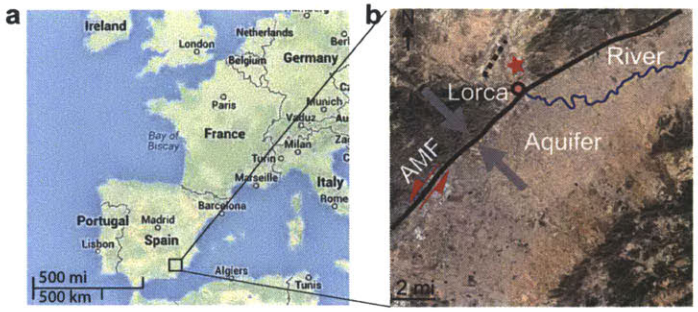

Figure 7-1: (a) Geographical location map of the Lorca city (from Google Maps). (b) Zoom-in view of a satellite image around Lorca (from Google Maps). The trace of the Alhama de Murcia Fault (AMF) is shown as a solid black line, with the maximum principal stress direction from tectonic compression on the fault shown as thick gray arrows. The Alto Guadalentin aquifer is on the south-east side of the fault and Lorca city is situated very close to the fault. The Guadalentin river is shown as a blue line. The red asterisk indicates the epicenter of the 2011 Lorca earthquake. The dash black line is the trace of an unmapped thrust plane in the region located from seismic analysis of the Lorca earthquake data [62].

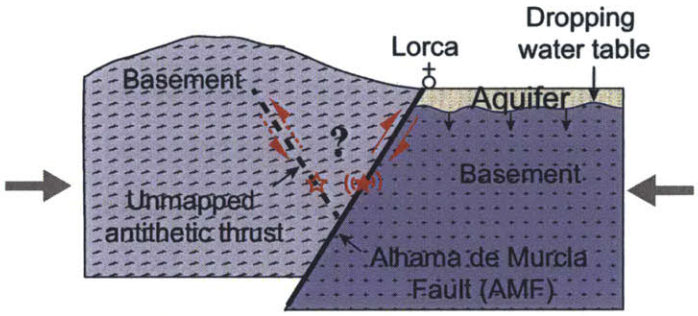

Figure 7-2: Conceptual model of the Lorca earthquake shown in a cross-section view (inspired from [12]). Crustal unloading due to groundwater extraction from the aquifer in the Alto Guadalentin basin led to rupture nucleation (red asterisk) on the nearby Alhama de Murcia Fault (AMF, solid black line), or possibly on an unmapped thrust plane (dash black line). The two fault planes correspond to conjugate nodal plane solutions of elastic dislocation model and surface deformation data, and the actual rupture plane is uncertain [62]. Slip motion is reverse with some left-lateral (AMF), or right-lateral component (the unmapped fault plane).

the change in cumulative Coulomb stress on the modeled fault plane due to crustal unloading [110], with positive values indicating favorable conditions for fault slip [20]. Gonzalez et al. show that the Coulomb stress change in their model is positive around the hypocentral region. However, Gonzalez et al. used elastic loading models [33, 172] to calculate the Coulomb stress change on a segment of the AMF under the assumption that pore pressure effects are unimportant for the timescales of interest.

Note that there is ambiguity regarding the geometry and position of the actual rupture plane associated with the earthquake. There are two equivalent conjugate nodal plane solutions from seismic analysis of the 2011 Lorca earthquake data–the northwest dipping plane and the southeast dipping plane [62]. Since the regional AMF fault system dips northwest, and there is no mapped fault in the region that dips southeast, previous analyses of the Lorca earthquake [110, 170] selected the northwest dipping plane as the earthquake-inducing fault. However, relocation of aftershocks at depth suggests that the aftershocks are oriented along a southeast plane. Therefore, the geometry and position of the actual rupture plane is uncertain. Elastic dislocation model and surface deformation data (InSAR and GPS) cannot resolve this uncertainty [62]. *Post mortem* analysis of earthquakes, and forecasting of earthquake triggering based on geodetic measurements such as InSAR and GPS, is an order-one problem in geophysics. However, determination of the rupture plane from conjugate nodal plane solutions, for a small (magnitude less than 6) and shallow earthquake such as the 2011 Lorca earthquake, is difficult because surface deformations for both nodal plane solutions are very similar.

In this Chapter, we investigate the role of fluid pressure in triggering of the Lorca earthquake and in resolving the uncertainty in location of the rupture plane. We use two different fault models based on two different nodal plane solutions proposed in [62]. Using a three-dimensional model of the Lorca region, we simulate groundwater withdrawal and subsequent unloading of the basin over the period of interest. Our coupled flow and geomechanics approach allows us to take a fresh look at this seismic event, which to-date has only been analyzed using simple elastic dislocation models and elastic loading solutions [110, 62].

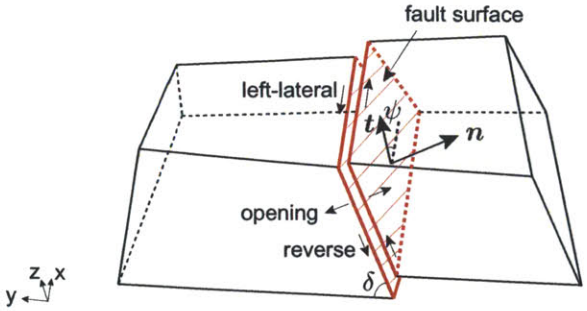

Figure 7-3: Schematic of a fault plane and fault slip. The fault plane is shown as striking along the x-axis. δ is the dip angle, and ψ is the rake angle. $\boldsymbol{n}$ and $\boldsymbol{t}$ are the normal and tangent vectors on the fault plane, respectively. Three components of fault slip motion in 3D are shown in terms of lateral, along-dip, and perpendicular-to-fault directions.

7.2 Pore pressure effects on fault slip

A large volume of water was extracted from the Alto Guadalentin aquifer during the period of 1960–2010 leading to an estimated $\Delta z_{\mathrm{wt}} = 250$ m drop in the water table. Ground level subsidence accompanying the pressure depletion is recorded at 2 m during the period 1990-2010 [110]. If we extrapolate at the subsidence rate of 10 cm/yr [109], total subsidence since 1960 could be higher, in the range of 3 to 5 m. Groundwater extraction leads to a decrease in the overburden (weight of overlying rock) acting on the basement as well as volumetric contraction of the aquifer. To calculate the effect of unloading on fault stability, due to decrease in the overburden, we evaluate the change in the Coulomb Failure Function, defined as

$$\Delta \mathrm{CFF} = \Delta\tau + \mu_f \Delta\sigma_n', \tag{7.1}$$

where $\Delta\tau$ is the change in shear traction, $\Delta\sigma_n' = \Delta\sigma_n + b\Delta p$ is the change in effective normal traction, and μ_f is the friction coefficient of the fault. In 3D, let δ and ψ be the fault dip angle and the slip-rake angle, respectively (Fig. 7-3). The fault normal vector is $\boldsymbol{n} = [0, -\sin\delta, \cos\delta]$, and the tangent vector is $\boldsymbol{t} = [\cos\psi, -\cos\delta\sin\psi, -\sin\delta\sin\psi]$. Assuming that the fault strikes along x-axis,

fault tractions are calculated from the Mohr-Coulomb theory as [133]

$$\begin{aligned}
\Delta\sigma_n &= \boldsymbol{n}^T \cdot \Delta\boldsymbol{\sigma} \cdot \boldsymbol{n} \\
&= (\Delta\sigma_{yy} \sin^2\delta + \Delta\sigma_{zz} \cos^2\delta) - \Delta\sigma_{yz} \sin 2\delta \\
\Delta\tau &= \boldsymbol{t}^T \cdot \Delta\boldsymbol{\sigma} \cdot \boldsymbol{n} \\
&= \cos\psi(\Delta\sigma_{xz} \cos\delta - \Delta\sigma_{xy} \sin\delta) + \left(\frac{1}{2}(\Delta\sigma_{yy} - \Delta\sigma_{zz}) \sin 2\delta - \Delta\sigma_{yz} \cos 2\delta\right) \sin\psi.
\end{aligned} \tag{7.2}$$

In the fault coordinate system (Fig. 7-3), the fault traction vector is $[\tau_1, \tau_2, \sigma_n]$, where τ_1 is the left-lateral component of the shear traction, and τ_2 is the up-dip component.

Equation (7.2) requires three inputs: changes in the total stress tensor, $\Delta\boldsymbol{\sigma}$, the fault geometry (δ, ψ), and changes in the pore pressure Δp. $\Delta\boldsymbol{\sigma}$ is calculated as a function of time using the rate of mass of water removed, $\phi\rho_w \dot{z}_{\text{wt}} A$, over an unloading area A. Gonzalez et al. assumed $\phi = 0.05$ and $\dot{z}_{\text{wt}} = 5$ m/year. They consider different shapes for the unloading area, e.g. a homogeneously loaded rectangle, a homogeneously loaded area bounded by a specific value of the subsidence contour, and an area bounded by a specific value of contour with load pattern proportional to the subsidence pattern (Fig. S11 in Supplementary Information of [110]). They used Love's solution [172] for the rectangular shapes, and convolution of Boussinesq's point source solution [33] for the irregular shapes. The important point to note here is that the stress field in the porous medium, $\boldsymbol{\sigma}$, is computed as the stress field in a purely elastic medium with no fluid or fluid pressure effect. This is also known as the decoupled approach for solving the stress field [216].

Gonzalez et al. used an elastic dislocation model [194] and inversion of the geodetic deformation data to estimate the best-fit fault geometry (70° NW dip, N230E strike, 36° rake of the slip). They also calculated slip on the fault using an inversion method.

Evaluation of ΔCFF on the fault requires evaluation of Δp in the neighborhood of the fault. Pumping of water from the aquifer leads to two kinds of changes in the pore pressure in the basement rock around the fault: drop in pressure due to expansion of pores under mechanical unloading, Δp_c, and drop in pressure due to leakage of water

from the basement to the aquifer, Δp_d. The former is related to the pressure drop under undrained conditions ($\zeta = 0$, Eq. (5.5)), i.e. $B\Delta\sigma_v$, where B is the Skempton coefficient and σ_v is the mean volumetric stress. The Skempton coefficient is defined as the ratio of induced change in pressure to change in mean stress under undrained conditions, $B = (\Delta p/\Delta\sigma_v)|_{\zeta=0}$, or equivalently as the ratio of volumetric strain to increment in fluid mass at constant mean stress, $B = (\varepsilon_v/\zeta)|_{\Delta\sigma_v=0}$ [267]. The latter pressure drop, Δp_d, can also be understood as diffusion of pressure drop from the aquifer to the basement, and it requires hydraulic communication between the two. Usually, the timescale for mechanical unloading is much smaller than the timescale for pressure diffusion due to high compressional wave speed and low hydraulic diffusivity in the basement. Such conditions favor undrained behavior during loading/unloading and lead to higher values of the Skempton coefficient.

Gonzalez et al. compute $\Delta p = \Delta p_c + \Delta p_d$ by solving the pressure diffusion equation for single-phase poromechanics

$$\frac{\partial}{\partial t}\left(\Delta p + B\Delta\sigma_v\right) - c\nabla^2(\Delta p) = 0, \tag{7.3}$$

which is Eq. (5.17) with external source $f = 0$ and the hydraulic diffusivity $c = (k/\mu)(K_{dr}B/b)$. Here, k is the basement permeability, μ is the fluid viscosity, and K_{dr} is the drained bulk modulus. Gonzalez et al. assume all rock and fluid properties to be constant in space and time. Assumed values of the aquifer diffusivity, $c = 0.1 - 10$ m^2/s, are high compared to reported values [43] of $0.02 - 0.04$ m^2/s. Assuming the decoupled approach, Gonzalez et al. use the analytical solution of Eq. (7.3) from [143] to calculate Δp at two points in the basement at a depth of 4 km (close to the hypocenter depth). Assuming $B = 0.6$ and $\mu_f = 0.5$, the authors show that ΔCFF varies between -10 kPa to 10 kPa over the fault plane with $\Delta\mathrm{CFF} \approx 5$ kPa near the hypocenter.

Gonzalez et al. claim that pore-pressure diffusion and coupled pore pressure changes are not relevant for the timescales of interest. This is based on the small values of Δp they calculated for the assumed diffusivity, and the small sensitivity of

Δp to variations in the Skempton coefficient. However, the ΔCFF values reported by Gonzalez et al. are in the range of kPa, orders of magnitude smaller than the stresses estimated to be released during the earthquake, as noted in [12]. The average static stress released during an earthquake can be estimated as $\overline{\Delta\sigma_s} = CM_0\tilde{L}^{-3}$ where C is a geometric constant of order unity, M_0 is the seismic moment, and $\tilde{L}$ is the characteristic rupture dimension [144]. Substituting $M_0 = 10^{1.5(M_w+6.07)}$ and $\tilde{L} = 3000$ m [110, 170], we obtain $\overline{\Delta\sigma_s} \approx 2$ MPa. In addition to the disparity in ΔCFF values on the AMF fault, there is some uncertainty as to which fault led to the earthquake, whether it is a segment from the AMF, or a blind thrust plane striking 5 km further NW from the AMF and dipping SE at 50° [62].

We test the assumptions made by Gonzalez et al. by simulating the *coupled* flow and deformation processes leading up to the Lorca earthquake. We build a 3D geomechanical model of the Lorca region and simulate groundwater extraction in the aquifer. We investigate the role of pore pressure in triggering of the Lorca earthquake, especially as it relates to the pumping of water from the aquifer. We also test the validity of the decoupled stress assumption by evaluating the sensitivity of ΔCFF to hydraulic diffusivity and porosity.

7.3 The Lorca simulation model

We construct two models of the Lorca region to simulate groundwater extraction and crustal unloading processes: Model 1 with the AMF fault surface dipping 54° to NW [110, 170], and Model 2 with an alternate plane dipping 50° to SE (Fig. 7-4). Both fault surfaces are obtained as conjugate nodal plane solutions during inversion of the InSAR Line-Of-Sight displacement data with elastic dislocation model. Model 2 fault plane also satisfies Lorca earthquake aftershock relocation [62]. Although this fault plane is currently unmapped in the region, the presence of SE dipping antithetic faults in the AMF splay system have been previously noted using geologic and paleoseismic data [180]. Using CUBIT, we construct a 20 km×16 km×10 km three-dimensional domain with x-axis parallel to the Lorca segment of the AMF fault. The

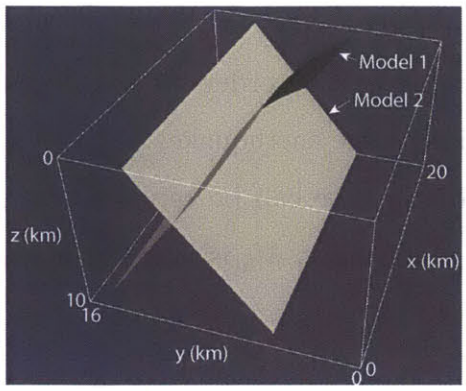

Figure 7-4: Two possible fault models for the Lorca earthquake.

Alto Guadalentin basin is south of the fault in both models. We follow [43] to model the geology and stratigraphy of the basin. The high-permeability detrital aquifer is 300-600 m thick and is underlain by low permeability strata. We use an unstructured grid to discretize the domain with very fine layering in the aquifer (10-20 m thick), and coarse layering (400-500 m thick) outside (Fig. 7-5). This allows us to model the drop in water table with time. The fault surface is truncated such that it does not intersect any of the four boundaries ($x+$, $x-$, $z+$, and $z-$). The flow domain is identical to the mechanics domain. We assume linear elastic mechanical response.

7.3.1 Model 1: Regional AMF fault

The fault surface in Model 1 bends to reflect the change in strike from the Lorca segment to the La Tercia segment of the AMF (Fig. 7-5). The aquifer is confined on the sides by the impermeable fault, $y-$, $x-$ and $x+$ boundaries. In the $z-$ direction it is confined through low permeability layers in the basement. We distribute rock properties such as the permeability k, the Young modulus E, and the drained bulk

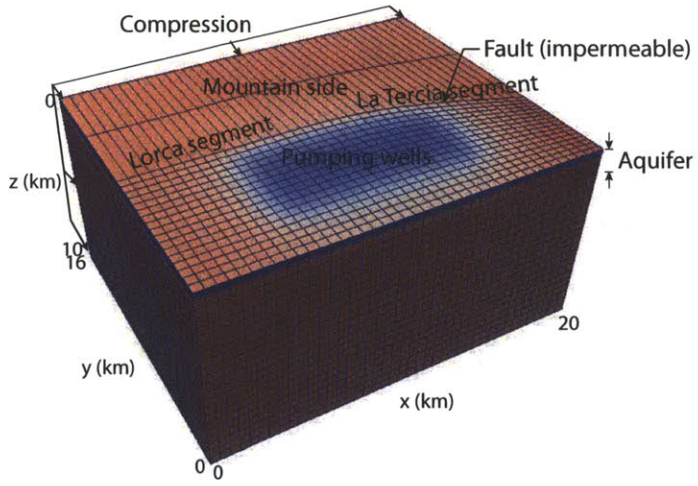

Figure 7-5: Geomechanical grid of the Lorca Model 1. The fault surface divides the domain into two sides: the basin side and the mountain side. Normal compression equal to twice the overburden, i.e. $2\sigma_{zz}$, is applied on the $y+$ boundary to simulate the pre-stress and compression on the fault. Water is extracted from the aquifer with wells located on the basin side. Rock permeability, which decreases with depth, is higher on the basin side than the mountain side.

modulus K_{dr} as per the following empirical relationships

$$\begin{aligned}
\phi &= \phi_r + (\phi_0 - \phi_r)\exp(-a_1 z) \\
k &= \max\left[k_r, k_0\left(\frac{\phi}{\phi_0}\right)^{a_2}\right] \\
E &= E_0 + \frac{3(1-2\nu)(1+\nu)}{(1-\nu)c_m} \\
\log_{10} c_m &= a_3 + a_4 \log_{10}(\sigma'_{\text{vert}}) \\
\sigma_{\text{vert}} &= z(a_5 + a_6 \ln z) \\
K_{dr} &= \frac{E}{3(1-2\nu)},
\end{aligned} \tag{7.4}$$

where subscript r denotes residual values ($\phi_r = 0.001, k_r = 0.0001$ mD), subscript 0 denotes surface values ($\phi_0 = 0.2$, $k_0 = 1000$ mD, $E_0 = 5$ GPa), $\nu = 0.25$ is the drained Poisson ratio, c_m is the uniaxial pore compressibility (bar^{-1}), z is depth (meter) positive downward, σ'_{vert} is the effective vertical stress (bar), σ_{vert} is the total vertical stress (bar), and $a_1 = 0.002, a_2 = 15, a_3 = -1.83, a_4 = 1.13, a_5 = 3270.8771, a_6 = 2415.588$ are the constants in the empirical relations. The empirical relations as a

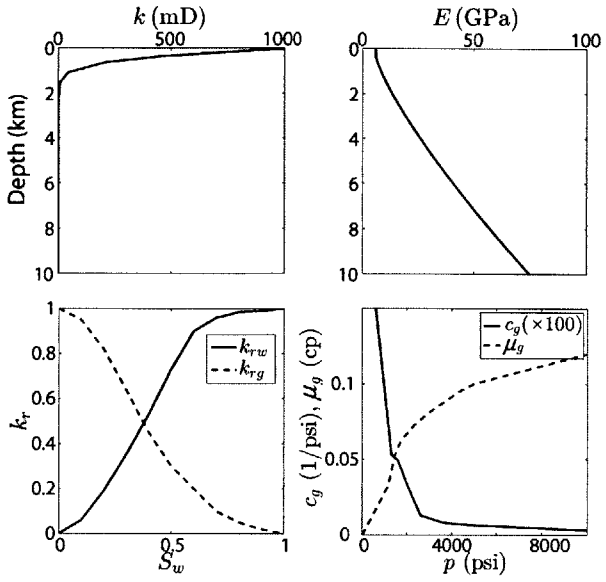

Figure 7-6: Top row: permeability k and the Young modulus E as a function of depth in Model 1. Values are calculated from empirical relations (Eq. (7.4)). On the mountain side of the fault (Fig. 7-5), the permeability is set to a constant low value of 0.0001 mD. Bottom row: relative permeabilities as a function of water saturation, and air compressibility and air viscosity as a function of pressure.

function of depth are taken from [128]. We use the porosity relation above only to compute permeability as a function of depth (Fig. 7-6), and fix the porosity in the flow simulation to 0.1.

We consider two-phase flow with air and water as the two phases and assume zero capillary pressure. The unknowns in the flow problem are the air pressure p_g and the water saturation S_w. The bulk density is given as $\rho_b = (1-\phi)\rho_s + \phi(S_w\rho_w + (1-S_w)\rho_g)$, where $\rho_s = 2600$ kg/m^3, $\rho_w = 1000$ kg/m^3, and $\rho_g = 0.76$ kg/m^3 are the solid, water and air densities, respectively. ρ_b is calculated with constant $\phi = 0.1$. As the water table drops and water in the pores is replaced with air, ρ_b decreases, which leads to crustal unloading. The mechanics problem is initialized with tectonic stresses that favor reverse faulting [180] (gray arrows in Fig. 7-1b): $\sigma_{zz} = -\int_0^z \rho_b g dz$, $\sigma_{yy} = 2\sigma_{zz}$, $\sigma_{xx} = 1.5\sigma_{zz}$, and zero shear stresses. With a static coefficient of friction $\mu_s = 0.47$ on the fault, these initial stresses result in fault tractions such that the fault is stable, albeit, close to failure. The initial displacement field is zero, $\boldsymbol{u}(t = 0) = \mathbf{0}$. The flow problem is initialized with the water table at $z = 0$, i.e., $S_w(t = 0) = 1$, and

hydrostatic pressure $p_g(t = 0) = p_w(t = 0) = \rho_w g z$. The mechanical boundary conditions are: normal compression on $y+$ side, i.e., $\sigma_n(y = 16\text{ km}) = \sigma_{yy}$, zero normal displacement on $x-$, $x+$, $y-$, and $z+$ boundaries, and zero traction on the $z-$ boundary. For the flow problem, no-flux boundary condition is imposed on all boundaries. To model the constant pressure open boundary at $z = 0$, we place 30 air injectors in the top layer operating under a maximum bottom hole pressure (BHP) constraint equal to the atmospheric pressure. This ensures that the aquifer pore space is filled with air as the water table drops. Water is extracted using 90 pumping wells placed at a uniform spacing and producing at a constant rate of 8000 barrel/day (14.7 kg/s) with minimum BHP constraint of 16 psi (110.32 kPa). Although rough estimate exist [110], actual production and rainfall data for the basin are not available.

Fig. 7-7 shows the pressure drop and the water saturation fields at $t = 50$ year. With this set of rock and fluid properties, the average water table depth drops by approximately 180 m, which is less than the expected value of 250 m. However, the maximum subsidence is only 0.35 m (Fig. 7-8), which is much smaller than the measurement value of 2 m. This discrepancy possibly indicates that the assumed values of the Young modulus near the surface are larger than the true values. We calculate ΔCFF to record the effect of pressure depletion on fault stability for Model 1. From Fig. 7-9, we observe that, for this fault geometry, ΔCFF is negative around the hypocenter depth suggesting that the fault actually becomes more stable as a result of the pressure depletion. Crustal unloading induces down-dip shear underneath the aquifer and higher compression on the fault (Fig. 7-10). This leads to a monotonic decline in ΔCFF. Further below, the change in the up-dip shear traction, $\Delta\tau_2$, switches sign leading to an increase in ΔCFF (Fig. 7-9b).

7.3.2 Model 2: Unmapped antithetic fault

This model is similar to Model 1 with the main difference being that we replace the AMF fault surface with an alternate fault plane, identified as a potential origin of the Lorca earthquake in [62] (Fig. 7-4). The fault plane located between $J = 14$ and $J = 15$, where J denotes the grid index along the y axis, strikes parallel to the Lorca

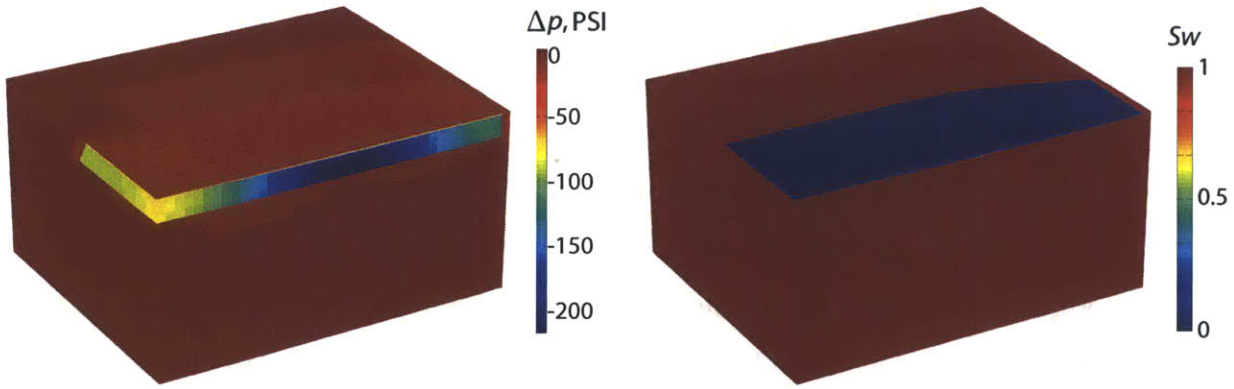

Figure 7-7: Overpressure and water saturation fields at $t = 50$ year in Model 1.

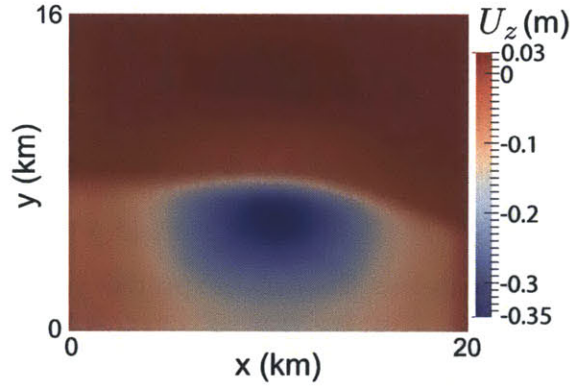

Figure 7-8: Vertical displacement field on ground surface for Model 1.

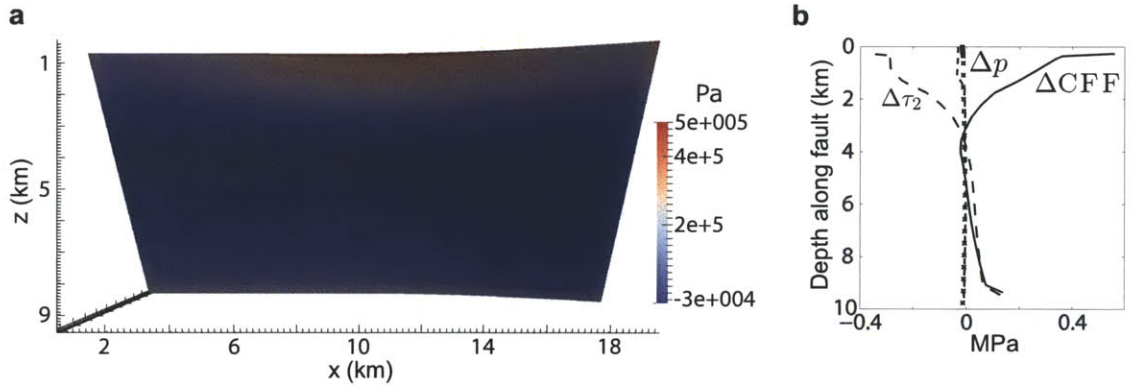

Figure 7-9: (a) Cumulative change in the Coulomb Failure Function, ΔCFF, on the AMF fault due to crustal unloading. (b) Depth profiles of changes in the Coulomb stress (solid line), pore pressure Δp (dash line for pressures on the aquifer side, crosses for pressures on the mountain side), and up-dip shear traction $\Delta\tau_2$ (long dash line) at $x = 10$ km. Results correspond to $t = 50$ year. For $z < 1$ km, the drop in pressure on the basin side is higher than that on the mountain side, due to the higher permeability on the basin side. Note that ΔCFF is negative below the base of the aquifer, i.e. around 3 km depth, suggesting frictional locking of the fault. This is in contrast with the positive ΔCFF estimated by Gonzalez et al. [110].

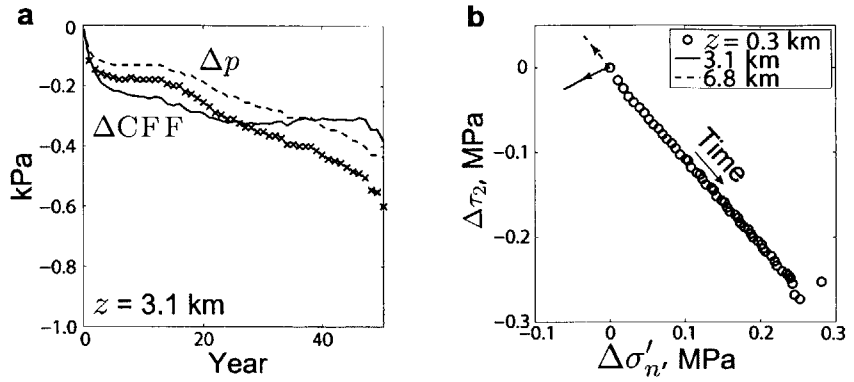

Figure 7-10: (a) Temporal evolution of changes in the Coulomb stress ΔCFF (solid line) and pore pressure Δp (dash line for the aquifer side, crosses for the mountain side) on the AMF fault at a point (9.96 km, 10.33 km, 3.1 km) in the hypocentral interval. (b) Evolution of change in the shear $\Delta\tau_2$ and effective normal $\Delta\sigma_n'$ fault tractions at three points on the fault: within the aquifer (0.3 km), below the aquifer around the hypocenter (3.1 km), and in the basement (6.8 km). $x = 9.96$ km. The arrows denote the direction of time from $t = 0$ to $t = 50$ year. At the hypocentral depth, the effective normal compression $-\sigma_n'$ increases, and the up-dip shear traction τ_2 decreases. This suggests stabilization of the fault at that depth.

segment of the AMF at a distance of approximately 5 km further NW and dips 50° to SE (Fig. 7-11). Similar to Model 1, the basin is confined in the $y+$ direction at approximately $y = 8$ km by applying a y-transmissibility multiplier of value 0.0001 to the faces shared by elements with $J = 9$ and $J = 10$ indices. This ensures that the fault is located on the mountain side, within the low permeability region. There are 70 pumping wells and 24 air injectors placed in a configuration similar to that of Model 1. We increase pumping rate for each well in four steps: 8000 bbl/d for $t \leq 13$ year, 12000 bbl/d for $13 < t \leq 26$ year, 16000 bbl/d for $26 < t \leq 46$ year, and 22000 bbl/d for $46 < t \leq 50$ year. Note that the conclusions do not change if we use a constant flow rate of 8000 bbl/d as in the case of Model 1. As the water table drops (Fig. 7-12), and water is replaced with air in the aquifer layers, the overburden on the basement rock decreases (crustal unloading), and there is negligible decline in the pore pressure of the basement rock because its permeability is very low. This results in expansion of the basement rock underneath the aquifer, which applies additional compression on the fault. Since the fault is dipping to SE, from Eq. (7.2), this results in up-dip shear on the fault (Fig. 7-14) and increase in ΔCFF between 3 to 5 km

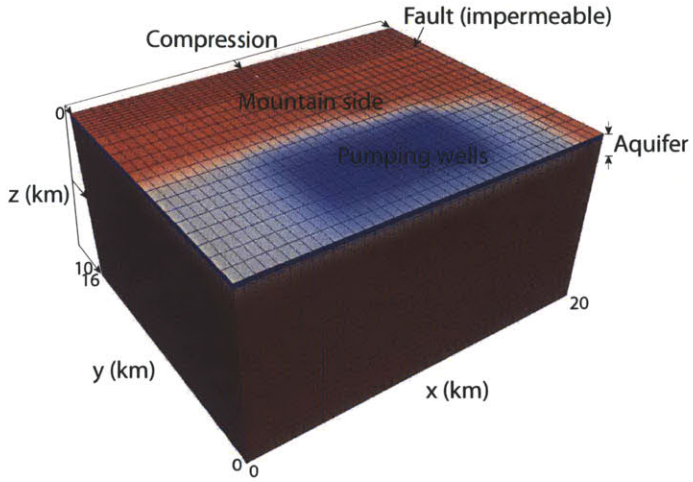

Figure 7-11: Geomechanical grid of the Lorca Model 2. The fault plane is entirely located in the low permeability mountain side region.

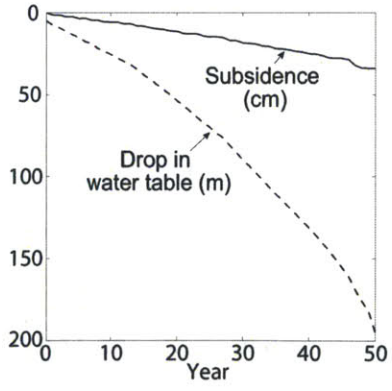

Figure 7-12: Temporal evolution of water table depth and ground subsidence in Model 2.

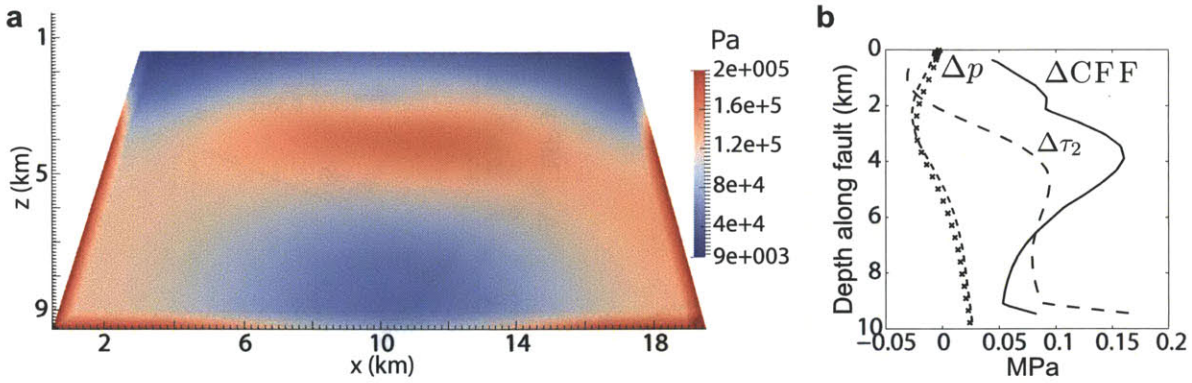

Figure 7-13: (a) Cumulative change in the Coulomb stress ΔCFF, on the antithetic fault due to crustal unloading. (b) Depth profiles of changes in the Coulomb stress (solid line), pore pressures Δp (dash line for the aquifer side, crosses for the mountain side), and up-dip shear traction $\Delta\tau_2$ (long dash line) at $x = 10$ km. Results are shown for $t = 50$ year. Note that ΔCFF is positive and with magnitude in the order of 100 kPa below the base of the aquifer, i.e. around 3 km depth, suggesting that the conditions are favorable for failure of the antithetic fault.

depth (Fig. 7-13). This suggests conditions favorable for fault slip.

7.4 Conclusions

While straightforward interpretation of the 2011 Lorca earthquake seismic data and regional (mapped) geology suggests that the earthquake nucleated on a segment of the NW-dipping AMF fault [110], relocation of aftershocks at depth agrees better with the conjugate nodal plane dipping SE [62]. Surface deformation data (InSAR and GPS), by itself, is unable to resolve which fault was the origin of the earthquake. In a previous modeling effort based on InSAR and GPS data in the Lorca region, and the elastic dislocation theory, it was concluded that the earthquake nucleated on a segment of the AMF fault [110]. However, that analysis neglected the role of pore pressure and the two-way coupling between groundwater extraction and mechanical deformation. The magnitude of the change in Coulomb stress associated with groundwater extraction calculated on the AMF fault is too small, and can not explain the stress drop accompanying the earthquake.

Here, we contend that a *coupled* analysis of flow and mechanics is required to

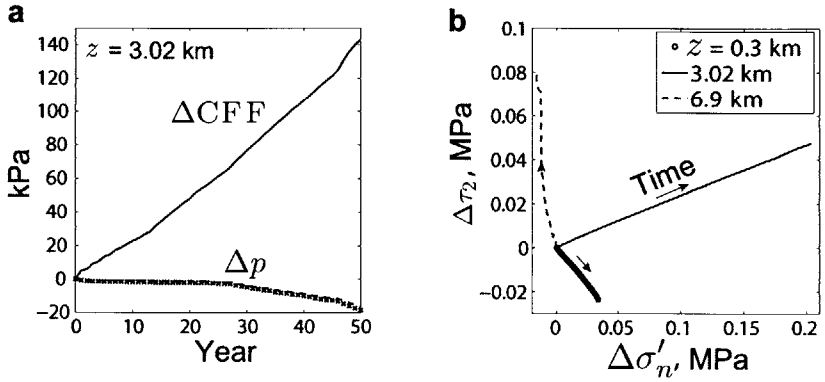

Figure 7-14: (a) Temporal evolution of changes in the Coulomb stress ΔCFF (solid line) and pore pressures Δp (dash line for the aquifer side, crosses for the mountain side) on the antithetic fault at a point (10 km, 10.47 km, 3.02 km) in the hypocentral interval. Notice the increase in the rate of decline in Δp at $t = 27$ and 46 years corresponding to increase in the water pumping rate. (b) Evolution of change in the fault tractions at three points on the fault: within the aquifer (0.3 km), below the aquifer around the hypocenter (3.02 km), and in the basement (6.9 km). $x = 10$ km. The arrows denote the direction of time from $t = 0$ to $t = 50$ year. At the hypocentral depth, in contrast to Model 1, the effective normal compression $-\sigma'_n$ decreases, and the up-dip shear traction τ_2 increases. This suggests destabilization of the fault and conditions favorable for up-dip slip at that depth.

identify the fault that ruptured during the 2011 Lorca earthquake. In our model, crustal unloading due to drop in the water table stabilizes a NW dipping fault, i.e. the AMF, in the hypocentral depth interval because the normal compression on the fault increases and the up-dip shear decreases. For a SE dipping antithetic fault, the trend reverses, and the fault is destabilized such that thrust faulting is favored. Moreover, the change in Coulomb stress on the antithetic fault is of the same order as that of the stress drop estimated to occur during the earthquake. Therefore, it appears that the 2011 Lorca earthquake was likely caused by rupture on a SE dipping unmapped fault, and we conclude that coupling of flow and mechanics is required to identify the earthquake-inducing fault.

Bibliography

[1] See http://juanesgroup.mit.edu/publications/mixfing for supplementary videos.

[2] B. Aagaard, S. Kientz, M. Knepley, S. Somala, L. Strand, and C. Williams. *PyLith User Manual version 1.8.0.* Computational Infrastructure for Geodynamics, 2011.

[3] B. Aagaard, C. Williams, and M. Knepley. PyLith: A finite-element code for modeling quasi-static and dynamic crustal deformation. *Eos Trans. AGU*, 89:T41A–1925, 2008.

[4] B. T. Aagaard, M. G. Knepley, and C. A. Williams. A domain decomposition approach to implementing fault slip in finite-element models of quasi-static and dynamic crustal deformation. *J. Geophys. Res.*, 118:3059–3079, 2013.

[5] I. Aavatsmark. An introduction to multipoint flux approximations for quadrilateral grids. *Comput. Geosci.*, 6:405–432, 2002.

[6] Y. Abousleiman, A. H.-D. Cheng, L. Cui, E. Detournay, and J.-C. Roegiers. Mandel's problem revisited. *Geotechnique*, 46:187–195, 1996.

[7] T. Ahmed, T. S. Shimizu, and R. Stocker. Microfluidics for bacterial chemotaxis. *Integr. Biol.*, 2:604–629, 2010.

[8] E. M. Anderson. *The Dynamics of Faulting and Dyke Formation With Application to Britain.* Oliver and Boyd, New York, 1951.

[9] F. Armero. Formulation and finite element implementation of a multiplicative model of coupled poro-plasticity at finite strains under fully saturated conditions. *Comput. Meth. Appl. Mech. Eng.*, 171:205–241, 1999.

[10] F. Armero and J. C. Simo. A new unconditionally stable fractional step method for non-linear coupled thermomechanical problems. *Int. J. Numer. Meth. Eng.*, 35:737–766, 1992.

[11] F. Armero and J. C. Simo. A priori stability estimates and unconditionally stable product formula algorithms for nonlinear coupled thermoplasticity. *Int. J. Plasticity*, 9:749–782, 1993.

[12] J. Avouac. Human-induced shaking. *Nat. Geosci.*, 5:763–764, 2012.

[13] K. Aziz and A. Settari. *Petroleum Reservoir Simulation.* Elsevier, London, 1979.

[14] J. C. Bacri, N. Rakotomalala, D. Salin, and R. Woumeni. Miscible viscous fingering: Experiments versus continuum approach. *Phys. Fluids*, 4:1611, 1992.

[15] S. Balay, W. D. Gropp, L. C. McInnes, and B. F. Smith. Efficient management of parallelism in object-oriented numerical software libraries. In *Modern Software Tools in Scientific Computing*, pages 163–202. Birkhauser Press, 1997.

[16] J. Baldyga, R. Czarnocki, B. Y. Shekunov, and K. B. Smith. Particle formation in supercritical fluids: scale-up problem. *Chem. Eng. Res. Des.*, 88:331, 2010.

[17] F. Balsamo and F. Storti. Size-dependent comminution, tectonic mixing, and sealing behavior of a structurally oversimplified fault zone in poorly lithified sands: Evidence for a coseismic rupture? *Geo. Soc. Am. Bull.*, 123:601–619, 2011.

[18] J. Bear. *Dynamics of Fluids in Porous Media.* Wiley, New York, 1972.

[19] J. Bear and M. Y. Corapcioglu. Mathematical model for regional land subsidence due to water pumping. *Water Resour. Res.*, 17:937–958, 1981.

[20] N. M. Beeler, R. W. Simpson, S. H. Hickman, and D. A. Lockner. Pore fluid pressure, apparent friction, and Coulomb failure. *J. Geophys. Res.*, 105:25533–25542, 2000.

[21] G. Beer. An isoparametric joint/interface element for finite element analysis. *Int. J. Numer. Meth. Eng.*, 21:585–600, 1985.

[22] D. Bensimon, L. P. Kadanoff, S. Liang, B. I. Shraiman, and C. Tang. Viscous flow in two dimensions. *Rev. Mod. Phys.*, 58:977–999, 1986.

[23] K. R. Bhaskar et al. Viscous fingering of HCl through gastric mucin. *Nature*, 360:458–461, 1992.

[24] M. A. Biot. General theory of three-dimensional consolidation. *J. Appl. Phys.*, 12:155–164, 1941.

[25] J. T. Birkholzer and Q. Zhou. Basin–scale hydrogeologic impacts of CO_2 storage: Capacity and regulatory implications. *Int. J. Greenh. Gas Control*, 3:745–756, 2009.

[26] A. W. Bishop. The principle of effective stress. *Tekniske Ukeblad*, 39:859–863, 1959.

[27] A. W. Bishop and G. E. Blight. Some aspects of effective stress in saturated and partly saturated soils. *Geotechnique*, 13:177–197, 1963.

[28] R. J. Blackwell, J. R. Rayne, and W. M. Terry. Factors influencing the efficiency of miscible displacements. *Petrol. Trans.* AIME, 217:1–8, 1959.

[29] M. Blunt and M. Christie. How to predict viscous fingering in three component flow. *Transp. Porous Media*, 12:207–236, 1993.

[30] M. Blunt and M. Christie. Theory of viscous fingering in two phase, three component flow. *SPE Advanced Technology Series*, 2(2):52–60, 1994.

[31] G. Boffetta, F. De Lillo, and S. Musacchio. Nonlinear diffusion model for Rayleigh-Taylor mixing. *Phys. Rev. Lett.*, 104:034505, 2010.

[32] D. Bolster, F. J. Valdes-Parada, T. Le Borgne, M. Dentz, and J. Carrera. Mixing in confined stratified aquifers. *J. Contam. Hydrol.*, 120–121:198–212, 2011.

[33] J. Boussinesq. Application des potentiels a l'etude de l'equilibre et du mouvement des solides elastiques. *Reprint Paris: Blanchard, 1969*, 1885.

[34] H. Brezis. *Functional Analysis, Sobolev Spaces and Partial Differential Equations.* Springer, New York, 2011.

[35] E. E. Brodsky and L. J. Lajoie. Anthropogenic seismicity rates and operational parameters at the Salton Sea Geothermal Field. *Science*, 341:543–546, 2013.

[36] R. H. Brooks and A. T. Corey. Hydraulic properties of porous media. *Hydrological Papers (Colorado State University)*, 3:892–898, 1964.

[37] J. S. Caine and C. B. Forster. *Faults and Subsurface Fluid Flow in the Shallow Crust,* W. C. Haneberg et al. (eds.). Am. Geophys. Union, Geophys. Mono. Series, Vol. 113, 1999.

[38] H. Cao. *Development of Techniques for General Purpose Simulators.* PhD thesis, Stanford University, 2002.

[39] F. Cappa and J. Rutqvist. Impact of CO_2 geological sequestration on the nucleation of earthquakes. *Geophys. Res. Lett.*, 38:L17313, 2011.

[40] F. Cappa and J. Rutqvist. Modeling of coupled deformation and permeability evolution during fault reactivation induced by deep underground injection of CO_2. *Int. J. Greenh. Gas Control*, 5:336–346, 2011.

[41] D. S. Carder. Seismic investigations in the Boulder Dam area, 1940–1944, and the influence of reservoir loading on earthquake activity. *Bull. Seismol. Soc. Am.*, 35:175–192, 1945.

[42] R. D. Carter and G. W. Tracy. An improved method for calculating water influx. *Petrol. Trans., AIME*, 219:415–417, 1960.

[43] J. Ceron and A. Pulido-Bosch. Groundwater problems resulting from co_2 pollution and overexploitation in Alto Guadalentn aquifer (Murcia, Spain). *Environ. Geol.*, 28:223–228, 1996.

[44] C.-Y. Chen, C.-W. Huang, H. Gadêlha, and J. A. Miranda. Radial viscous fingering in miscible Hele-Shaw flows: A numerical study. *Phys. Rev. E*, 78:016306, 2008.

[45] C. Y. Chen and E. Meiburg. Miscible porous media displacements in the quarter five-spot configuration. Part 1. The homogeneous case. *J. Fluid Mech.*, 371:233–268, 1998.

[46] C. Y. Chen and E. Meiburg. Miscible porous media displacements in the quarter five-spot configuration. Part 2. Effect of heterogeneities. *J. Fluid Mech.*, 371:269–299, 1998.

[47] C.-Y. Chen, L. Wang, and E. Meiburg. Miscible droplets in a porous medium and the effects of Korteweg stresses. *Phys. Fluids*, 13:2447–2456, 2001.

[48] L. Chiaramonte, M. D. Zoback, J. Friedmann, and V. Stamp. Seal integrity and feasibility of CO_2 sequestration in the Teapot Dome EOR pilot: geomechanical site characterization. *Environ. Geol.*, 54(8):1667–1675, 2008.

[49] M. A. Christie. High-resolution simulation of unstable flows in porous media. *SPE Reserv. Eng.*, 4:297–303, August 1989.

[50] M. A. Christie and D. J. Bond. Detailed simulation of unstable processes in miscible flooding. *SPE Reserv. Eng.*, 2:514–522, November 1987.

[51] J. T. Coleman and D. Sinton. A sequential injection microfluidic mixing strategy. *Microfluid. Nanofluid.*, 1:319, 2005.

[52] O. Coussy. *Mechanics of Porous Continua.* John Wiley and Sons, Chichester, England, 1995.

[53] O. Coussy. *Poromechanics.* John Wiley and Sons, Chichester, England, 2004.

[54] O. Coussy. Poromechanics of freezing materials. *J. Mech. Phys. Solids*, 53:1689–1718, 2005.

[55] O. Coussy, P. Dangla, T. Lassabatére, and V. Baroghel-Bouny. The equivalent pore pressure and the swelling and shrinkage of cement-based materials. *Mater. Struct. Concrete Sci. Eng.*, 37:15–20, 2004.

[56] O. Coussy, R. Eymard, and T. Lassabatére. Constitutive modeling of unsaturated drying deformable materials. *J. Eng. Mech.*, 124(6):658–557, 1998.

[57] CUBIT. *Cubit 13.2 User Documentation.* Sandia National Laboratories, 2013.

[58] L. Cueto-Felgueroso and R. Juanes. Forecasting long-term gas production from shale. *Proc. Natl. Acad. Sci. U.S.A.*, 110:19660–19661, 2013.

[59] P. J. Cullen. *Food Mixing: Principles and Applications.* Wiley, 2009.

[60] C. M. Dafermos. *Hyperbolic Conservation Laws in Continuum Physics.* Springer-Verlag, Berlin, 2000.

[61] L. P. Dake. *Fundamentals of Reservoir Engineering.* Elsevier, Oxford, 1978.

[62] M. de Michele, P. Briole, D. Raucoules, A. Lemoine, and A. Rigo. Revisiting the shallow Mw 5.1 Lorca earthquake (southeastern Spain) using C-band InSAR and elastic dislocation modelling. *Remote Sens. Lett.*, 4:863–872, 2013.

[63] A. De Wit. Fingering of chemical fronts in porous media. *Phys. Rev. Lett.*, 87:054502, 2001.

[64] A. De Wit, Y. Bertho, and M. Martin. Viscous fingering of miscible slices. *Phys. Fluids*, 17:054114, 2005.

[65] A. De Wit and G. M. Homsy. Viscous fingering in periodically heterogeneous porous media. I. Formulation and linear instability. *J. Chem. Phys.*, 107:9609–9618, 1997.

[66] A. De Wit and G. M. Homsy. Viscous fingering in periodically heterogeneous porous media. II. Numerical simulations. *J. Chem. Phys.*, 107:9619–9628, 1997.

[67] A. De Wit and G. M. Homsy. Viscous fingering in reaction-diffusion systems. *J. Chem. Phys.*, 110:8663–8675, 1999.

[68] R. H. Dean, X. Gai, C. M. Stone, and S. E. Minkoff. A comparison of techniques for coupling porous flow and geomechanics. *Soc. Pet. Eng. J.*, 11:132–140, 2006.

[69] M. Dentz, T. Le Borgne, A. Englert, and B. Bijeljic. Mixing, spreading and reaction in heterogeneous media: A brief review. *J. Contam. Hydrol.*, 120–121:1–17, 2011.

[70] J. H. Dieterich. Constitutive properties of faults with simulated gouge. pages 108–120.

[71] J. H. Dieterich. Modeling of rock friction, 1. Experimental results and constitutive equations. *J. Geophys. Res.*, 84:2161–2168, 1979.

[72] D. Dreger and B. Woods. Regional distance seismic moment tensors of nuclear explosions. *Tectonophysics*, 356:139–156, 2002.

[73] D. A. Dunn and I. Feygin. Challenges and solutions to ultra-high-throughput screening assay miniaturization: submicroliter fluid handling. *Drug Discov. Today*, 5:84, 2000.

[74] W. L. Ellsworth. Injection-induced earthquakes. *Science*, 341:1–7, 2013.

[75] A. A. Emerick and A. C. Reynolds. Ensemble smoother with multiple data assimilation. *Comput. Geosci.*, 55:3–15, 2013.

[76] T. Engelder. Capillary tension and imbibition sequester frack fluid in Marcellus gas shale. *Proc. Natl. Acad. Sci. U.S.A.*, 109(52):E3625, 2012.

[77] V. Eswaran and S. B. Pope. Direct numerical simulations of the turbulent mixing of a passive scalar. *Phys. Fluids*, 31:506, 1988.

[78] G. Evensen. The ensemble Kalman filter: Theoretical formulation and practical implementation. *Ocean Dynamics*, 53:343–367, 2003.

[79] G. Evensen. Sampling strategies and square root analysis schemes for the EnKF. *Ocean Dynamics*, 54:539–560, 2004.

[80] G. Evensen. *Data assimilation: The ensemble Kalman filter.* Springer, Berlin, 2007.

[81] F. M. Orr and J. J. Taber. Use of carbon dioxide in enhanced oil recovery. *Science*, 224:563–569, 1984.

[82] F. J. Fayers. An approximate model with physically interpretable parameters for representing viscous fingering. *SPE Reserv. Eng.*, 3:551–558, 1988.

[83] F. J. Fayers, M. J. Blunt, and M. A. Christie. Comparison of empirical viscous-fingering models and their calibration for heterogeneous problems. *SPE Reserv. Eng.*, 7:195–203, May 1992.

[84] F. J. Fayers, F. Jouaux, and H. A. Tchelepi. An improved macroscopic model for viscous fingering and its validation for 2D and 3D flows—I. Non-gravity flows. *In Situ*, 18:43–78, 1994.

[85] K. L. Feigl, D. C. Agnew, Y. Bock, D. Dong, A. Donnellan, B. H. Hager, T. A. Herring, D. D. Jackson, T. H. Jordan, R. W. King, S. Larsen, K. M. Larson, M. H. Murray, Z. K. Shen, and F. H. Webb. Space geodetic measurement of crustal deformation in central and southern California, 1984–1992. *J. Geophys. Res.*, 98:21677–21712, 1993.

[86] C. A. Felippa and K. C. Park. Staggered transient analysis procedures for coupled mechanical systems: Formulation. *Comput. Meth. Appl. Mech. Eng.*, 24:61–111, 1980.

[87] E. J. Fernandez, T. Tucker Norton, W. C. Jung, and J. G. Tsavalas. A column design for reducing viscous fingering in size exclusion chromatography. *Biotechnol. Prog.*, 12:480, 1996.

[88] J. Fernandez and G. M. Homsy. Viscous fingering with chemical reaction: effect of *in-situ* production of surfactants. *J. Fluid Mech.*, 480:75, 2003.

[89] J. Fernandez, P. Kurowski, P. Petitjeans, and E. Meiburg. Density-driven unstable flows of miscible fluids in a Hele-Shaw cell. *J. Fluid Mech.*, 451:239, 2002.

[90] M. Ferronato, N. Castelletto, and G. Gambolati. A fully coupled 3-D mixed finite element model of Biot consolidation. *J. Comput. Phys.*, 229(12):4813–4830, 2010.

[91] M. Ferronato, G. Gambolati, C. Janna, and P. Teatini. Numerical modeling of regional faults in land subsidence prediction above gas/oil reservoirs. *Int. J. Numer. Anal. Methods Geomech.*, 32:633–657, 2008.

[92] M. J. Fetkovich. A simplified approach to water influx calculations—Finite aquifer systems. *J. Pet. Technol.*, 23:814–828, 1971.

[93] Y. Fialko and M. Simons. Deformation and seismicity in the Coso geothermal area, Inyo County, California: Observations and modeling using satellite radar interferometry. *J. Geophys. Res.*, 105:781–794, 2000.

[94] J. B. Fletcher and L. R. Sykes. Earthquakes related to hydraulic mining and natural seismic activity in western New York State. *J. Geophys. Res.*, 82:3767–3780, 1977.

[95] F. J. T. Floris, M. D. Bush, M. Cuypers, F. Roggero, and A-R. Syversveen. Methods for quantifying the uncertainty of production forecasts: A comparative study. *Pet. Geosci.*, 7:87–96, 2001.

[96] C. Frohlich, C. Hayward, B. Stump, and E. Potter. The Dallas-Fort Worth earthquake sequence: October 2008–May 2009. *Bull. Seismol. Soc. Am.*, 101:327–340, 2010.

[97] T. Frommelt et al. Microfluidic mixing via acoustically driven chaotic advection. *Phys. Rev. Lett.*, 100:034502, 2008.

[98] D. L. Galloway and T. J. Burbey. Review: Regional land subsidence accompanying groundwater extraction. *Hydrogeol. J.*, 19:1459–1486, 2011.

[99] D. L. Galloway, K. W. Hudnut, S. E. Ingebritsen, S. P. Phillips, G. Peltzer, F. Rogez, and P. A. Rosen. Detection of aquifer system compaction and land subsidence using interferometric synthetic aperture radar, Antelope Valley, Mojave Desert, California. *Water Resour. Res.*, 34:2573–2585, 1998.

[100] G. Gambolati and R. A. Freeze. Mathematical simulation of the subsidence of Venice, 1, Theory. *Water Resour. Res.*, 9:721–733, 1973.

[101] G. Gambolati, P. Teatini, D. Bau, and M. Ferronato. The importance of poroelastic coupling in dynamically active aquifers of the Po river basin, Italy. *Water Resour. Res.*, 36:2443–2459, 2000.

[102] P. Garstecki, M. J. Fuerstman, M. A. Fischbach, S. K. Sia, and G. M. Whitesides. Mixing with bubbles: a practical technology for use with portable microfluidic devices. *Lab Chip*, 6:207–212, 2006.

[103] J. Geertsma. The effect of fluid pressure decline on volumetric change of porous rocks. *Trans. AIME*, 210:331–340, 1957.

[104] J. Geertsma. A basic theory of subsidence due to reservoir compaction: The homogeneous case. *Verhandelingen Kon. Ned. Geol. Mijnbouwk. Gen.*, 28:43–62, 1973.

[105] J. Geertsma and G. Van Opstal. A numerical technique for predicting subsidence above compacting reservoirs based on the nucleus of strain concept. *Verhandelingen Kon. Ned. Geol. Mijnbouwk. Gen.*, 28:63–78, 1973.

[106] I. Glasgow and N. Aubry. Enhancement of microfluidic mixing using time pulsing. *Lab Chip*, 3:114–120, 2003.

[107] I. Glasgow and N. Aubry. Electroosmotic mixing in microchannels. *Lab Chip*, 4:558–562, 2004.

[108] R. Glowinsky and P. Le Tallec. *Augmented Lagrangian and Operator-Splitting Methods in Nonlinear Mechanics*. SIAM, Philadelphia, PA, 1989.

[109] P. J. Gonzalez and J. Fernandez. Drought-driven transient aquifer compaction imaged using multitemporal satellite radar interferometry. *Geology*, 39:551–554, 2011.

[110] P. J. Gonzalez, K. F. Tiampo, M. Palano, F. Cannavo, and J. Fernandez. The 2011 Lorca earthquake slip distribution controlled by groundwater crustal unloading. *Nat. Geosci.*, 5:821–825, 2012.

[111] R. E. Goodman, R. L. Taylor, and T. L. Brekke. A model for the mechanics of jointed rock. *J. Soil Mech.*, 94:637–659, 1968.

[112] W. G. Gray and B. A. Schrefler. Thermodynamic approach to effective stress in partially saturated porous media. *Eur. J. Mech.-A*, 20:521–538, 2001.

[113] D. W. Green and G. P. Willhite. *Enhanced Oil Recovery*. SPE Textbook Series, Vol. 6, 1998.

[114] D. Gunasekera, P. Childs, J. Herring, and J. Cox. A multi-point flux discretization scheme for general polyhedral grids. In *6th SPE International Oil and Gas Conference and Exhibition*, number SPE 48855, Beijing, 1998.

[115] H. K. Gupta. *Reservoir-Induced Earthquakes*. Elsevier, Amsterdam, 1992.

[116] H. K. Gupta. A review of recent studies of triggered earthquakes by artificial water reservoirs with special emphasis on earthquakes in Koyna, India. *Earth-Sci. Rev.*, 58:279–310, 2002.

[117] B. Habermann. The efficiency of miscible displacement as a function of mobility ratio. *Petrol. Trans.* AIME, 219:264–272, 1960.

[118] B. H. Hager, R. W. King, and M. H. Murray. Measurement of crustal deformation using the Global Positioning System. *Annu. Rev. Earth Planet. Sci.*, 19:351–382, 1991.

[119] N. Halko, P. G. Martinsson, and J. A. Tropp. Finding structure with randomness: Probabilistic algorithms for constructing approximate matrix decompositions. *SIAM Rev.*, 53:217–288, 2011.

[120] O. Hallatschek and D. R. Nelson. Population genetics and range expansions. *Phys. Today*, 62(7):42–47, 2009.

[121] T. C. Hanks and H. Kanamori. A moment magnitude scale. *J. Geophys. Res.*, 84:2348–2350, 1979.

[122] M. Hashimoto, P. Garstecki, H. A. Stone, and G. M. Whitesides. Interfacial instabilities in a microfluidic Hele-Shaw cell. *Soft Matter*, 4:1403–1413, 2008.

[123] Y. Hatwalne, S. Ramaswamy, M. Rao, and R. A. Simha. Rheology of active-particle suspensions. *Phys. Rev. Lett.*, 92:118101, 2004.

[124] J. J. Hidalgo, J. Fe, L. Cueto-Felgueroso, and R. Juanes. Scaling of convective mixing in porous media. *Phys. Rev. Lett.*, 109:264503, 2012.

[125] G. M. Homsy. Viscous fingering in porous media. *Ann. Rev. Fluid Mech.*, 19:271–311, 1987.

[126] R. W. Howarth, R. Santoro, and A. Ingraffea. Methane and the greenhouse-gas footprint of natural gas from shale formations. *Climatic Change*, 106:679–690, 2011.

[127] M. K. Hubbert and W. W. Rubey. Role of fluid pressure in mechanics of overthrust faulting I. Mechanics of fluid-filled porous solids and its application to overthrust faulting. *Geol. Soc. Am.*, 70:115–166, 1959.

[128] T. Hueckel, G. Cassiani, J. H. Prevost, and D. A. Walters. Field derived compressibility of deep sediments of the northern adriatic. *Land Subsidence, Special Volume, Proc. 7th Int. Symp. on Land Subsidence*, 2005.

[129] T. J. R. Hughes. *The Finite Element Method: Linear Static and Dynamic Finite Element Analysis.* Prentice-Hall, Englewood Cliffs, NJ, 1987.

[130] IPCC. *Special Report on Carbon Dioxide Capture and Storage,* B. Metz et al. (eds.). Cambridge University Press, 2005.

[131] T. Ishikawa, N. Yoshida, H. Ueno, M. Wiedeman, Y. Imai, and T. Yamaguchi. Energy transport in a concentrated suspension of bacteria. *Phys. Rev. Lett.*, 107:028102, 2011.

[132] R. B. Jackson, A. Vengosh, T. H. Darrah, N. R. Warner, A. Down, R. J. Poreda, S. G. Osborn, K. Zhao, and J. D. Karr. Increased stray gas abundance in a subset of drinking water wells near Marcellus shale gas extraction. *Proc. Natl. Acad. Sci. U.S.A.*, 110(28):11250–11255, 2013.

[133] J. C. Jaeger and N. G. W. Cook. *Fundamentals of Rock Mechanics*. Chapman and Hall, London, 1979.

[134] L. Jean, M. Mainguy, R. Masson, and S. Vidal-Gilbert. Accelerating the convergence of coupled geomechanical-reservoir simulations. *Int. J. Numer. Anal. Methods Geomech.*, 31:1163–1181, 2007.

[135] B. Jha, L. Cueto-Felgueroso, and R. Juanes. Fluid mixing from viscous fingering. *Phys. Rev. Lett.*, 106:194502, 2011.

[136] B. Jha, L. Cueto-Felgueroso, and R. Juanes. Quantifying mixing in viscously unstable porous media flows. *Phys. Rev. E*, 84:066312, 2011.

[137] B. Jha, L. Cueto-Felgueroso, and R. Juanes. Synergetic fluid mixing from viscous fingering and alternating injection. *Phys. Rev. Lett.*, 111:144501, 2013.

[138] B. Jha and R. Juanes. A locally conservative finite element framework for the simulation of coupled flow and reservoir geomechanics. *Acta Geotech.*, 2:139–153, 2007.

[139] R. Juanes and M. J. Blunt. Analytical solutions to multiphase first-contact miscible models with viscous fingering. *Transp. Porous Media*, 64(3):339–373, 2006.

[140] R. Juanes and M. J. Blunt. Impact of viscous fingering on the prediction of optimum WAG ratio. *Soc. Pet. Eng. J.*, 12(4):486–495, 2007.

[141] R. Juanes, B. H. Hager, and H. J. Herzog. No geologic evidence that seismicity causes fault leakage that would render large-scale carbon capture and storage unsuccessful. *Proc. Natl. Acad. Sci. U.S.A.*, 109(52):E3623, 2012.

[142] R. Juanes, E. J. Spiteri, F. M. Orr, Jr., and M. J. Blunt. Impact of relative permeability hysteresis on geological CO_2 storage. *Water Resour. Res.*, 42:W12418, 2006.

[143] Kalpna and R. Chander. Greens function based stress diffusion solutions in the porous elastic half space for time varying finite reservoir loads. *Phys. Earth Planet. In.*, 120:93–101, 2000.

[144] H. Kanamori and E. E. Brodsky. The physics of earthquakes. *Rep. Prog. Phys.*, 67:1429–1496, 2004.

[145] K. M. Keranen, H. M. Savage, G. A. Abers, and E. S. Cochran. Potentially induced earthquakes in Oklahoma, USA: Links between wastewater injection and the 2011 M_w 5.7 earthquake sequence. *Geology*, 41:699–702, 2013.

[146] N. Khalili, F. Geiser, and G. E. Blight. Effective stress in unsaturated soils, a review with new evidence. *Int. J. Geomech.*, 4:115–126, 2004.

[147] J. Kim, H. A. Tchelepi, and R. Juanes. Stability, accuracy and efficiency of sequential methods for coupled flow and geomechanics. *Soc. Pet. Eng. J.*, 16(2):249–262, 2011.

[148] J. Kim, H. A. Tchelepi, and R. Juanes. Stability and convergence of sequential methods for coupled flow and geomechanics: Drained and undrained splits. *Comput. Meth. Appl. Mech. Eng.*, 200:2094–2116, 2011.

[149] J. Kim, H. A. Tchelepi, and R. Juanes. Stability and convergence of sequential methods for coupled flow and geomechanics: Fixed-stress and fixed-strain splits. *Comput. Meth. Appl. Mech. Eng.*, 200:1591–1606, 2011.

[150] J. Kim, H. A. Tchelepi, and R. Juanes. Rigorous coupling of geomechanics and multiphase flow with strong capillarity. *Soc. Pet. Eng. J.*, 18:1123–1139, 2013.

[151] A. R. Kopf-Sill and G. M. Homsy. Nonlinear unstable viscous fingers in Hele-Shaw flows. I. Experiments. *Phys. Fluids*, 31:242, 1988.

[152] K. S. Korolev, M. Avlund, O. Hallatschek, and D. R. Nelson. Genetic demixing and evolution in linear stepping stone models. *Rev. Mod. Phys.*, 82(2):1691–1718, 2010.

[153] E. J. Koval. A method for predicting the performance of unstable miscible displacements in heterogeneous media. *Soc. Pet. Eng. J.*, pages 145–150, June 1963.

[154] H. Kurtuldu, J. S. Guasto, K. A. Johnson, and J. P. Gollub. Enhancement of biomixing by swimming algal cells in two-dimensional films. *Proc. Natl. Acad. Sci. U.S.A.*, 108:10391–10395, 2011.

[155] K. S. Lackner. A guide to CO_2 sequestration. *Science*, 300(5626):1677–1678, 2003.

[156] LaGriT. *LaGriT Manual.* Los Alamos National Laboratories, 2013.

[157] E. Lajeunesse, J. Martin, N. Rakotomalala, and D. Salin. 3D instability of miscible displacements in a Hele-Shaw cell. *Phys. Rev. Lett.*, 79:5254–5257, 1997.

[158] E. Lajeunesse, J. Martin, N. Rakotomalala, D. Salin, and Y. C. Yortsos. Miscible displacement in a Hele-Shaw cell at high rates. *J. Fluid Mech.*, 398:299, 1999.

[159] T. Le Borgne, M. Dentz, D. Bolster, J. Carrera, J.-R. de Dreuzy, and P. Davy. Non-Fickian mixing: Temporal evolution of the scalar dissipation rate in heterogeneous porous media. *Adv. Water Resour.*, 33(12):1468–1475, 2010.

[160] X. Y. Lei, G. Swoboda, and G. Zenz. Application of contact-friction interface element to tunnel excavation in faulted rock. *Comput. Geotech.*, 17:349–370, 1995.

[161] K. C. Leptos, J. S. Guasto, J. P. Gollub, A. I. Pesci, and R. E. Goldstein. Dynamics of enhanced tracer diffusion in suspensions of swimming eukaryotic microorganisms. *Phys. Rev. Lett.*, 103:198103, 2009.

[162] R. J. LeVeque. *Finite Volume Methods for Hyperbolic Problems.* Cambridge University Press, UK, 2002.

[163] R. W. Lewis, A. Makurat, and W. K. S. Pao. Fully coupled modeling of seabed subsidence and reservoir compaction of North Sea oil fields. *Hydrogeol. J.*, 11(1):142–161, 2003.

[164] R. W. Lewis and B. A. Schrefler. *The Finite Element Method in the Static and Dynamic deformation and Consolidation of Porous Media.* Wiley, Chichester, England, second edition, 1998.

[165] R. W. Lewis and Y. Sukirman. Finite element modelling of three-phase flow in deforming saturated oil reservoirs. *Int. J. Numer. Anal. Methods Geomech.*, 17:577–598, 1993.

[166] X. Li, Z. Liu, and R. W. Lewis. Mixed finite element method for coupled thermo-hydro-mechanical process in poro-elastic-plastic media at large strains. *Int. J. Numer. Meth. Eng.*, 64(5):667–708, 2005.

[167] B. E. Lofgren. Monitoring crustal deformation in The Geyser Clear Lake region. In *Research in The Geysers-Clear Lake geothermal area, northern California*, page 1141. U. S. Geological Survey, 1981.

[168] R. B. Lohman and M. Simons. Some thoughts on the use of InSAR data to constrain models of surface deformation: Noise structure and data downsampling. *Geochem. Geophys. Geosystems (G3)*, 6:1, 2005.

[169] C. Lomnitz. Earthquakes and reservoir impounding: State of the art. *Eng. Geol.*, 8:191–198, 1974.

[170] J.-A. Lopez-Comino, F. de Lis Mancilla, J. Morales, and D. Stich. Rupture directivity of the 2011, Mw 5.2 Lorca earthquake (Spain). *Geophys. Res. Lett.*, 539:L03301, 2012.

[171] M. W. Losey, M. A. Schmidt, and K. F. Jensen. Microfabricated multiphase packed-bed reactors: Characterization of mass transfer and reactions. *Ind. Eng. Chem. Res.*, 40:2555, 2001.

[172] A. E. H. Love. The stress produced in a semi-infinite solid by pressure on part of the boundary. *Phil. Trans. R. Soc. Lond. A*, 667:377–420, 1929.

[173] J. L. Lumley. Computational modeling of turbulent flows. *Adv. Appl. Mech.*, 18:123.

[174] J. M. MacInnes, Z. Chen, and R. W. K. Allen. Investigation of alternating-flow mixing in microchannels. *Chem. Eng. Sci.*, 60:3453, 2005.

[175] M. Mainguy and P. Longuemare. Coupling fluid flow and rock mechanics: formulations of the partial coupling between reservoir and geomechanics simulators. *Oil Gas Sci. Tech.*, 57:355–367, 2002.

[176] E. L. Majer, R. Baria, M. Stark, S. Oates, J. Bommer, B. Smith, and H. Asanuma. Induced seismicity associated with Enhanced Geothermal Systems. *Geothermics*, 36:185–222, 2007.

[177] J. Mandel. Consolidation of soils (mathematical study). *Geotechnique*, 3:287–299, 1953.

[178] O. Manickam and G. M. Homsy. Fingering instabilities in vertical miscible displacement flows in porous media. *J. Fluid Mech.*, 288:75, 1995.

[179] C. Marone. Laboratory-derived friction laws and their application to seismic faulting. *Ann. Rev. Earth Planet. Sci.*, 26:643–696, 1998.

[180] J. J. Martinez-Diaz, E. Masana, and M. Ortuno. Active tectonics of the Alhama de Murcia fault, Betic Cordillera, Spain. *J. Iberian Geol.*, 38:253–270, 2012.

[181] P.J. van Leeuwen and G. Evensen. Data assimilation and inverse methods in terms of a probabilistic formulation. *Mon. Weather Rev.*, 124:2898–2913, 1996.

[182] S. E. Minkoff, C. M. Stone, S. Bryant, M. Peszynska, and M. F. Wheeler. Coupled fluid flow and geomechanical deformation modeling. *J. Pet. Sci. Eng.*, 38:37–56, 2003.

[183] M. Mishra, M. Martin, and A. De Wit. Miscible viscous fingering with linear adsorption on the porous matrix. *Phys. Fluids*, 19:073101, 2007.

[184] M. Mishra, M. Martin, and A. De Wit. Differences in miscible viscous fingering of finite width slices with positive or negative log-mobility ratio. *Phys. Rev. E*, 78:066306, 2008.

[185] J. P. Morris, R. L. Detwiler, S. J. Friedman, O. Y. Vorobiev, and Y. Hao. The large-scale geomechanical and hydrogeological effects of multiple CO_2 injection sites on formation stability. *Int. J. Greenh. Gas Control*, 5(1):69–74, 2011.

[186] J. P. Morris, Y. Hao, W. Foxall, and W. McNab. A study of injection-induced mechanical deformation at the In Salah CO_2 storage project. *Int. J. Greenh. Gas Control*, 5(2):270–280, 2011.

[187] A. Mossop and P. Segall. Subsidence at The Geysers geothermal field, N. California from a comparison of GPS and leveling surveys. *Geophys. Res. Lett.*, 24:1839–1842, 1997.

[188] M. Muskat. *Physical Principles of Oil Production.* McGraw-Hill, New York, 1949.

[189] Y. Nagatsu, K. Matsuda, Y. Kato, and Y. Tada. Experimental study on miscible viscous fingering involving viscosity changes induced by variations in chemical species concentrations due to chemical reactions. *J. Fluid Mech.*, 571:475–493, 2007.

[190] N. Nakamura. Two-dimensional mixing, edge formation, and permeability diagnosed in an area coordinate. *J. Atmos. Sci.*, 53:1524, 1996.

[191] J.-P. Nicot and B. R. Scanlon. Water use for shale-gas production in Texas, U.S. *Environ. Sci. Tech.*, 46:3580–3586, 2012.

[192] E. Nikooee, G. Habibagahi, S. M. Hassanizadeh, and A. Ghahramani. Effective stress in unsaturated soils: A thermodynamic approach based on the interfacial energy and hydromechanical coupling. *Eur. J. Mech.-A/Solids*, 96:369–396, 2013.

[193] M. Nuth and L. Laloui. Effective stress concept in unsaturated soils: Clarification and validation of a unified framework. *Int. J. Numer. Anal. Methods Geomech.*, 32:771–801, 2008.

[194] Y. Okada. Surface deformation due to shear and tensile faults in a half-space. *Bull. Seismol. Soc. Am.*, 75:1135–1154, 1985.

[195] P. Olson, P. G. Silver, and R. W. Carlson. The large scale structure of convection in the earth's mantle. *Nature*, 344:209, 1990.

[196] F. M. Orr. Onshore geologic storage of CO_2. *Science*, 325:1656–1658, 2009.

[197] S. G. Osborn, A. Vengosh, N. R. Warner, and R. B. Jackson. Methane contamination of drinking water accompanying gas-well drilling and hydraulic fracturing. *Proc. Natl. Acad. Sci. U.S.A.*, 108(20):8172–8176, 2011.

[198] J. M. Ottino and S. Wiggins. Introduction: mixing in microfluidics. *Phil. Trans. R. Soc. Lond.* A, 362:923–935, 2004.

[199] S. Pacala and R. Socolow. Stability wedges: Solving the climate problem for the next 50 years with current technologies. *Science*, 305:968–972, 2004.

[200] H. Pan and H. Cao. *User Manual for General Purpose Research Simulator.* Stanford University Petroleum Engineering Institute, Stanford, CA, 2010.

[201] W. K. S. Pao and R. W. Lewis. Three dimensional finite element simulation of three-phase flow in a deforming fissured reservoir. *Comput. Meth. Appl. Mech. Eng.*, 191:2631–2659, 2002.

[202] K. C. Park. Stabilization of partitioned solution procedure for pore fluid–soil interaction analysis. *Int. J. Numer. Meth. Eng.*, 19:1669–1673, 1983.

[203] L. Paterson. Fingering with miscible fluids in a Hele-Shaw cell. *Phys. Fluids*, 28:26, 1985.

[204] J. C. Pechmann, W. J. Arabasz, K. L. Pankow, R. Burlacu, and M. K. McCarter. Seismological report on the 6 Aug 2007 Crandall Canyon Mine collapse in Utah. *Seismol. Res. Lett.*, 79:10–12, 2008.

[205] J. C. Pechmann, W. R. Walter, S. J. Nava, and W. J. Arabasz. The February 3, 1995, ML 5.1 seismic event in the Trona mining district of southwestern Wyoming. *Seismol. Res. Lett.*, 66:25–34, 1995.

[206] P. Petitjeans, C.-Y. Chen, E. Meiburg, and T. Maxworthy. Miscible quarter five-spot displacements in a Hele-Shaw cell and the role of flow-induced dispersion. *Phys. Fluids*, 11:1705–1716, 1999.

[207] P. J. Phillips and M. F. Wheeler. A coupling of mixed and continuous Galerkin finite element methods for poroelasticity I: the continuous in time case. *Comput. Geosci.*, 11:131–144, 2007.

[208] P. J. Phillips and M. F. Wheeler. A coupling of mixed and continuous Galerkin finite element methods for poroelasticity II: the discrete-in-time case. *Comput. Geosci.*, 11:145–158, 2007.

[209] S. B. Pope. *Turbulent Flows.* Cambridge University Press, 2000.

[210] J. D. Posner, C. L. Perez, and J. G. Santiago. Electric fields yield chaos in microflows. *Proc. Natl. Acad. Sci. U.S.A.*, 109:14353–14356, 2012.

[211] D. Pritchard. The instability of thermal and fluid fronts during radial injection in a porous medium. *J. Fluid Mech.*, 508:133, 2004.

[212] C. B. Raleigh, J. H. Healy, and J. D. Bredehoeft. An experiment in earthquake control at Rangely, Colorado. *Science*, 191:1230–1237, 1976.

[213] A. Riaz and E. Meiburg. Three-dimensional miscible displacement simulations in homogeneous porous media with gravity override. *J. Fluid Mech.*, 494:95, 2003.

[214] A. Riaz, C. Pankiewitz, and E. Meiburg. Linear stability of radial displacements in porous media: Influence of velocity-induced dispersion and concentration-dependent diffusion. *Phys. Fluids*, 16:3592, 2004.

[215] J. R. Rice. Spatio-temporal complexity of slip on a fault. *J. Geophys. Res.*, 98:9885–9907, 1993.

[216] E. Roeloffs. Fault stability changes induced beneath a reservoir with cyclic variations in water level. *J. Geophys. Res.*, 93:2107–2124, 1988.

[217] E. Roeloffs. Poroelastic techniques in the study of earthquake-related hydrologic phenomena. *Adv. Geophys.*, 37:135–195, 1996.

[218] A. L. Ruina. Slip instability and state variable friction laws. *Geophys. Res. Lett.*, 88:359–370, 1983.

[219] M. Ruith and E. Meiburg. Miscible rectilinear displacements with gravity override. Part 1. Homogeneous porous medium. *J. Fluid Mech.*, 420:225–257, 2000.

[220] J. Rutqvist, J. T. Birkholzer, F. Cappa, and C. F. Tsang. Estimating maximum sustainable injection pressure during geological sequestration of CO_2 using coupled fluid flow and geomechanical fault-slip analysis. *Energy Conv. Manag.*, 48:1798–1807, 2007.

[221] J. Rutqvist, J. T. Birkholzer, and C. F. Tsang. Coupled reservoir–geomechanical analysis of the potential for tensile and shear failure associated with CO_2 injection in multilayered reservoir–caprock systems. *Int. J. Rock Mech. Min. Sci.*, 45:132–143, 2008.

[222] J. Rutqvist, A. P. Rinaldi, F. Cappa, and G. J. Moridis. Modeling of fault reactivation and induced seismicity during hydraulic fracturing of shale-gas reservoirs. *J. Petrol. Sci. Eng.*, 107:31–44, 2013.

[223] J. Rutqvist, D. W. Vasco, and L. Myer. Coupled reservoir-geomechanical analysis of CO_2 injection and ground deformations at In Salah, Algeria. *Int. J. Greenh. Gas Control*, 4:225–230, 2010.

[224] J. Rutqvist, Y. S. Wu, C. F. Tsang, and G. Bodvarsson. A modeling approach for analysis of coupled multiphase fluid flow, heat transfer, and deformation in fractured porous rock. *Int. J. Rock Mech. Min. Sci.*, 39:429–442, 2002.

[225] D. Saintillan and M. J. Shelley. Instabilities and pattern formation in active particle suspensions: Kinetic theory and continuum simulations. *Phys. Rev. Lett.*, 100:178103, 2008.

[226] SAMG. *SAMG User's Manual.* Fraunhofer Institute for Algorithms and Scientific Computing (SCAI), Germany, 2010.

[227] P. Samier and S. Gennaro. A practical iterative scheme for coupling geomechanics with reservoir simulation. Paper SPE 107077. In *SPE Europec/EAGE*, London, 2007.

[228] R. L. Schiffman, A.T.-F. Chen, and J. C. Jordan. An analysis of consolidation theories. *J. Soil Mech.*, 95:285–312, 1969.

[229] Schlumberger. *Eclipse 100 Reference Manual 2009.1.* Houston, 2009.

[230] C. H. Scholz. Mechanics of faulting. *Ann. Rev. Earth Planet. Sci.*, 17:309–334, 1989.

[231] Nat. Acad. Sci. *Induced Seismicity Potential in Energy Technologies: A Report of the National Research Council.* The Nat. Acad. Press, Washington, DC, 2012.

[232] P. Segall. Earthquakes triggered by fluid extraction. *Geology*, 17:942–946, 1989.

[233] A. Settari and F. Mourits. A coupled reservoir and geomechanical simulation system. *Soc. Pet. Eng. J.*, 3:219–226, 1998.

[234] A. Settari and D. A. Walters. Advances in coupled geomechanical and reservoir modeling with applications to reservoir compaction. *Soc. Pet. Eng. J.*, 6:334–342, 2001.

[235] Simulia. *Abaqus Version 6.7 Reference Manual*, 2007.

[236] A. W. Skempton. The pore pressure coefficients A and B. *Geotechnique*, 4:143–147, 1954.

[237] D. Snyder and S. Tait. A flow-front instability in viscous gravity currents. *J. Fluid Mech.*, 369:1–21, 1998.

[238] A. Sokolov and I. S. Aranson. Reduction of viscosity in suspension of swimming bacteria. *Phys. Rev. Lett.*, 103:148101, 2009.

[239] A. Sokolov, R. E. Goldstein, F. I. Feldchtein, and I. S. Aranson. Enhanced mixing and spatial instability in concentrated bacterial suspensions. *Phys. Rev. E*, 80:031903, 2009.

[240] T. H. Solomon and J. P. Gollub. Chaotic particle transport in time-dependent Rayleigh-bénard convection. *Phys. Rev. A*, 38:6280, 1988.

[241] T. M. Squires and S. R. Quake. Microfluidics: Fluid physics at the nanoliter scale. *Rev. Mod. Phys.*, 77(3):977–1026, 2005.

[242] F. I. Stalkup. Carbon dioxide miscible flooding: Past, present, and outlook for the future. *J. Pet. Technol.*, 30:1102–1112, 1978.

[243] F. I. Stalkup. *Miscible Displacement.* SPE Monograph Series, Vol. 8, Dallas, 1983.

[244] H. A. Stone, A. D. Stroock, and A. Ajdari. Engineering flows in small devices: Microfluidics toward a lab-on-a-chip. *Ann. Rev. Fluid Mech.*, 36:381–411, 2004.

[245] A. D. Stroock, S. K. W. Dertinger, A. Ajdari, I. Mezic, H. A. Stone, and G. M. Whitesides. Chaotic mixer for microchannels. *Science*, 295:647–651, 2002.

[246] Y. Sukirman and R. W. Lewis. A finite element solution of a fully coupled implicit formulation for reservoir simulation. *Int. J. Numer. Anal. Methods Geomech.*, 17(10):677–698, 1993.

[247] M. L. Szulczewski, C. W. MacMinn, H. J. Herzog, and R. Juanes. The lifetime of carbon capture and storage as a climate-change mitigation technology. *Proc. Natl. Acad. Sci. U.S.A.*, 109(14):5185–5189, 2012.

[248] C.-T. Tan and G. M. Homsy. Stability of miscible displacements in porous media: Rectilinear flow. *Phys. Fluids*, 29:3549, 1986.

[249] C. T. Tan and G. M. Homsy. Simulation of nonlinear viscous fingering in miscible displacement. *Phys. Fluids*, 31:1330–1338, 1988.

[250] C.-T. Tan and G. M. Homsy. Viscous fingering with permeability heterogeneity. *Phys. Fluids*, 4:1099, 1992.

[251] H. A. Tchelepi and F. M. Orr. Interaction of viscous fingering, permeability heterogeneity and gravity segregation in three dimensions. *SPE Reserv. Eng.*, 9(4):266–271, November 1994.

[252] H. A. Tchelepi, F. M. Orr, N. Rakotomalala, D. Salin, and R. Woumeni. Dispersion, permeability heterogeneity, and viscous fingering – Acoustic experimental-observations and particle-tracking simulations. *Phys. Fluids A*, 5:1558–1574, 1993.

[253] P. Teatini, N. Castelletto, M. Ferronato, G. Gambolati, C. Janna, E. Cairo, D. Marzorati, D. Colombo, A. Ferretti, A. Bagliani, and F. Bottazzi. Geomechanical response to seasonal gas storage in depleted reservoirs: A case study in the Po River basin, Italy. *J. Geophys. Res.*, 116:F02002, 2011.

[254] H. Tennekes and J. L. Lumley. *A First Course in Turbulence.* The MIT Press, 1972.

[255] K. Terzaghi, R. B. Peck, and G. Mesri. *Soil Mechanics in Engineering Practice.* John Wiley & Sons, New York, NY, 1996.

[256] L. K. Thomas, L. Y. Chin, R. G. Pierson, and J. E. Sylte. Coupled geomechanics and reservoir simulation. *Soc. Pet. Eng. J.*, 8(4):350–358, 2003.

[257] M. R. Todd and W. J. Longstaff. The development, testing and application of a numerical simulator for predicting miscible flood performance. *J. Pet. Technol.*, pages 874–882, July 1972.

[258] D. Tran, L. Nghiem, and L. Buchanan. Improved iterative coupling of geomechanics with reservoir simulation. Paper SPE 93244. In *SPE Reservoir Simulation Symposium*, Houston, TX, January 2005.

[259] D. Tran, A. Settari, and L. Nghiem. New iterative coupling between a reservoir simulator and a geomechanics module. *Soc. Pet. Eng. J.*, 9(3):362–369, 2004.

[260] Reuters UK. Small earthquake hits Spain near gas storage project. `http://uk.reuters.com/article/2013/10/01/spain-gas-idUKL6N0HR29820131001`. Accessed: 2013-12-30.

[261] N. J. van der Elst, H. M. Savage, K. M. Keranen, and G. A. Abers. Enhanced remote earthquake triggering at fluid-injection sites in the midwestern United States. *Science*, 341:164–167, 2013.

[262] M. T. van Genuchten. A closed-form equation for predicting the hydraulic conductivity of unsaturated soils. *Soil Sci. Soc. Am.*, 44:892–898, 1980.

[263] P. E. van Keken, E. H. Hauri, and C. J. Ballentine. Mantle mixing: The generation, preservation, and destruction of chemical heterogeneity. *Annu. Rev. Earth Planet. Sci.*, 30:493, 2002.

[264] I. Vlahinic, H. M. Jennings, J. E. Andrade, and J. J. Thomas. A novel and general form of effective stress in a partially saturated porous material: The influence of microstructure. *Mech. Mater.*, 43:25–35, 2011.

[265] J. Wan, L. J. Durlofsky, T .J. R. Hughes, and K. Aziz. Stabilized finite element methods for coupled geomechanics–reservoir flow simulations. Paper SPE 79694. In *SPE Res. Simul. Sym.*, Houston, Feb. 2003.

[266] C. Y. Wang, L. H. Cheng, C. V. Chin, and S. B. Yu. Coseismic hydrologic response of an alluvial fan to the 1999 Chi-Chi earthquake, Taiwan. *Geology*, 29:831–834, 2001.

[267] H. F. Wang. *Theory of Linear Poroelasticity with Applications to Geomechanics and Hydrogeology.* Princeton University Press, 2000.

[268] Z. Warhaft. Passive scalars in turbulent flows. *Ann. Rev. Fluid Mech.*, 32:203–240, 2000.

[269] N. R. Warner, R. B. Jackson, T. H. Darrah, S. G. Osborn, A. Down, K. Zhao, A. White, and A. Vengosh. Geochemical evidence for possible natural migration of Marcellus Formation brine to shallow aquifers in Pennsylvania. *Proc. Natl. Acad. Sci. U.S.A.*, 109(30):11961–11966, 2012.

[270] N. R. Warner, R. B. Jackson, T. H. Darrah, S. G. Osborn, A. Down, K. Zhao, A. White, and A. Vengosh. Reply to Engelder: Potential for fluid migration from the Marcellus Formation remains possible. *Proc. Natl. Acad. Sci. U.S.A.*, 109(52):E3626, 2012.

[271] C. A. Williams. Development of a package for modeling stress in the lithosphere. *Eos Trans. AGU*, 87:T24A–01, 2006.

[272] Z. Yang and Y. C. Yortsos. Asymptotic solutions of miscible displacements in geometries of large aspect ratio. *Phys. Fluids*, 9(2):286–298, 1997.

[273] Z. M. Yang, Y. C. Yortsos, and D. Salin. Asymptotic regimes in unstable miscible displacements in random porous media. *Adv. Water Resour.*, 25:885–898, 2002.

[274] R. F. Yerkes and R. O. Castle. Seismicity and faulting attributable to fluid extraction. *Eng. Geol.*, 10:151–167, 1976.

[275] Y. C. Yortsos and M. Zeybek. Dispersion driven instability in miscible displacement in porous media. *Phys. Fluids*, 31:3511, 1988.

[276] H. R. Zhang, K. S. Sorbie, and N. B. Tsibuklis. Viscous fingering in five-spot experimental porous media: new experimental results and numerical simulation. *Chem. Eng. Sci.*, 52(1):37–54, 1997.

[277] O. C. Zienkiewicz, D. K. Paul, and A. H. C. Chan. Unconditionally stable staggered solution procedure for soil–pore fluid interaction problems. *Int. J. Numer. Meth. Eng.*, 26(5):1039–1055, 1988.

[278] O. C. Zienkiewicz and R. L. Taylor. *The Finite Element Method for Solid and Structural Mechanics.* Elsevier, Burlington, MA, 2005.

[279] W. B. Zimmerman and G. M. Homsy. Nonlinear viscous fingering in miscible displacement with anisotropic dispersion. *Phys. Fluids A*, 3:1859–1872, 1991.

[280] W. B. Zimmerman and G. M. Homsy. Three-dimensional viscous fingering: A numerical study. *Phys. Fluids A*, 4:1901–1914, 1992.

[281] W. B. Zimmerman and G. M. Homsy. Viscous fingering in miscible displacements: Unification of effects of viscosity contrast, anisotropic dispersion, and velocity dependence of dispersion on nonlinear finger propagation. *Phys. Fluids*, 4:2348, 1992.

[282] M. D. Zoback. *Reservoir Geomechanics.* Cambridge University Press, UK, 2007.

[283] M. D. Zoback and S. M. Gorelick. Earthquake triggering and large-scale geologic storage of carbon dioxide. *Proc. Natl. Acad. Sci. U.S.A.*, 109:10164–10168, 2012.

[284] M. D. Zoback and S. M. Gorelick. Reply to Juanes et al.: Evidence that earthquake triggering could render long-term carbon storage unsuccessful in many regions. *Proc. Natl. Acad. Sci. U.S.A.*, 109(52):E3624, 2012.